Multi-Scale Design of Ink Formulations for the 3D Bioprinting of Soft and Elastic Tissue-Mimetic Structures

by

Yun Wu

A thesis

presented to the University Of Waterloo

in fulfilment of the

thesis requirement for the degree of

Doctor of Philosophy

in

Chemistry (Nanotechnology)

Waterloo, Ontario, Canada, 2021

Examining Committee Membership

The following served on the Examining Committee for this thesis. The decision of the Examining Committee is by majority vote.

External Examiner	Eugenia Kumacheva Professor
Supervisor	Shirley Tang Professor
Internal Member	John Honek Professor
Internal Member	Juewen Liu Professor
Internal-external Member	Michael Tam Professor

AUTHOR'S DECLARATION

I hereby declare that I am the sole author of this thesis. This is a true copy of the thesis, including any required final revisions, as accepted by my examiners.

I understand that my thesis may be made electronically available to the public.

Abstract

Three-dimensional (3D) engineered tissue and organ models with adjustable biochemical and physical properties are needed in regenerative medicine. As such, 3D printing has emerged as a potential strategy to create more complex tissue-like constructs compared to conventional microfabrication techniques. It allows for precise positioning of biomaterials to create tissue constructs that imitate natural tissues and organs. Among 3D printing strategies, including extrusion-based, light-induced, and inkjet-based methods, the extrusion-based technique is broadly employed owing to its ease of use and compatibility with multi-material printing. However, the fabrication of accurate and precise human-mimetic functional 3D constructs still remains challenging. This thesis presents an investigation on the bioink material preparation from nano-, micro- to macro-scale to provide high structural resolution and cell viability and functionality.

Chapter 3 presents a strong shear-thinning, solid-like bioink employing alginate (1%), cellulose nanocrystals (CNCs) (3%), and gelatin methacryloyl (GelMA) (5%) (namely 135ACG hybrid ink) for the direct printing of cell-laden and acellular architectures. After crosslinking, the ACG gel can also provide a stiff extracellular matrix (ECM) ideal for stromal cell growth. By controlling the polymer concentration, a GelMA (4%) bioink was designed to encapsulate hepatoma cells (hepG2), as GelMA gel possesses the desired low mechanical stiffness matched human liver tissue. Four different versions of to-scale liver lobule-mimetic constructs were fabricated via ME bioprinting, with precise positioning of two different cell types (NIH/3T3 and hepG2) embedded in matching ECMs (135ACG and GelMA, respectively). The four versions allowed us to exam effects of mechanical cues and intercellular interactions on cell behaviors. Fibroblasts thrived in stiff 135ACG matrix and aligned at

the 135ACG/GelMA boundary due to durotaxis, while hepG2 formed spheroids exclusively in the soft GelMA matrix. Elevated albumin production was observed in the bicellular 3D co-culture of hepG2 and NIH/3T3, both with and without direct intercellular contact, indicating that improved hepatic cell function can be attributed to soluble chemical factors. Overall, our results showed that complex constructs with multiple cell types and varying ECMs can be bioprinted and potentially be useful for both fundamental biomedical research and translational tissue engineering.

Chapter 4 presents a supporting bath-based embedded 3D printing strategy to fabricate large-scale architectures. Novel inks composed of 10 wt% glycidyl methacrylated poly(vinyl alcohol) (PVAGMA) with a different degree of substitution (DOS) and 4 wt% CNCs (PVAGMA(DOS)/CNC) with strong shear-thinning properties were developed. By controlling the DOS of PVAGMA and the crosslinking method, inks with the desired mechanical stiffness and toughness mimicking that of healthy arteries and arteries with atherosclerosis were designed to construct vascular phantoms. Cyclic tensile tests and an *in-vitro* hemodynamic study were performed on the hydrogels, illustrating that our ink compositions, namely PVAGMA2/CNC and PVAGMA4/CNC, possessed strong mechanical stability, durability, and recovery property. The burst circumferential tensile stress obtained from an *in-vitro* hemodynamic study and rupture tensile stress acquired under uniaxial test of PVAGMA2/CNC and PVAGMA4/CNC were comparable suggesting the optimal layer integrity and the mechanical strength was not influenced by the printing direction. Additionally, the burst pressure of our hydrogels was found to be about 90 mm Hg and the printed vascular phantoms were able to withstand a carotid pulse-mimetic pulsatile flow (60 beats/min with a peak flow rate of 27 mL/s) for over 10 days. Furthermore, with acoustic properties of PVAGMA/CNC hydrogels similar to those of human arteries,

we demonstrated their capability in ultrasonics by embedded printing three different versions of straight vascular phantoms. B-mode imaging were performed on the phantoms to confirm the vessel dimensions and analyze vessel strain of the softer PVAGMA2/CNC and stiffer PVAGMA4/CNC. It was found that the vessel strain was 24.6% and 8.9% for PVAGMA2/CNC and PVAGMA4/CNC, respectively, demonstrating that the two bioink materials can be used for vessel-mimetic materials. It is anticipated that this artery phantom can serve as a platform to evaluate local arterial stiffness estimation algorithms. Overall, our results elucidated the great potential of the PVAGMA-based inks and granular supporting material to create biofunctional heterogeneous vasculature via embedded printing strategy for regenerative medicine and tissue engineering applications.

Taken all together, this thesis presents a comprehensive study on developing and characterizing various bioink materials and bioprinting cellular and acellular constructs via free-form or embedded printing strategy. Our developed bioink materials and ME-based printing methods offered new approaches to address the central challenges in tissue engineering to create heterogeneous constructs with varying ECMs to recapitulate biological functions.

Acknowledgments

I would like to express my sincere gratitude to my supervisor, Dr. Shirley Tang, for her inspiring research advices and tremendous support during my Ph.D. studies. I have learned how to think and solve problem from her and it encouraged me to become a better researcher. It was a wonderful time to do research in this group.

I would also like to thank my committee members, Dr. John Honek, Dr. Juewen Liu and Dr. Michael Tam, for their guidance and valuable comments on my research from seminar, comprehensive exam, annual meeting all the way to my Ph.D. thesis defense during the past few years. I would like extend my gratitude to my external examiner Dr. Eugenia Kumacheva for reading my thesis and attending the thesis defense.

I would like to thank Dr. Boxin Zhao and Dr. Alfred Yu for providing access to the compression tester and ultrasound imaging, respectively. I would like to thank Pengxiang Si from Dr. Zhao's group for the training of the compression tester. I thank Adrian Chee for his help on the sample preparation and ultrasound imaging. I would also like to thank Chris Kleven for helping me set up instruments in the lab.

I would like to thank the previous and present group fellows: Irfani Ausri, Hossein Golzar, Kyle Chu, Andrew Wenger, Yuxing Wang, Zhi Li, and Kai Wang who offered kind help and scientific discussions. They provided me with technical guidance and knowledge in the lab. In particular, I would like to thank Irfani for helping review articles and this thesis.

Last, my deepest gratitude goes to my family. I am grateful to my parents and grandparents. Thank you for bringing me up and unquestioningly supporting me through my studies. Without your

love and encouragement, I would never be where I am now.

Table of Contents

List of Figures

List of Tables

List of Abbreviations

2D	two-dimensional
3D	three-dimensional
ACG	alginate-cellulose nanocrystal-gelatin methacryloyl
ALD	acute liver disease
CAD	computer-assisted design
CB	carbonate-bicarbonate
CBN	carbon-based nanomaterial
CCA	common carotid artery
CD	carbon dot
CLD	chronic liver disease
CNC	cellulose nanocrystal
CNF	cellulose nanofibrils
CNT	carbon nanotube
CT	computed tomography
CVD	cardiovascular disease
DAPI	4’,6-diamidino-2-phenylindole
dECM	decellularized ECM
DLP	digital light processing
DMAP	4-(N,N-dimethylamino)pyridine
DMEM	Dulbecco's Modified Eagle's Medium

DMSO	dimethyl sulfoxide
D_2O	deuterium oxide
DOS	degree of substitution
EC	endothelial cell
ECA	external carotid artery
ECM	extracellular matrix
EDC	1-ethyl-3-(3-dimethylaminopropyl)carbodiimide
EDTA	ethylenediaminetetraacetic acid
EMEM	Eagle's Minimum Essential Medium
EthD-1	ethidium homodimer-1
F127-BUM	F127-bisurethane methacrylate
FBS	fetal bovine serum
FDM	fused deposition modeling
GelMA	gelatin methacryloyl
GMA	glycidyl metharylate
HA	hyaluronic acid
hASC	human Adipose Stem Cells
hMSC	human Mesenchymal Stem Cell
HUVEC	human umbilical vein endothelial cell
ICA	internal carotid artery
ID	inner diameter

IMT	intima-media thickness
Irgacure 2959	1-[4-(2-hydroxyethoxy)-phenyl]-2-hydroxy-2-methyl-1-propanone
LAB	laser-assisted bioprinting
LAP	lithium phenyl-2, 4, 6-trimethylbenzoylphosphinate
ME	micro-extrusion
MRI	magnetic resonance imaging
MRT	magnetic resonance tomography
MWCO	molecular-weight-cutoff
NHS	N-hydroxysuccinimide
NMR	nuclear magnetic resonance
OD	outer diameter
PAA	polyallylamine
PBS	phosphate buffered saline
PDMS	polydimethylsiloxane
PEG	poly(ethylene glycol)
PEGDA	poly(ethylene glycol) diacrylate
PEGTA	poly(ethylene glycol)-tetra-acrylate
PEO	poly(ethylene oxide)
PPO	poly(propylene)
PT	portal tract
PVA	poly(vinyl alcohol)

PVAGMA	Glycidyl methacrylated PVA
RGD	Arg-Gly-Asp
SLA	stereolithography
STL	standard tessellation language
SMC	smooth muscle cell
TE	tissue engineering
TEMPO	2,2,6,6-tetramethylpiperidine-1-oxyl
VEGF	vascular endothelial growth factor
VS	vascular septum

Chapter 1 Introduction

1.1 3D Bioprinting

Three-dimensional (3D) printing is an additive manufacturing process that fabricates 3D architectures layer by layer with various materials, such as plastics, metal, ceramics, and polymers.[1–3] A computer-assisted design (CAD) software is seamlessly integrated with 3D printers and generates standard tessellation language (STL) files which can be converted to G-codes that are readable by the 3D printers.[4,5] There are several advantages of 3D printing over traditional manufacturing process, such as cost-efficient, easy operation, available mass production, and resource-sharing.[6] Therefore, the applications of 3D printing are not only in the industry, like construction, apparel, and toys, but also in medical applications, such as human cartilage, ears, and skin. To date, the closet 3D printing has gotten to a medical application is the fabrication of non-living constructs, which function as structural or space-filling prostheses.[7] Cells are then seeded on top or in the meshes of the printed constructs. However, the ultimate purpose of tissue engineering is to replace the damaged organs.[8,9] Bioprinting, a subset of 3D printing, can be employed to fabricate human organ-mimetic scaffolds. It precisely deposit biomaterials and cells to create heterogeneous tissue-mimetic constructs that promotes cell-cell and cell-extracellular matrix interactions in a 3D environment, features which are absent in two-dimensional (2D) cell culture systems.[10–12] The most-commonly used 3D printing techniques for medical applications are classified to four categories: inkjet-based, laser-assisted, light-induced, and extrusion-based methods (**Figure 1.1**).[13–22]

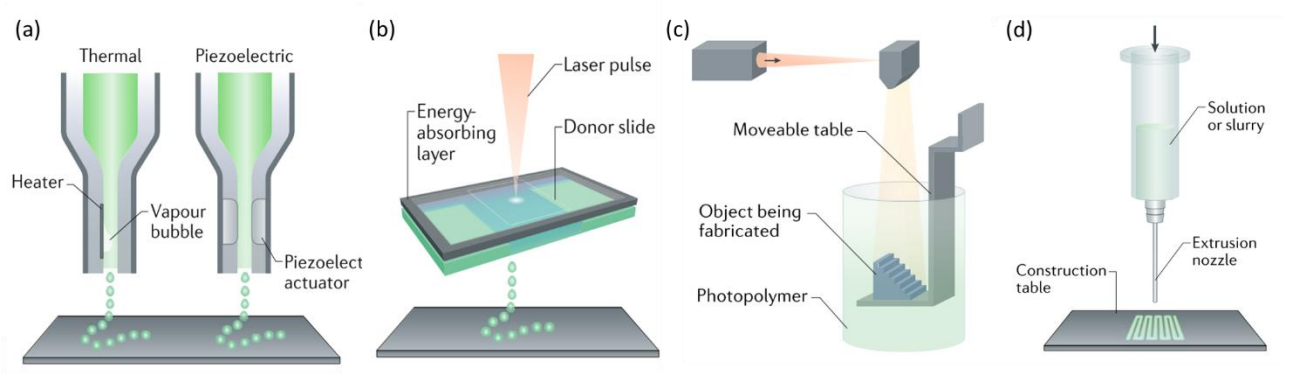

Figure 0.1 Schematics of four different 3D printing techniques: (a) inkjet-based, (b) laser-assisted, (c) light-induced, and (d) extrusion-based methods. Reproduced from Ref. 22.

Inkjet printing is the least technologically complex and expensive method, and it produces small volumes (1-100 picoliters) of droplets from a needle to a printing platform. The droplets are generated through electrically heating the needle to produce a vapor bubble or breaking the liquid into droplets by piezoelectric actuator.[3,17] Three important phases in inkjet printing process, including drop formation, drop/substrate interaction, and drop solidification, jointly control the final structure dimensions and the spatial resolution.[17] It has been found that the spatial resolution can reach up to 85-300 μm, which is determined by the surface interactions between adjacent droplets, and between droplets and the substrate.[17] Additionally, the non-contact fabrication strategy of inkjet printing helps avoid deformation of the previous deposited patterns. However, the major deficiency of inkjet-based printing is the selection of materials and low cell viability. The viscosity of the ink should be very low usually between 3.5 and 12 mPa·s, thus limiting its application in 2D tissue engineering (e.g., skin and cartilage constructs).[9]

Laser-assisted bioprinting (LAB) has been widely utilized to deposit biological materials including cells, nucleic acids, and peptides.[23] LAB works by applying an energized pulsed laser on target or

ribbons that are composed of bioinks with a laser-absorbing metal layer, such as gold or titanium. The bioinks comprised of cells and biomaterials are deposited over the metal layer followed by being vaporized, and bioinks are ejected to the receiving substrate.[23] It can work with materials with a wide range of viscosities ranging from 1 to 300 mPa s and the cell concentration can be up to 10^8 cells/mL.[23] The main advantage of this strategy is the high spatial resolution (> 5 μm) and a needle-free system, avoiding the needle clogging issue. An important consideration with LAB is that the materials should exhibit rapid crosslinking to prevent cells from gravitationally-settling over the long printing process.[23]

Light induced 3D printing, also known as stereolithography (SLA), was developed in the 1980s.[3,17,18] It worked by using scanning mirrors to move a focal point of light and crosslinking the liquid photo-responsive materials on the build stage. After being cured, the build stage lowers into the solution to allow for subsequent crosslinking. The lowering height of the stage is smaller than the curing depth, allowing for strong layer integrity.[24] Recent developments in the light source and refined mirror-lens system have improved the resolution and speed of SLA crosslinking. The highest resolutions of traditional SLA is approximately 25 μm, whereas the micro SLA and high definition SLA are in the single micrometer range.[16] Additionally, similar to LAB, the needle-free system prevents the needle clogging issues. However, one biggest limitations of light-induced 3D printing technology is that only photocurable bioink can be used and the long UV-exposure time will affect cell viability.[24]

Microextrusion-based (ME) printing methods, based on the technique where materials are extruded through a needle and a three-axis motion control system is used to control the movement of needles to build 3D objects layer-by-layer, are widely used to fabricate devices. In the traditional extrusion-based printing technique, fused deposition modeling (FDM), plastics are melted, extruded

under an applied pressure, solidified, and quickly bound to the previous layers to retain its shape.[8] Based on the idea of the FDM printer, the ME bioprinter with a syringe system has been produced. Biomaterials with various viscosities ranging from 30 mPa·s to over 60 kPa·s can be added to the syringe and extruded to generate 3D architectures.[9]

In summary, each deposition method has its own advantages and disadvantages. Inkjet-based printing is the least technologically complex and expensive method, and can generate high-resolution structures, but is limited to 2D tissue constructs due to the low viscosity of the bioinks. In addition, the high shear forces may cause cell damage when cells are incorporated into the biomterials. Although light-induced 3D printing is able to utilize bioinks with any viscosity and high density of cells to fabricate a construct with a high resolution, lower than 25 µm, it is hard to fabricate tissue constructs with multiple cell types via this strategy.[9] On the other hand, extrusion-based bioprinting can be utilized to print multiple cell lines within defined regions in the cm range and is suitable for scale-up production without geometrical limits. The downside is that compared to the other methods, it has the lowest printing resolution at 100 µm. Moreover, cell viability is still a potential issue with the ME bioprinters as cells experience too high of a shear stress when being extruded through the needles, thus damaging cell membranes.

In this project, ME 3D bioprinting is chosen as the bioprinting strategy due to the ease of use, ability to use a wide range of bioink viscosities, high cell loading density, multiple polymerization methods, and precise printing of defined constructs.[25–28] It can be divided into two categories, pneumatic (**Figure 1.2a**)and mechanically driven (**Figure 1.2b**) systems, based on the force that drives the extrusion.[9] Pneumatic systems can be easily controlled by adjusting the compressed air controller

Table 0-1 Comparison of four types of bioprinting techniques

Specification	Inkjet	Laser-assisted	Light-induced	Microextrusion-based	Ref
Principle	Droplets are generated through electrically heating or by piezoelectric actuator.	Applying an energized pulsed laser on target or ribbons and being deposited over metal substrates.	UV-initiated curing of the liquid photo-responsive materials on the build stage.	Extrusion of pre-gel solution through a needle and build up layer-by-layer.	12-24
Resolution	85-300 μm	> 5 μm	> 25 μm	100 μm - mm	
Gelatin	Fast Chemical, photo-crosslinking	Fast Chemical, photo-crosslinking	Fast Chemical, photo-crosslinking	Medium Chemical, photo-crosslinking, shear-thinning, temperature	
Dispensing speed	Fast (1-10,000	Medium-fast (200-1600		Slow (10 μm-50 mm/s)	
Material viscosity	3.5-12 mPa s	1-300 mPa s	1-300 mPa s	30-6 x 10^7 mPa s	
Cell density	Low, < 10^6 cells/mL	Medium, 10^8 cells/mL	Medium, 10^8 cells/mL	High, cell spheroids	
Cell viability	>85%	>95%	>90%	40%-80%	
Advantages	Low cost; Simple system; High resolution; Fast bioprinting speed; High cell viability	High resolution; High cell viability; Good vertical fidelity;	Low cost; High resolution; Fast bioprinting speeds; High cell viability; Fair vertical fidelity	Bioinks with wide range of viscosity; High cell density; Simple system; Multiple composition feasibility	
Disadvantages	Bioink with limited viscosity (low-to-medium); Low cell density; Mostly applied to 2D	Complex system; Expensive; Medium bioprinting speed; Medium on cell density	Moderately complex system; Bioink limited to photo-polymerization crosslinking; Medium on cell density	Low to moderate cell viability; Slow bioprinting speed; Moderate resolution	

so that bioinks with various range of viscosities (30 mPa s to > 60 kPa s) can be used with this technique. Meanwhile, high viscosity bioinks (> 60 kPa s) are preferred in mechanical systems in which forces are directly applied to pistons.[9] A pneumatic system is selected in this project to better control the bioink extrusion and avoid cell damage during printing. In order to achieve the optimal resolution of the printed architectures, systematic printing parameters, such as applied pressure, needle printing speed, extrusion flow rate, needle diameter, and layer height, should be considered. For example, a needle with large gauge is required to print fine filaments but may reduce the cell viability due to the increased shear stress experienced by cells during extrusion.

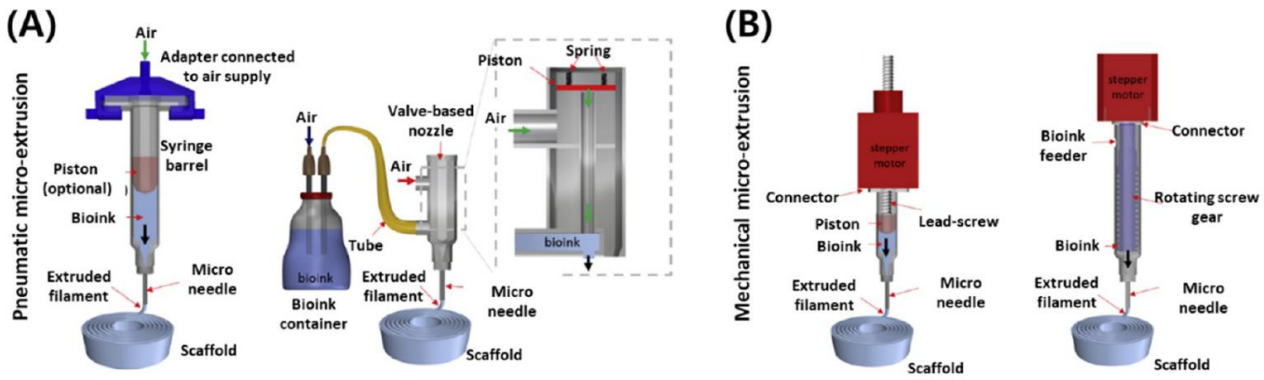

Figure 0.2 Schematics of (A) pneumatic and (B) mechanical driven microextrusion-based printing systems. Reproduced from Ref. 9.

1.1.1 Embedded Printing

Despite all of the advantages of ME printing, generating heterogeneous complex 3D tissue or organ-mimetic constructs with multiple biomaterials in high-resolution still remains challenging. As such, supporting bath-based embedded 3D bioprinting has arisen to increase the quality and fidelity of the printing. Materials used for the supporting bath include viscous oil,[29] elastomer,[30] self-healing hydrogels,[31] and granular gel suspension.[32–34]

Generally, the supporting material should act like a Bingham plastic, being rigid at low shear stresses but flowing at higher shear stresses.[26,31–33] First, a suitable yield stress is required. If the yield stress is too low, it is not able to support and stabilize the printed constructs while too high of a yield stress would hinder the needle movement. The yield stress of the supporting bath materials should also be at least an order of magnitude lower than that of the inks, thus allowing fine deposition of filaments in the supporting bath and preventing breakup of the printed filaments.[29,35] Luo *et al.* have found that a 5 wt% Poly(ethylene oxide) (PEO)-2m supporting bath with a zero-shear viscosity of 38 Pa·s and a yielding stress of 78 Pa facilitates the needle movement, inhibits ink dragging, and supports the extruded structure composed of 3 wt% poly(acrylic acid) and 0.05% dextran.[32] Second, the modulus of the supporting bath material should be high enough to support the printed threads, and the viscosity of the ink and the supporting bath material should be comparable. If the ink's viscosity is much higher than that of the supporting bath material, the printing needles will drag the extruded threads. On the other hand, if the viscosity is too low, the extruded thread will break.[32] Third, the density differences between the supporting bath material and the ink are supposed to be small enough to postpone the breakup and settlement of the extruded structure caused by gravity.[32] Fourth, low interfacial tension between supporting bath material and ink is preferred to hinder the deformation of the printed structures.[29,32] Fifth, osmolality difference between the ink and bath material could cause the swelling or shrinking of the printed structure. That is to say if the osmolality of ink is much lower than that of the bath material, swelling is observed.[32] Last, in terms of granular supporting bath, the microparticles size and distribution are vital to the successful printing of high-resolution architectures. The size of the microparticles influences the surface morphology of the

extruded filaments. “Spurs” are formed in between the microparticles and help bridge filaments.[26,33] It has been found that the smaller (larger than 1 μm) and more uniform microgel supporting medium, which possesses a lower stiffness, viscosity, and yielding stress, exhibits higher resolution structures than those fabricated within larger granular gels (**Figure 1.3**).[26,30,31]

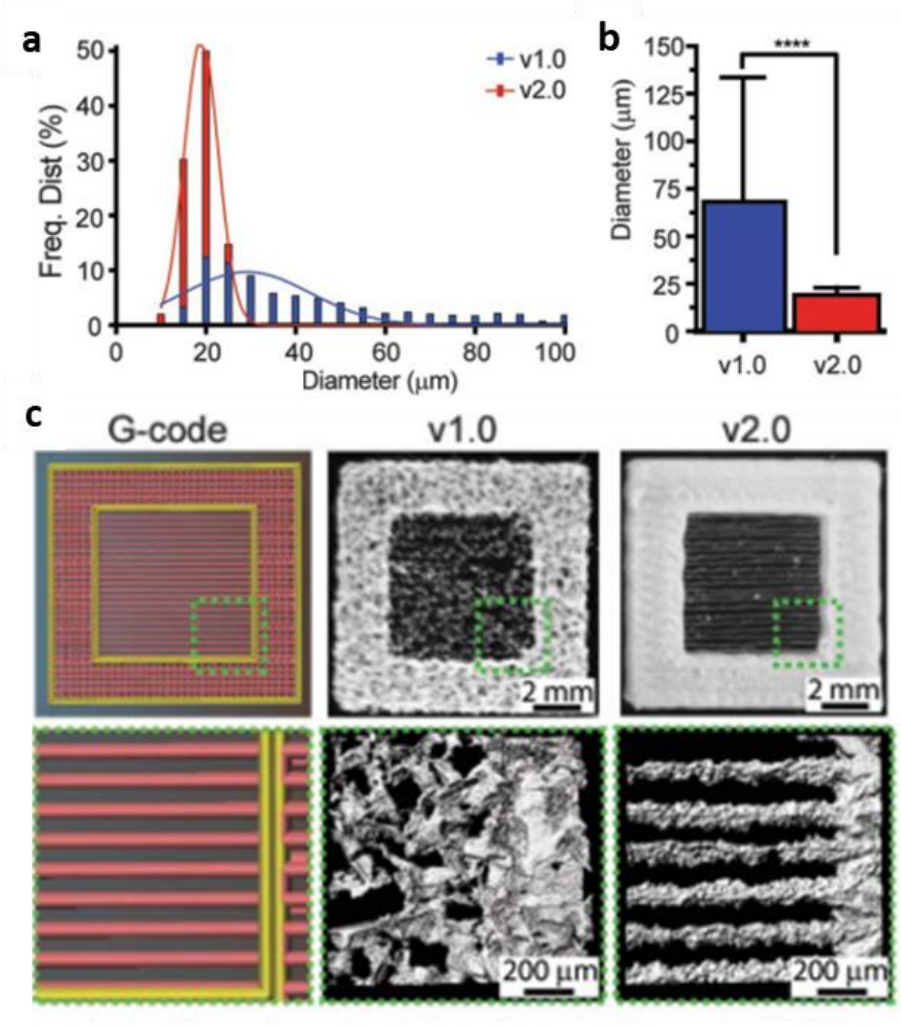

Figure 0.3 Characterizations of gelatin microparticle supporting bath material. (a) Diameter distribution and (b) mean diameter for two versions of gelatin slurry. (c) Comparison of the G-code and printed filaments by gelatin v1.0 and v2.0. Reproduced from Ref. 26.

Table 0-2 Properties of the supporting bath materials and bioinks

Property	Supporting bath material	Bioinks
Yield stress	78 Pa[32] 3-4 Pa[29] 0.63-5.3 Pa[36] 70 Pa[37] 1-200 Pa[30]	0.2-1 Pa[32]
Elastic modulus	64 Pa[30] 100-300 Pa[29,31,36] <500 Pa[33] 2000 Pa[26]	1-200 Pa at 1 Hz[30]
Microparticle size	~25 μm[26] ~55 μm[33] 7μm[30]	
Viscosity	38 Pa s[32]	0.1-0.5 Pa[32]
Density difference	20 kg/m^3 [32]	
Interfacial tension	Low 13.1 ±2.2 mN/m [29] 0.04 mN/m [32]	
Osmolality	35 mOsm/kg[32]	2 mOsm/kg[32]

Several groups have been working on developing the granular supporting bath materials for embedded printing as shown in **Figure 1.4**. Jeon *et al.* developed an alginate-based microgel supporting bath, in which cell pellets could be printed directly and maintain long-term differentiation (**Figure 1.4a**).[31] Feinberg's group developed two versions of gelatin slurry which serve as the supporting bath media to rebuild a human heart and found that constructs with high-resolution could be acquired in a smaller and more uniform gelatin slurry (**Figure 1.4 b-e**).[26,33] Hierarchically large-scale constructs can also be printed with high accuracy, resolution and fidelity by using a granular gel supporting bath. Bhattacharjee *et al.* used Carbopol ETD 2020 polymer incorporated with photoinitiatior as a granular gel medium to successfully print various complex structures, such as octopus, jellyfish, and branched tubular networks (**Figure 1.4 f-i**).[30] Noor *et al.* developed an alginate

microgel and xanthan gum supporting bath medium to support the printing of large and complex structures (e.g., hollow balls and hand) as shown in **Figure 1.4 j, k**.[38]

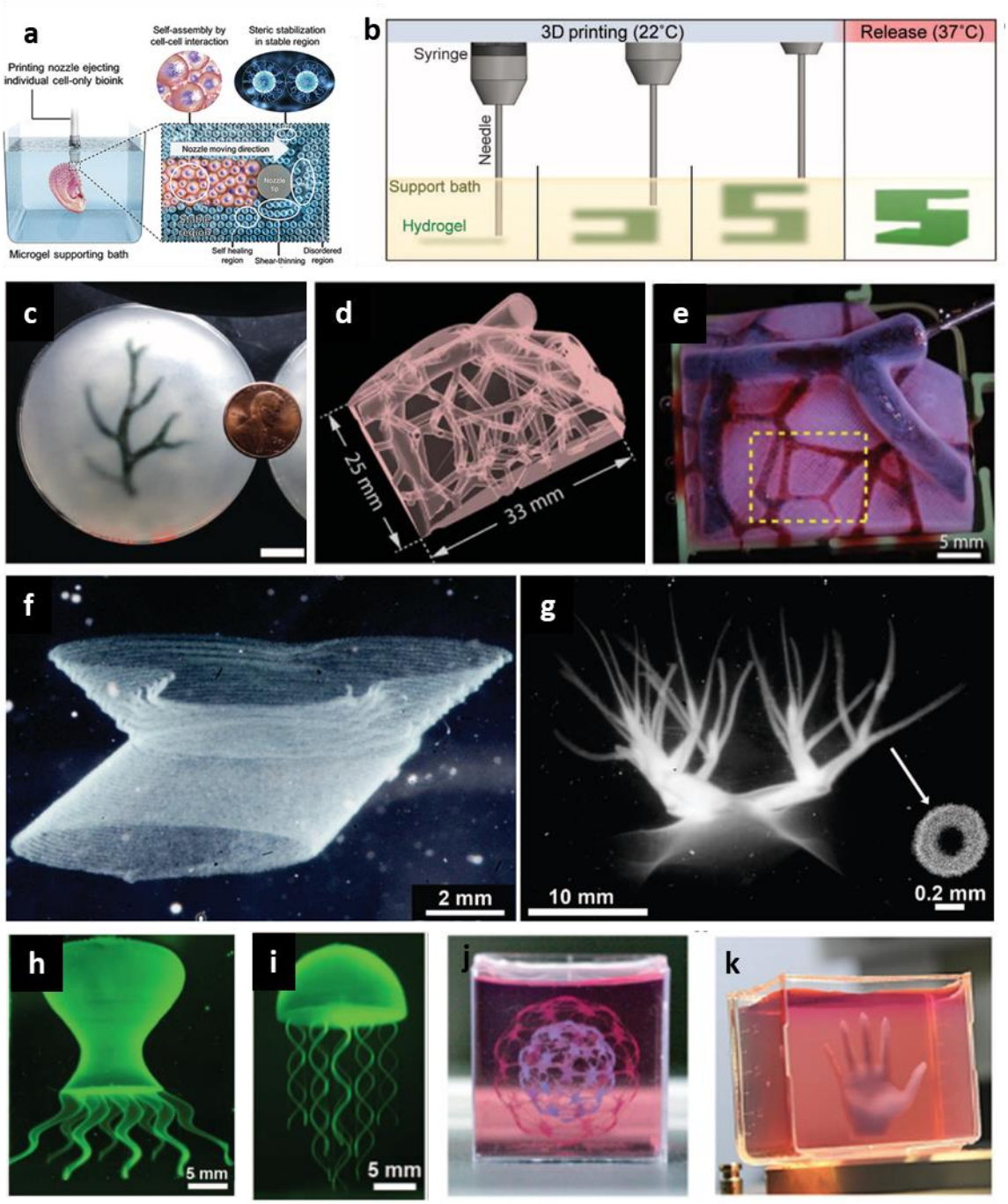

Figure 0.4 Embedded printed constructs in granular supporting bath. (a) A schematic illustration of 3D bioprinting cell pellet within alginate-based supporting bath. (b) A schematic illustration of the process of embedded printing and release of the printed hydrogel from the gelatin supporting bath.

(c) An arterial tress embedded printed in alginate (black) within a gelatin slurry bath. (d) The design of vascular network. (e) Interconnectivity test by perfusing the printed vascular network with glycerol (red). (f, g) Hierarchically branched tubular networks and fluorescent images of (h) octopus and (i) jellyfish models printed in Carbopol ETD 2020 polymer. (j, k) Large-scale structures printed within xanthan gum-alginate hybrid supporting bath. Reproduced from Ref. 26, 30, 31, 33, and 38.

1.2 Biomaterials for Bioprinting

Tissue engineering (TE) is a multidisciplinary and interdisciplinary field of biological science and engineering,[16,17] Conventionally, cells are harvested from a patient, followed by proliferating, migrating and differentiating *in vitro* to create an engineered tissue.[39–43] The autologous cell-incorporated scaffold is then utilized for transplantation with no adverse response, thus making this approach a safe option for tissue regeneration.[39] Recent development of 3D bioprinting illustrates the feasibility to fabricate advanced patient-specific scaffolds. Relatively simple tissues are also successfully produced, such as cartilage, skin, and bones.[7] However, the development of optimal bioinks is still one of the challenges.

The extracellular matrix (ECM), composed of a variety of proteins and macromolecules, provides a supportive scaffold for cellular growth and partly interacts with specific cell surface molecules. For example, integrin helps to transmit information from ECM to cells and synergize with other cell surface molecules to regulate migration, proliferation, or differentiation.[44] In addition, the filamentous nature of ECM affects the structural anisotropy and physical properties, thus influencing the cell growth, migration, and differentiation.[45] Therefore, biomaterials should be able to reproduce

the physiological ECM with biodegradability, biocompatibility, cell attachments, and comparable mechanical strength to human tissues.[20,46–50] Besides the required properties for TE, the biomaterials must meet the requirements for ME bioprinting. Strong shear-thinning biomaterials are good candidates because they have high viscosities at low shear rates, which allows hydrogels to form intricate patterns when being extruded and while at high shear rates, they can easily flow through the needle without clogging due to the low viscosity and reduce shear stress that can lead to cell damage.[25,28,51–53] Moreover, the printed scaffold should be mechanically strong enough to avoid collapsing during printing and be able to obtain constructs with a high resolution and aspect ratio. Furthermore, instant gelation after deposition or partially pre-gelled hydrogels are also preferred to ensure high structural integrity.[9,54]

To accommodate the mentioned requirements, potential bioinks involving physiological, biochemical, or mechanical cues have been investigated, including natural polymers, synthetic polymers, and nano-bio materials.

1.2.1 Natural Polymers

Natural polymers, such as alginate, gelatin, collagen, agarose, and fibrin, have been studied because of their similar properties to human ECM.[55–58]

1.2.1.1 Alginate

Alginate, a natural linear polysaccharide, is composed of (1,4) β-D-mannuronic (M) and α-L-guluronic (G) acid residues.[59–62] It contains three kinds of blocks, namely, MM-blocks, GG-blocks and MG-blocks. The MG-blocks are the most flexible parts of the polymer chains and the MM-block create

less stiff regions.[60,63] GG-blocks are able to form a cooperative "egg-box structure" by trapping divalent cations (e.g., Ca^{2+}, Sr^{2+}, Ba^{2+}). Due to the easy gelatin method, biocompatibility, and high viscosities, alginate has been used as the main material for bioprinting. Wu *et al.* developed a bioink composed of alginate and cellulose nanocrystals to bioprint a liver lobule-mimetic honeycomb structure with a cell viability over 65% for three days.[64] However, the absence of cell attachment sites hinders its application in 3D bioprinting, thus Arg-Gly-Asp (RGD)-motifs-modified alginate is gaining much attention and other natural biomaterials, such as gelatin, need to be added into alginate.[65–67] In order to better improve cell functions, alginate hydrogels can also be decomposed by using Ca^{2+}-chelating agent, thus providing enlarged pores and lower mechanical strength which is favorable for cell growth. [68,69] It was found that physically crosslinked alginate hydrogels lost over 60% of their initial mechanical strength after being exposed to a physiological buffer caused by the ion exchange of divalent and monovalent ions from the surrounding environments.[61,70–72] Zhu *et al.* combined alginate with gelatin to generate biomacromolecular network by chemically crosslinking gelatin with genipin and physically crosslinking alginate with $CaCl_2$ solution followed by dissolving away alginate via ethylenediaminetetraacetic acid (EDTA). The enlarged porous structure leads to improved cell behaviors (**Figure 1.5a**).[73]

1.2.1.2 Collagen

Collagen is the major composition of the basement membrane with at least 19 types, making ti attractive to TE.[74–76] It contains large amounts of glycine, proline, and hydroxyproline residues. The three basic polypeptide chains wrap around one another and form a three-stranded structure through hydrogen and covalent bonds.[77] The strands can also self-aggregate to form stable fibers by

changing temperature, pH, or ionic strength.[78] The gelled collagen can be readily degraded by metalloproteases, specifically collagenase and serine proteases, so degradation of the fiber in engineered tissues can be controlled. Yeo *et al.* fabricated microsized core-shell mesh structures composed of a core (cell-encapsulated collagen) and shell (pristine alginate) region, and outstanding cell viability (91%) in collagen was achieved as shown in **Figure 1.5b**.[76] Lee *et al.* used collagen and human stem cell-derived cardiomyocytes to embedded print a model of human heart. Collagen was gelled by adjusting the pH of the supporting bath. Cell viability was found to be 96%, and the ventricles contraction were observed at 4 days post-printing.[26]

1.2.1.3 Gelatin

Gelatin, produced from collagen through a denaturation process, has been widely used benefiting from the purity, low cost, and low antigenicity.[79,80] It is in the liquid form above 40 ℃ and reversibly forms an α helix structure below 30 ℃ by coiling its molecular structures.[81–83] Crosslinked gelatin can provide an ECM-like microenvironment for cells to embed in. However, the property that gelatin tends to liquefy at high temperatures (~ 37 ℃) dramatically hinders its application in bioinks. Hence, gelatin methacryloyl (GelMA) derived from gelatin with methacrylamide or methacrylate groups has been used to ensure easy solidification of the printed constructs without liquefaction at body temperature.[84] Moreover, the physical properties, such as mechanical strength and viscosity, of the photocrosslinkable GelMA can be easily tuned by tailoring the degree of substitution (DOS). Furthermore, hydrogels made of low concentrations of GelMA with a low DOS improve the cell viability and facilitate cellular organization.[85,86] Khademhosseini's group have been using GelMA as the main biomaterial for 3D bioprinting for years, and improved cell growth and proliferation were

observed by tuning the concentrations of GelMA and the type and crosslinking mechanism of the auxiliary biomaterials (e.g., carbon nanotubes and grahene oxide).[86–88] Wang *et al.* blended gelatin with GelMA and encapsulated human umbilical vein endothelial cells (HUVECs) to fabricate hollow microfibers via a coaxial needle (**Figure 1.5 c.i**). The addition of gelatin helped improve the fidelity of the hollow constructs. Furthermore, the encapsulated HUVECs showed great proliferation (**Figure 1.5 c.ii**).[89]

1.2.1.4 Hyaluronic Acid

Hyaluronic acid (HA) is the simplest polymeric glycosaminolglycan composed of a repeating disaccharide of (1-3) and (1-4)-linked β-D-glucuronic acid and N-acetyl-β-D-gulcosamine units.[77] HA is found in almost every mammalian tissue and fluid to help maintain homeostasis. Antich *et al.* combined HA with alginate to fabricate cell-laden artificial articular cartilage and found the addition of HA enhanced the expression of chondrogenic gene markers (**Figure 1.5d**).[90] Abundant carboxyl and hydroxyl groups on HA help ease its chemical modification. Rodell *et al.* have synthesized cyclodextrin modified HA and adamantane modified HA to assemble guest-host supramolecular gels. Secondary covalent crosslinking via addition of thiols and Michael-acceptors on HA increases the moduli and stability of the hydrogel, suggesting its potential use in TE.[91]

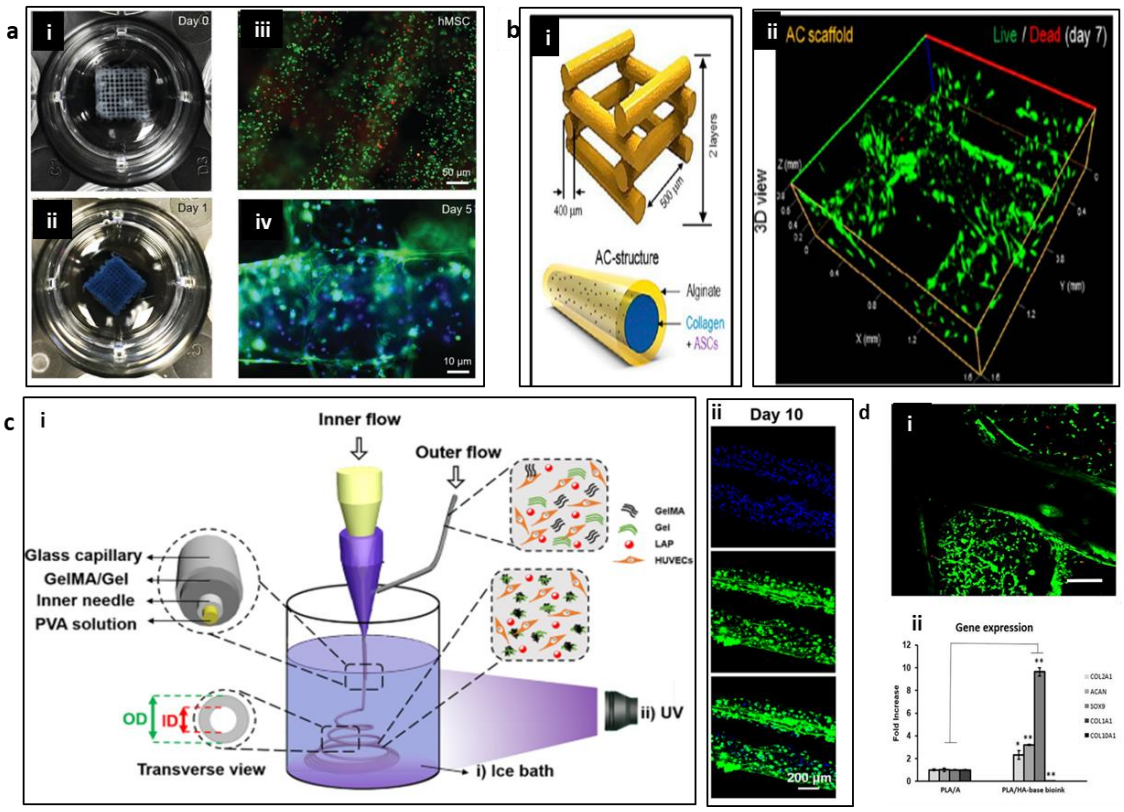

Figure 0.5 Examples of natural materials used in bioprinting. (a) Bioprinted five-layer mesh structure with alginate and gelatin at (i) day 0 and (ii) day 1; Fluorescence images with (iii) live/dead staining at day 0 and (iv) F-actin/nuclei staining at day 5 of the embedded human Mesenchymal Stem Cells (hMSCs). (b-i) Schematic illustration of mesh structures with core-shell bioprinting alginate in the sheath and human Adipose Stem Cells (hASCs)-laden collagen in the core. (b-ii) Fluorescence images showing live/dead staining of hASCs at day 7. (c-i) Schematic image of the setup to generate hollow microfibers with GelMA/gelatin blend solution in the shell and PVA in the core. (c-ii) Fluorescence images showing CD31/nuclei staining of HUVECs at day 10 post-printing. (d-i) Chondrocytes growth (green: live, red: dead) in HA-based bioink 4 weeks post-printing; (d-ii) Gene expression levels of chondrogenic markers in the bioprinted construct. Reproduced from Ref. 73, 76, 89 and 90.

1.2.2 Synthetic Polymers

Although naturally-derived polymers can reproduce the physiological environment for cells, the poor mechanical properties and difficulties in controlling the structural integrity limit their application in TE.[9] Therefore, synthetic polymers, such as polyesters, polyanhydride, polyorthoester, polycaprolactone, polycarbonate, and polyfumarate, are receiving increased attention due to their ease of control on mechanical and rheological properties.[92] However, synthetic polymers might possess poor biodegradability and cannot be used for soft tissues. In addition, synthetic polymers lack the biological cues inherent in a variety of natural polymers, such as the lack of active binding sites, that can lead to low cell viability.[93] Hence, efforts have been recently devoted to developing hybrid biomaterials to overcome the challenges in organ fabrication.

Hydrophilic polymers, such as poly(ethylene glycol) (PEG), with excellent solubility are ideal for tissue engineering.[17] PEG can be modified to form linear or multi-arm polymers, showing different properties including mechanical strength, stability of the crosslinked matrix, and their influence on cellular functions. Xue *et al.* fabricated 3D octahedral model with various stiffness by adjusting the crosslinking time of linear Poly(ethylene glycol) diacrylate (PEGDA) via digital light processing (DLP)-based 3D printing (**Figure 1.6a**). The growth and proliferation of the seeded fibroblasts were observed on the surface of PEGDA after being treated with poly-D-lysine (**Figure 1.6b**).[46] Jia *et al.* blended poly(ethylene glycol)-tetra-acrylate (PEGTA) with alginate and GelMA to prepare a bioink for vascular structure formation as shown in **Figure 1.6c**. PEGTA introduced the shear-thinning behavior and improved the mechanical strength of the constructs. In addition, the branched PEGTA improved the biomolecule diffusivity and pore size, allowing improved cell growth and proliferation (**Figure 1.6d**).[69]

By increasing the arms of branching PEG-based polymers, Pi *et al.* found the eight-arm PEG acrylate with a tripentaerythritol core could further enhance the mechanical strength and provide a favorable physicochemical environment for cell proliferation.[94]

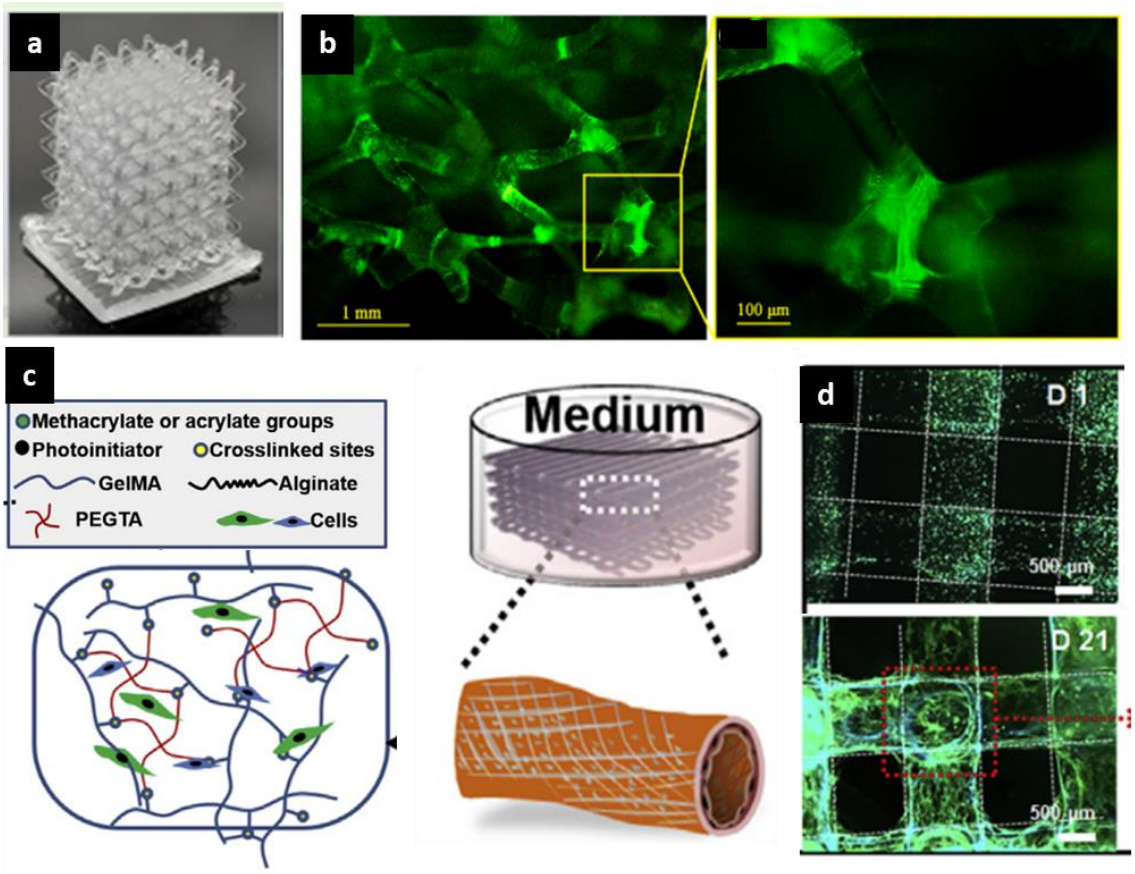

Figure 0.6 Examples of PEG-based hydrogels used in bioprinting. (a) 3D printed PEGDA octahedral model via DLP-based printing method. (b) Fluorescent images of the distribution of fibroblasts on the frame surface. (c) Schematic illustration of the composition of PEGTA-involved vascular structure. (d) F-actin/nuclei stained HUVECs within the bioprinted scaffolds at day 1 and day 21. Noticeable cell spreading from spindle shape to long strip-like shape was found over time. Reproduced from Ref. 46 and 69.

Pluronic 127 is another common polymers used in tissue engineering. It is a triblock copolymer

composed of a hydrophobic poly(propylene) (PPO) segment and two hydrophilic PEO segments in a PEO-PPO-PEO configuration. Pluronic 127 shows thermoreversible gelation behaviors when its concentration is above its critical micelle concentration. The gelled Pluronic F127 liquefies when temperature lowers to 4-5 ℃, thus commonly being used as a sacrificial biomaterial. F127 serves as a fugitive material in the core with other biomaterials, such as GelMA-involved bioinks or F127-bisurethane methacrylate (F127-BUM), in the sheath to fabricate hollow structure (**Figure 1.7a**).[55,95–97] F127 can also be blended with other biomaterials to form a physiological environment and be removed later to generate desired porous structure and thus promoting cell growth. Armstrong *et al.* have demonstrated the feasibility of 3D printing Pluronic-alginate multicomponent bioinks.[2] With the addition of Pluronic F127 in alginate, the hybrid bioink showed improved shear thinning behavior, compressive modulus, and shear modulus. The incorporation of Pluronic F127 into alginate matrices also increased the porous architecture because the fugitive Pluronic F127 were then removed after the engineered scaffolds formed (**Figure 1.7b, c**). No significant loss in the viability of the encapsulated hMSCs was observed over a 10-day period.[2] This indicates that the fugitive ink did not only provide a microscopic structure formation, but also template a macroscopic structure.

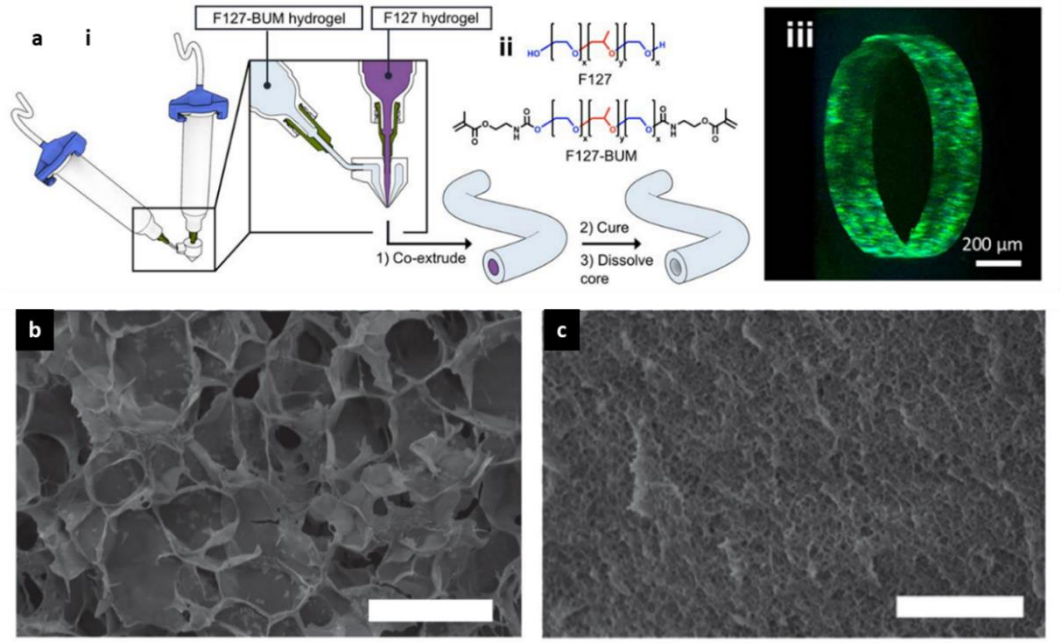

Figure 0.7 Examples of F127-based hydrogels used in bioprinting. (a-i) Schematic illustration of the tubing fabrication process by using (a-ii) F127 as the core materials and F127-BUM as the shell material. (a-iii) Confocal image of HUVECs seeded on the surface of collagen I-treated F127-BUM tubing. Scanning electron micrographs of the porous structures produced by (b) F127-alginate hybrid gels and (c) pure alginate gel. Reproduced from Ref. 2 and 55.

Polyvinyl alcohol (PVA) has been widely used in various areas, including tissue engineering, foods, lacquers, resins, drug delivery, and cosmetics industries due to its high water content, low frictional behavior, and biocompability.[98–100] The elasticity of PVA materials is similar to that of the human artery, making it uniquely suiabtle for constructing vascular phantoms. The abundant hydroxyl groups on the backbone of PVA not only make them hydrophilic but also increase the viscosity and elasticity of PVA solution over time which is caused by H-bonding.[101] The hydroxyl groups can boost the intermolecular interactions between PVA and collagenous proteins, hence Choi *et al.* developed a granular supporting bath composed of gelatin and PVA to promote the feasibility and fidelity of

embedded printing decellularized ECM (dECM).[34] PVA is crosslinked either physically (e.g. through free-thaw cycles), or chemically using crosslinkers such as glutaraldehyde, epochlorohydrin, and boric acid.[99,102] By increasing molecular weight, concentration, and cycles times, crystalline gels with improved crosslinking density, elastic strength and less water uptake capacity are formed.[103] The physically crosslinked PVA aerogel, driven by the phase separation, benefits from the low cytotoxicity but with poor mechanical properties and structure stability.[99,103] In comparison, the chemical crosslinkers, such as glutaraldehyde, epochlorohydrin, and boric acid are typically cytotoxic. Therefore, photo-responsive PVA, which renders chemically crosslinked gels that are stable and biocompatible, is favored for tissue engineering and medical applications. Glycidyl methacrylated PVA (PVAGMA) has attracted much attention recently. Transesterification and epoxide ring-opening are the two mechanisms that explain the reaction between hydroxyl groups of PVA with glycidyl metharylate (GMA). At pH 3.5, the GMA undergoes epoxide ring-opening while at pH 10.5, a hydrolysis process occurs, and both mechanism routes are involves but ring-opening is a preferred reaction.[104] Chen *et al.* have been found that PVAGMA solution is semitransparent with a DOS higher than 3%, and it cannot be dissolved in water if the DOS is larger than 12% which is caused by the high density of the hydrophobic methacryloyl groups.[105,106] DOS influences the mechanical and swelling properties of the PVAMA hydrogels as well. Zhang *et al*. found that the crosslinking density of PVAGMA is reversibly proportional to the fracture strain and the ultimate compressive strength, but proportional to the compressive strength.[107] Additionally, PVAGMA with a higher DOS lowers the swelling ratio.[99,107] Further, cell studies revealed that PVAGMA is biocompatible but without cell attachment sites.[107]

1.2.3 Nano-bio Materials

Hybrid bioinks composed of natural and synthetic polymers have been widely used in ME bioprinting to compensate for the limitations of each component. Briefly, the synthetic polymers provide appropriate mechanical properties, and the natural polymers provide suitable biological microenvironments. Bioactive compounds, like peptide and growth factors, are added or grafted to the polymer networks to improve cell behavior. The peptides provide binding sites for the cells to attach, whereas the growth factors induce cell differentiation to develop into a specific tissue. Additionally, polymer are typically strain-softening whereas human soft tissues exhibit strain-stiffening behavior. By mixing polymers with nanomaterials, such as graphene-derivatives, carbon nanotubes (CNT), cellulose nanocrystal (CNC), and methacrylate silica nanoparticles, the issues can be addressed.[108] The nano-fillers not only improve mechanical properties but also help improve cell functions in the hybrid biomaterials.[110–114] In addition, the incorporation of nanofibers, such as CNCs, cellulose nanofibres (CNFs), and chitin nanocrystals, into the polymer helps to provide a fibrous environment which is the nature of ECM and influence its biophysical and biochemical properties.[45]

1.2.3.1 Carbon-based Nanomaterials (CBNs)

Carbon-based nanomaterials (CBNs) have attracted tremendous attention in the last few decades in biomedical field, especially in drug delivery, biosensing, and tissue engineering, due to the attractive electrical, mechanical, thermal, and chemical properties. CBNs include fullerenes, CNT, graphene and its derivatives, nanodiamonds, and carbon-based quantum dots.[113] Photoluminescent carbon dots (CD), which are small carbon nanoparticles with a size less than 10 nm have been used in nanomedicine because of well dispersibility in water, high cell membrane permeability, and

biocompatibility. Human vascular endothelial growth factor (VEGF)-linked CDs not only preserve its angiogenic property but also allow noninvasive detection of HUVECs.[114] Two commonly used CBNs in regenerative medicines are CNT and graphene, and their characteristics, such as biocompatibility, mobility, conductivity, and Young's modulus, have been investigated. CNT is made of a graphite sheet rolled into a tube with a diameter of 1 nm while graphene is one-atom-thick single layer of sp^2 carbon atoms, and both possess strong tensile strength and modulus.[115,116] However, poor solubility of CNT and graphene in water limit their use in biomedical applications, therefore various derivatives, like graphene oxide (GO) and reduced GO (rGO) have been synthesized to improve their dispersibility and biocompatibility, making them effective candidates for biomedical application.

Recent research have been conducted on graphene-derivatives or CNTs-incorporated hydrogels to demonstrate their applications in tissue engineering. A small addition of CBNs enhance the mechanical strength due to their rigid nature.[117] Shin *et al.* demonstrated that the addition of CNTs in GelMA increased the compression modulus from 10 kPa, without CNTs, to a maximum of 32 kPa with a small amount of CNTs (3 mg/mL).[58,109,110] Additionally, CNTs increased the hydrogel pore size without changing the porosity of the polymeric matrix.[58,118] Cha *et al.* found that the incorporation of GO in a low-to-moderate dosages range in GelMA polymer network remained high cell viability and proliferation rate.[110] Furthermore, owing to the optimal electrical property, CBNs are able to mediate electrical signals in biological system, such as cardiac and neural tissue.[116]

1.2.3.2 Cellulose Nanocrystals

Cellulose is the most abundant substance on earth and considered as an inexhaustible source of raw materials.[119,120] It is a linear syndiotactic homopolymer composed of β-(1, 4)-glycosidic bonds

linked D-anhydroglucopyranose.[119–127] Cellulose nanocrystals (CNCs), rod-like or whisker-shaped nanoparticles with an average diameter of 5-10 nm and an average length of around 100 nm, is extracted from cellulose either being subjected to mechanical and chemical treatments, such as acid hydrolysis (**Figure 1.8a, b**).[119,128] The species of acid influence CNCs' dispersibility and stability. CNCs extracted by sulfuric acid demonstrates high water solubility due to the highly negatively charged sulfate ester surface.[129]

CNCs possess some promising properties such as renewability, low density, high mechanical strength, large and highly reactive surface (250 ~ 500 m^2/g), and low cytotoxic response. The van der Waals force and intermolecular hydrogen bonds promote the stacking of cellulose chains that cause the CNCs' crystalline structure. Due to its high crystallinity, CNCs exhibit an axial elastic modulus ranging from 110 to 220 GPa and a tensile strength ranging from 7.5 to 7.7 GPa.[119] Thus, CNC is commonly utilized to enhance mechanical strength of gels. Furthermore, the rheological property of CNC suspensions is another promising property for 3D bioprinting (**Figure 1.8 c-e**). The shear thinning behavior is observed due to the alignment of the chiral nematic liquid crystalline domains.[129–131] Xu *et al.* mixed 2,2,6,6-tetramethylpiperidine-1-oxyl (TEMPO)-oxidized CNF with GelMA to 3D print mesh structures. The biocompatible scaffolds showed improved structural stability and mechanical strength due to the presence of TEMPO-oxidized CNF.[132] Wu *et al.* found the addition of CNCs improved the shear-thinning properties of alginate, making it possible to print alginate/CNCs hybrid bioinks with high cell viability (**Figure 1.8f**).[64]

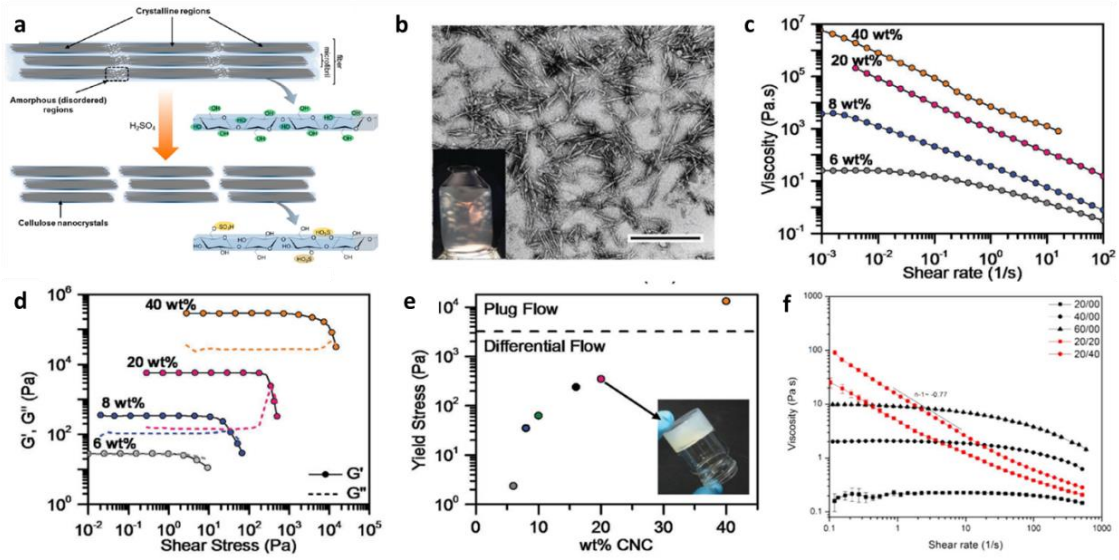

Figure 0.8 Characterizations of CNCs. (a) Schematic showing cellulose fibers containing alternate crystalline and amorphous regions and negatively-charged CNCs after removing the amorphous regions of cellulose fibers through acid hydrolysis. (b) Transmission electron image of CNCs (scale bar: 500 nm). (c) Steady-shear and (d) oscillatory rheological measurements of CNC suspension. (e) Yield stress of CNC inks. (f) Flow curves of five different alginate/CNC (in mg/mL) bioink formulations. Reproduced from Ref. 64, 119, and 131.

1.3 Bioprinted Tissue Structures

Tissue engineering and regenerative medicine are new approaches to develop engineered artificial tissues for clinical translation, disease studies, and drug delivery. The conventional 2D monolayer cell culture lacks the physiologically dynamic and complicate cell-cell and cell-ECM interactions, thus 3D bioprinting has emerged to fabricate functional tissues. To date, the most medical applications of 3D printing have involved non-living constructs that function as structural or space-filling prostheses, such as orthopaedic devices, surgical tools, and maxillofacial implants because it can provide optimal accuracy and produce patient-specific devices compared to traditional

intraoperative methods.[7] Although advanced 3D tissue models have been successfully fabricated, such as skin, bone, cartilage, bone, liver, kidney, lung, and heart,[21–23,133] main challenges still exist including the selection of suitable biomaterials and cell sources, tissue complexity, and manufacturing time and scalability.[7,22]

Currently, various mini-tissue constructs that structurally mimic native tissue and organs have been successfully bioprinted via different 3D printing techniques. The small-scale tissues only contain one or two cell types with limited functionality. Research is mainly focused on the shape and size, tissue organization, or functional inner structures separately instead of the recreation of whole organs that recapitulate the anatomy and physiology of the organ.[22] For instance, multilayered skin tissue can be 3D bioprinted via *in vitro* or *in situ* strategies with great complexity and accuracy. A layer of fibroblast-laden hydrogel was first printed followed by the deposition of a second layer of keratinocytes-encapsulated hydrogels to mimic the architecture of native skin.[22] However, functional large scale tissues with physiological heterogeneity that fully mimic the morphological, biochemical, and physiological properties have not been bioprinted yet. This is mainly due to the complex nature of human tissue and organs. For instance, the oxygen and nutrient diffusion distance is limited to 100-200 μm, thus vasculature is required when fabricating large tissues to sustain cell survival.[227] Therefore, essential functional elements like vasculature, innervation, and diversity of cells should be considered when designing tissue models. Noor *et al.* have successfully generated thick, perusable vascularized cardiac patches with proper functions, which demonstrates that 3D bioprinting is a potential approach to engineer vascularized tissues that mimic biochemical microenvironment.[38] However, with current technology, the complex hierarchical 3D architecture of a multi-scale vascular

system including capillaries in micrometer scale and arteries in millimeter scales cannot yet be recapitulated.[7,134]

In addition to the tissue complexity, identification of suitable printable biomaterials hinder the development of 3D bioprinting because they affect long-term cell functionality, printability, shape fidelity, and structural resolution. Currently, ideal biomaterials that meet all the requirements have not been established yet. Firstly, the biocompatible inks should be able to reproduce the functional and biomechanical properties of the target tissue or organs, such as comparable mechanical strength, proper degradation rate, and physiological interactions with cells. The potential solutions to these requirements could be using ECM-based hydrogel, modifying biopolymers with peptides, and combining natural and synthetic biomaterials.[7,20,135] Secondly, the printable biomaterials should be easily extruded without damaging cells and rapid solidification post-printing, thus viscosity is a vital factor in developing bioinks. Shear-thinning bioinks are preferred because it can shield the stress on cells during the extrusion process and maintain shape fidelity after deposition due to the high static viscosity.[7] Simply increasing the polymer concentrations can increase the ink viscosity but with poorer enhanced shear-thinning properties when compared to that of the ink compositions composed of nanofillers and polymers,[64] therefore hybrid inks containing nanomaterials are widely developed as the printing materials.

As the primary and important composition in bioinks, cells need to be considered as well. Cells are homogeneously distributed in the bioink, allowing precise deposition to construct living architectures. Current 3D bioprinted tissue only contains small amount of cells and cell types. However, a large amount of tissue-specific cells and phenotypes is required to recreate the whole

organ. Primary cells and stem cells can be good choices. Although stem cells are more sensitive to the environmental stimulation, such as the shear stress during printing, it is better to use it for fabricating large-scale tissues because it can differentiation into different tissues by precisely incorporating growth factors or inducerons, thus decreasing the complexity of the printing process.[23] Additionally, maintaining high cell viability in large-scale bioprinted tissues and organs within the initial layers will be a challenge due to the long manufacturing time.

Despite the materials science and biology, hardware investigation and development are also critical to successfully construct functional tissues and organs. Essential printer working parameters including applied pressure, needle printing speed, extrusion flow rate, needle diameter, and layer height need to be considered to ensure optimal printing fidelity. Furthermore, only few number of bioinks can be used on a single printer due to the limited printer cartridges, which hinders the manufacturing time and scalability of the bioprinted structures.[23] Therefore the development of the bioprinter is necessary to accelerate the rate of bioprinting large-scale tissue with high cell viability.

In this project, we focused on the development of functional biomaterials, and two main soft tissue scaffolds, liver lobule and blood vessel, were chosen as models to investigate our developed inks.

1.3.1 Liver

1.3.1.1 Human Liver Anatomy

The liver, the largest and most metabolically complicated organ in the body, is located in the abdomen and performs multiple functions, such as detoxification, blood sugar control, protein production, and hormones synthesis.[136–138] The structural unit of liver is the hepatic lobule, which is

separated by a connective tissue, namely the vascular septum (VS). Each lobule is hexagonal in shape with a diameter of approximately 1 mm as shown in **Figure 1.9a**.[139,140] A portal triad, composed of portal vein, hepatic artery, and bile duct, is located at the vertices and a central vein sits in the middle of hepatic lobule. The major aspects of hepatic structure are the hepatic vascular system, the biliary tree, and the liver cell arrangements.

The liver is a dynamic vascular organ and stores 10-15% of the total human blood at any time. Unlike other organs, 75% of the liver blood supply is nutrient dense venous blood, entering into the liver from the portal vein while the remaining oxygenated blood supply enters from the hepatic artery as arterial blood. Blood then flows through the sinusoids to the central vein of each lobule and leaves the liver to the inferior vena cava. Sinusoids are distensible capillaries lined by fenestrated endothelial cells and in immediate proximity to the space of Disse, which borders the hepatocytes. A large amount of fluid and proteins in blood diffuse into space of Disse, providing a dominant portion of the body's lymph.[141,142]

The function of the biliary tree is to transport bile from the liver to the lumen of the small intestine. Bile is secreted by hepatocytes and fed into canaliculi, which are generated by the dilated intercellular space between adjacent hepatocytes. The direction of the canaliculi are antiparallel to the blood flow. Bile flows into the bile ducts through the canaliculi and leaves the liver.[141]

Each hepatic lobule consists of ECM, parenchymal cells, namely hepatocytes and cholangiocytes, and non-parenchymal cells as illustrated in **Figure 1.9b**.[143] Native liver ECM is mainly composed of fibronectin, proteins, collagens, glycosaminoglycans, and growth factors. The critical function of the ECM is to maintain the healthy phenotype of liver cells. The progressive changes in the composition

of the ECM affect the biofunctions of the parenchymal and the non-parenchymal cells and ultimately lead to chronic fibrogenic disorders. Hepatocytes are the main functional cells in the liver and account for approximately 80% of the liver mass and 60-70% of the total liver cells. [144] The cells radiate outward from the central vein in each hepatic lobule. They are in contact either with sinusoids or neighboring hepatocytes. Hepatocytes perform a variety of functions, including producing protein, lipid and very low density lipoproteins. The main non-parenchymal cells, including Kupffer cells, sinusoidal endothelial cells, and hepatic stellate cells, play an important role in supporting parenchymal cells and regulating hepatic functions.[145] The phagocytic Kupffer cells are populated in the sinusoids and are in charge of removing bacteria and microbes in the portal venous blood, preventing the attack during systemic circulation. Stellate cells, liver-specific pericytes, are located in the space of Disse and represent about 5% of the liver cells. In healthy liver, stellate cells are quiescent. Once liver is injured by toxins or viruses, stellate cells transform into an active state and secrete abundant ECM proteins, such as collagens, glycoproteins, and proteoglycans. However, the repeated insults may cause liver fibrosis and damage some liver functions. In addition to the critical role in liver regeneration, stellate cells store vitamin A.

The functional unit of the liver is the hepatic acinus, which is different from the liver lobule, and is not able to be seen under a microscope. It is oriented around the afferent vascular system in an ellipsoidal shape (**Figure 1.9c**). It is composed of three zones based on function and perfusion. Zone I is defined as the periportal region of hepatocytes and exposed to highest level of oxygenated blood and nutrients, thus making it least susceptible to ischemic injury and very sensitive to the viral hepatitis. Additionally, owing to its high perfusion, zone I plays a key role in oxidative metabolisms,

bile formation, amino acid catabolism and cholesterol formation. Zone III lies around the central vein with the lowest perfusion, thus cells in this zone is most sensitive to ischemic injury. It plays an important in lipogenesis, detoxification, glycolysis, ketogenesis, and xenobiotic biotransformation. Zone II sits between zone I and zone III and is considered as the regenerative region with the greatest number of oval cells.[146,147]

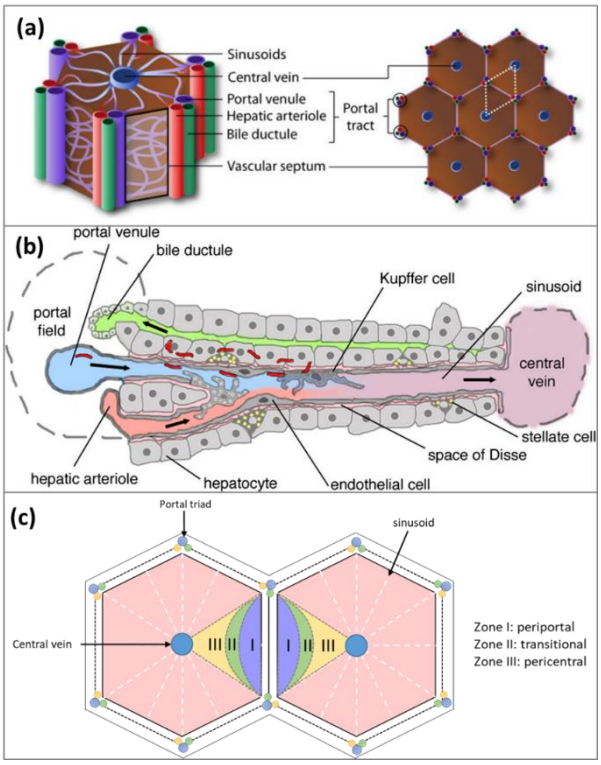

Figure 0.9 Human liver anatomy. Schematics of (a) liver lobule with a shape of hexagon prism and its vascular network, (b) detailed liver lobule composition, and (c) hepatic acinus. Reproduced from Ref. 140.

1.3.1.2 Liver Diseases

Liver failure is life-threatening and has become one of the leading causes of death worldwide. Although liver is highly regenerative and has a vital role in protecting the body from foreign antigens and microbes, drugs, toxins, or viruses can still cause damages to hepatocytes, leading to liver

failure.[148,149] Four main stages are included in liver failure: (i) inflammation, (ii) fibrosis/scarring, (iii) cirrhosis, and (iv) end-stage liver failure. Acute and chronic liver disease are the two types of liver disease. Acute liver disease (ALD) is a rapid loss of liver functions. The main causes of ALD include drug induced liver injury, hepatitis A, B, and E infections, Epstein-Barr virus, Wilson's disease, autoimmune hepatitis, and etc.[138] In comparison, chronic liver disease (CLD), a progressive destruction related to fibrogenic evolution, is potentially caused by hepatitis B or C infection, non-alcoholic fatty liver disease, alcoholic liver disease, and biliary obstruction. Liver injury activates stellate cells, accumulates fibrillar ECM, and alters the vascular architecture of the liver, which leads to cirrhosis.[150] Up to date, liver transplantation is the only long-term therapy to treat liver failure, but there is a shortage of donor organs. Additionally, artificial 3D systems are required for pathophysiological studies, drug screening, and hepatoxicity prediction. Therefore, research on artificial livers has been arisen to solve the problem.

1.3.1.3 Liver Tissue Engineering

Liver tissue engineering is mainly concentrated on the development of artificial liver tissue by arranging cells and biomaterials. An effective artificial liver should contain 10^{10} hepatocytes and be able to provide 10% of the liver function.[148] To maintain liver function, it should meet the requirements of a high oxygen level environment as well as ultralow shear stress experienced by the hepatocytes simultaneously. Different cell sources have been utilized for liver tissue engineering, including human or porcine primary hepatocytes, immortalized hepatocytes, human hepatic cell lines and stem cells.[148,151] To simulate *in vivo* conditions, ECM and co-culture hepatocytes with non-parenchymal cells are key factors because matched ECM and the addition of non-parenchymal cells

are able to extend the hepatocytes life and preserve liver functions.

Recently, many groups demonstrated the fabrication of liver tissues using various 3D printing methods and materials. Nguyen *et al.* mixed alginate and gelatin hybrid hydrogels with parenchymal and non-parenchymal cells to construct a piece of liver tissue via ME bioprinting. Ma *et al.* fabricated a liver lobule-mimetic architecture with hepatocytes and non-parenchymal cells in defined regions via dynamic optical projection stereolithography.[149,152,153] It was found that not only the co-culturing but also the spatial patterning of parenchymal and non-parenchymal cells influenced the liver physiologic function.[153] Co-culturing fibroblasts with hepatocytes has been found to support hepatic functions without physical contact.[139] Proliferation maker genes, such as albumin, α-fetoprotein, MKI67, hepatocyte nuclear factor 4α, α-1 antitrypsin, and transthyretin, and drug-metabolizing enzymes, like cytochromes are commonly measured to test the liver functions in an artificial liver model.[149,154] Current investigation on 3D printed liver models is mainly focused on the drug test with minimal consideration of hepatic anatomy, therefore, it is necessary to construct an engineered liver tissue that simulating native liver scaffolds with defined cell patterning.

1.3.2 Carotid Artery

1.3.2.1 Carotid Artery Anatomy

The arterial system is composed of two sub-systems based on functional and structural properties. Steadily-flowing blood is expelled to the peripheral circulation during heart diastole. The large elastic arteries store blood that is ejected from the heart and dampen flow pulsatility, while the muscular arteries, especially those of the lower limb, alter vascular tone and modulate the velocity of the pressure wave from the larger vessels upstream.[155,156]

In this project, the carotid artery, which is the major blood vessel that delivers blood to the brain, was studied. It is composed of common carotid arteries (CCA) with a 6-mm diameter, internal carotid arteries (ICA) with a 4.2-mm diameter, and external carotid arteries (ECA) with a 3.5-mm diameter as illustrated in **Figure 1.10a**.[157,158] Arteries are considered to be viscoelastic, rather than simply elastic. It contains elastin fibers which are known to possess an elastic effect, and also smooth muscle cells (SMCs) which introduce their viscous properties..[159,160] An artery wall consists of three layers, namely the intima, media, and adventitia (**Figure 1.10b**). The intima, the innermost layer of vessels, is composed of a monolayer of endothelial cells (ECs) that are bound to a basement membrane.[134,161] The function of the endothelial layer is to maintain a permeability barrier, regulate coagulation, and control blood flow.[161] VE-cadherin, Ki-67, and laminin are the main indicators of EC function. VE-cadherin is an adhesion-junction molecule between ECs and regulates vascular functions, and Ki-67 is a protein in cells and indicates cell division.[162] The media, composed of SMCs with fibers of elastic tissues located between the intima and the adventitia, controls the vessel diameter and vessel strength.[161] SMCs are to maintain the blood vessel tone and blood pressure through the contraction and relaxation process. It transforms from contractile to synthetic phenotype over time *in vivo*. α-Smooth muscle actin and smooth muscle-myosin heavy chain are two common contractile protein expression markers in testing the contractile function of SMCs.[163] The outermost layer of vessels is called the adventitia and is composed of ECM with fibroblasts and perivascular nerves.[161]

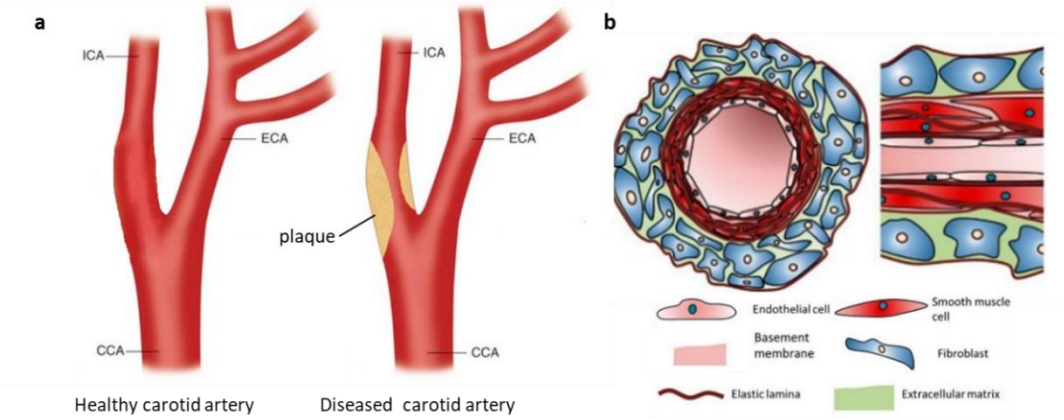

Figure 0.10 Schematics of human vessels. Schematics of (a) (left) healthy and (right) diseased carotid artery, and (b) blood vessels cell types and compositions. Reproduced from Ref. 134.

Cardiovascular disease (CVD), a disease associated with heart or blood vessels, has been a threat to human life over decades. CVD includes but is not limited to coronary artery disease, stroke, heart failure, and hypertensive heart disease. The main reason of CVD is the limited amount of blood flowing into the heart, thus leading to ischemia of the cardiac muscle cells. The mechanical and structural properties of the arteries play a critical role in determining cardiovascular health. Collagen and elastin in the intima-media are the proteins that influence vessel wall strength, elasticity, and compliance. Asymmetry between the synthesis and degradation of the two proteins contributes to arterial stiffening or softening. For instance, hypertension leads to an increase in collagen production and SMCs cross-section, but a decrease in elastin.[156,160]

Atherosclerosis and thrombosis have been observed in coronary artery disease. Atherosclerosis is caused by the fibrosis and the accumulation of calcium, lipids, and abnormal inflammatory cell. The deposition of calcium phosphate stiffens the arteries. In addition, as lipids accumulate, lipid pools are formed within the intima, which disrupt the cellular structure and break elastic fibers. Due to the intimal disorganization, new connective fibrous tissue are developed, forming plaque.[155] The build-

up of plaque (atherosclerosis) narrows the artery wall, increases wall stiffness, and decreases vascular compliance and arterial distensibility.[155,159] It occurs more likely at bifurcation vessels or high curvature vessels owing to the low or oscillating wall shear stress.[164] Decreased vascular compliance manifests in isolated systolic hypertension (i.e. systolic blood pressure higher than 140 mmHg and diastolic blood pressure lower than 90 mmHg).[155,156,160] The stiffening of the carotid arteries alters hemodynamic and mechanical conditions of the artery, impairs their cushioning function, reduces pulse wave reflection, and increases the pressure and flow pulsatility, which are transmitted into the cerebral circulation and can increase the risk of stroke.[155,156,159,160,164] Additionally, atherosclerosis causes obstruction to blood flow, thus leading to stress concentrations at the plaque shoulder and promoting vessel rupture.[155]

The most basic measurement of vascular stiffness is absolute distention, which is the difference between the systolic and diastolic diameter. By normalizing absolute distension to the diastolic diameter, vessel strain is obtained. It has been found that the mean carotid distension is 0. 360 mm-0.424 mm at plaque and 0.451 – 0.507 mm in adjacent healthy vessels.[155] Mechanical changes in the arterial walls is earlier than the structural changes, which can be detected as an increase intima-media thickness (IMT), which is the distance between two echogenic lines.[159] The IMT of a healthy carotid artery is typically 0.74 ± 0.14 mm, which is related with gender, age, and ethnicity.[157,165,166] An increase of IMT to above 1 mm or a focal thickening larger than 50% of the adjacent area is associated with high risk of cardiovascular disease such as atherosclerosis, myocardial infarction, and stroke.[166] Since arterial stiffening is an early marker of atherosclerosis, early diagnosis of vascular stiffness is necessary. It includes invasive tools (e.g. X-ray contrast angiography) and non-invasive imaging, such

as computed tomography (CT), magnetic resonance tomography (MRT), ultrasonography, or positron emission tomography scanning. Additionally, therapeutic interventions are required to alter the mechanical properties of arteries to treat CVD.[160]

1.3.2.2 Medical Carotid Artery Phantoms

Image-guided minimally invasive diagnostic imaging and therapeutic intervention techniques have significantly improved lives. They support accurate therapeutic procedure and help guide and monitor the intervention for optimal results. Ultrasound imaging, including B-mode imaging, Doppler imaging, contrast imaging, ultrafast imaging, functional ultrasound imaging, and ultrasound localization microscopy, has served as a tool in clinical practice.[167] Therefore, ultrasound, specifically, is widely used to image internal organs and aid in fluid management because it provides real-time, low-cost, and radiation-free imaging.[167] To develop next-generation medical ultrasound technologies, such as molecular imaging, the development of the scanners, and imaging-guided ultrasound therapy,[108,168] medical phantoms (i.e. models that mimic tissue and vascular properties) are highly desirable experimental devices, calibration tools, and training platforms because they can provide consistent results.[168] During the past decades, several groups were working on the fabrication of carotid arteries, including basic tubular structure, walled vascular phantoms, and wall-less phantoms via the traditional lost-core methods. Chee *et al.* developed walled vessels with serial levels of arterial stenosis by using 10 wt% PVA and 3 wt% graphite via the traditional mold method. The vessel wall motion dynamics of the fabricated phantoms is consistent with the pulse wave propagation in a real vessel wall (**Figure 1.11 A-B**).[158] They further developed vessel phantoms with varied regional wall stiffness and thickness and found local vessel distension was weakened in the regions with higher

wall stiffness and thickness (**Figure 1.11 C-D**).[169] However, the creation of application-specific phantoms with tailored acoustic properties, realistic geometrical configurations, and heterogeneous mechanical properties for advancing diagnostic ultrasonic techniques and exploring cardiovascular disease mechanisms still remains challenging,[170] thus in this project, I fabricated vascular phantoms and visualized them via ultrasound imaging.

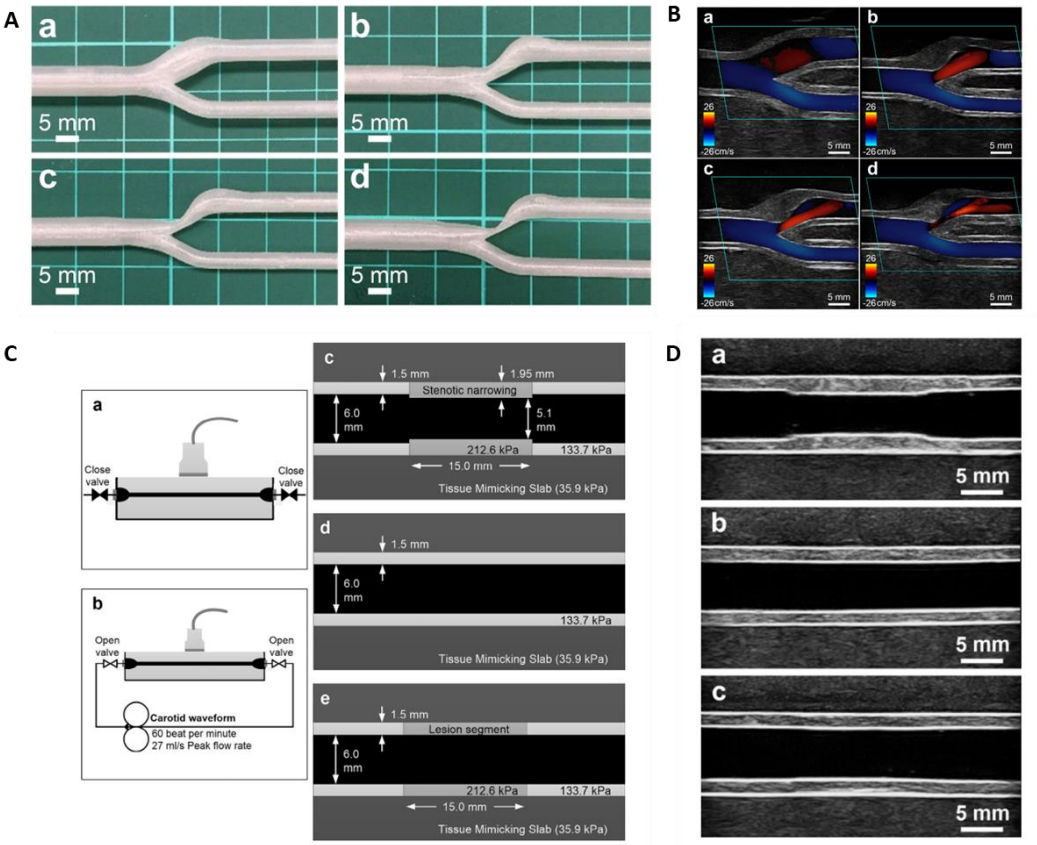

Figure 0.11 Ultrasonic characterizations of walled vessels made of PVA aerogel. (A) Images of the fabricated carotid bifurcation vessel phantoms with (A. a) healthy geometry and (A. b-d) diseased geometries with 25%, 50%, and 75% stenosis at the ICA inlet, respectively. (B) Clinical color flow image frames at pulse systole for (B. a) healthy geometry and (B. b-d) diseased geometries with 25%, 50%, and 75% stenosis at the ICA inlet, respectively. (C) Overview of the ultrasound imaging (a) without and (b) with a carotid pulse waveform and the design of three different models (c) stenosed three-

segment phantom, (d) single-segment phantom, and (e) unstenosed three-segment phantom. (D) B-Mode images of the three different phantoms (a) stenosed three-segment phantom, (b) single-segment phantom, and (c) unstenosed three-segment phantom. Reproduced from Ref. 158 and 169.

However, traditional phantom fabrication methods, such as the lost-core technique,[171] is complicated and time-consuming. Therefore, 3D bioprinting can be a promising alternative for the fabrication of complex functional phantoms. Techniques, such as CT and MRT, combined with 3D printing advance the design of 3D models. By using this strategy, patient-specific, high-resolution, and cost-efficient medial phantoms can be manipulated directly, assisting and facilitating surgeries.[108] Two common bioprinting methods have been developed to fabricate vascular structures, namely direct and indirect bioprinting of perfused vasculature channels.[172] In the indirect bioprinting, sacrificial materials are printed inside a cell-laden supporting bioink and removed after printing, forming a perfused open lumen (**Figure 1.12a**).[81,96,97] In terms of the direct bioprinting of vessel structure, extrusion-based bioprinting has attracted much attention due to its advantages as mentioned in **Section 1.1**. Coaxial extrusion-based printing and embedded printing supported by a supporting bath are the two common direct printing strategies. The main idea of coaxial printing is demonstrated in **Figure 1.12b**. Cell-encapsulated bioinks in the shell region and sacrificial biomaterials in the core region are coaxially printed to form a vessel model, on which a confluent monolayer of cells can form no matter the vessel size.[162] This method can also be combined with a rotated rod template to fabricate hierarchical architectures as shown in **Figure 1.12c**.[172,173] However, the limitation of coaxial printing strategy is to fabricate branched vessels.[162] Hence, the strategy of using a supporting bath for embedded bioprinting has arisen to solve the issue as discussed in **Section 1.1.1**.

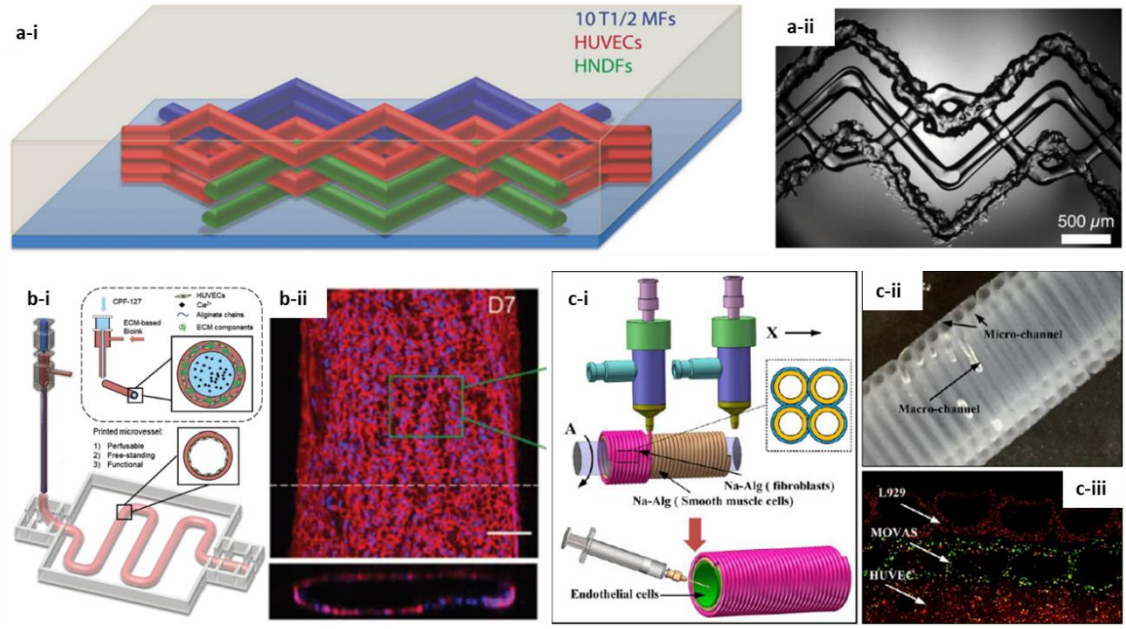

Figure 0.12 Bioprinting perfused vasculature channels. (a. i) Schematic illustration of a heterogeneous engineered tissue construct embedded in pure GelMA matrix by indirect bioprinting and the red filaments were evacuated to create open channels. (a. ii) Bright field microscopy image of the 3D printed tissue construct. (b. i) A schematic of coaxial bioprinted vessels using HUVECs-encapsulated hydrogel. (b. ii) HUVECs growth in the bioprinted vessel after 7 days fabrication. (c. i) Schematics of the coaxial bioprinting of cell-laden bioinks over a rod. (c. ii) A overview of a double-layer alginate vessel-like structure. (c. iii) Bioprinted vessel-like structure encapsulated with three cell lines. Reproduced from Ref. 97, 160, and 172.

The research of vasculature via 3D printing is mainly focused on the fabrication of microvasculature for perfusion tests instead of generating vessels that mimic the natural mechanical properties. In this project, we aimed to fabricate vessel models that can be used as a disease model to investigate the effect of vessel morphology on blood flow, clogging and other conditions. To mimic the real vessels, the vascular phantoms should simulate the mechanical properties, permeability, and

blood compatibility of the vasculature. The permeability of the artificial vessel should allow the exchange of essential nutrients, metabolic waste of cells, and prevent immunogenic molecules.[174] Blood compatibility (i.e. the endurance of blood to foreign materials) is crucial in artificial vessels. Additionally, modification of the vessels, such as surface passivation, construction of an antithrombotic bioactive surface, and surface endothelialization, is preferred to avoid thrombosis on the vessels. PEG and PVA are two commonly used hydrophilic materials to construct passive surface, and heparin is a representative molecule utilized to create a bioactive surface.[174] Since the endothelial layer are naturally anti-thrombogenic and hemocompatible, the formation of a single layer of endothelial cells would prevent thrombus formation.[175] In order to be applicable to ultrasound imaging, the electromagnetic and acoustic properties are also important in selecting suitable materials. Acoustic characteristics include density, sound speed, attenuation coefficient, and acoustic impedence.[176,177] Flow velocity and Reynolds number (Re) also need to be considered in the replication of biological flow. In human body, the peak flow velocity is 0.5-1 cm/s and 0.2-1.7 mm/s in arteriole and capillary vessels, respectively. The peak Re number is 0.09 and 0.001 for arteriole and capillary vessels, respectively.[176]

Water-based scanning gels, gelatin, agarose, magnesium silicate, oil gel, open cell foam, polyacrylamide gel, polyurethane, PVA, and silicon polymer-based materials are common materials used as tissue substitutes.[170] Among the materials, agarose, gelatin, PEG, and PVA-based polymers are widely used for vessel phantoms via 3D printing strategy and some are discussed in detail in **Section 1.2**.[176,178–181] Moreover, particles, such as cellulose, graphite, and aluminum oxide, can also be incorporated into polymers to provide attenuation and acoustic speckle on B-mode images and

improve the printability of the inks as well.[171]

1.4 Motivation and Scope of the Thesis

As discussed in the aforementioned introduction, it is essential to develop engineered 3D tissue and organ models with adjustable biochemical and physical properties for applications in replacement grafts, drug screening, and regenerative medicine. As such, the 3D bioprinting technique has arisen as a potential approach to create artificial tissue and organs by precisely depositing biomaterials and cells in patterned morphology. Micro-scale tissue constructs have been successfully bioprinted but with limited functionalities. The major hurdles of the functional large-scale tissues are the development of suitable biocompatible ink materials, the recapitulation of complex tissue, the selection of cell sources, and the scalability and manufacturing time of the 3D printing. Since the ink materials influence the printability, shape fidelity, spatial resolution, and the long-term cell functions, such as cell viability, proliferation, and growth, exploring suitable printable biocompatible materials are of paramount importance in the 3D bioprinting field. It will pave the development of fabricating large-scale tissue with physiologically properties. The shear-thinning behavior is the essential property for free-form printing as it enables smooth ink extrusion with minimal cell damage and rapid solidification post-printing due to the high viscosity at low shear rates. In addition, printing large scale tissues or organs is challenging in terms of cell viability and shape fidelity. Critical working parameters of the 3D printer, such as the needle size, printing speed, pneumatic pressure, and layer height, need to be systematically investigated to find the optimal printing window. Furthermore, embedded printing is a newly-developed potential approach to improve the quality and fidelity of the printed

large-scale constructs but the supporting bath materials still need to be improved.

Based on these motivations, this thesis features a comprehensive study of various printable biomaterials from nano-, micro-, to macro-scale with an ultimate goal of printing functional tissue-mimetic constructs. Severe liver disorders caused by drugs, toxins, or viruses have been a great threat to human life, and the established treatments are still not completely promising. Producing an artificial liver is a potential treatment but with challenge. Currently, micro-scale liver-mimetic tissue constructs have been fabricated to assemble with bioreactors for cancer research, drug screening, and clinical translation. However, few were working on fabricating liver lobule-mimetic constructs with cells deposited in defined regions, therefore, we aimed to print bicellular liver lobule-mimetic structures to investigate the versatility of our developed alginate-GelMA-CNC bioink material. We also investigated PVA-based biomaterials by printing artery-mimetic vessel, as vasculature is of great importance in fabricating tissue and organs. In addition, most studies on vasculature are for perfusion test but mechanical properties of the vessels were not included, thus we worked on printing standalone vessels that mimic the human vascular properties to fabricate disease model and investigate the effect of vessel morphology and mechanical property on blood flow.

This thesis is organized into five chapters. **Chapter 1** provides a general introduction on the 3D bioprinting techniques and the requirements of biomaterials that are utilized in bioprinting for tissue engineering. An overview of the research on 3D bioprinting that has been conducted in the past few years and the main challenges are also given. The main objective of the thesis is to develop suitable bioink materials for 3D printing tissue-mimetic constructs with proper functionality. The chapter is partly adapted from “Y. Wu, 3D Printing of Soft Hydrogels Incorporating Functional Nanomaterials,

Chem 794, Copyright © 2015, Yun Wu".

Chapter 2 introduces the research experimental methods and characterization techniques that are employed in this thesis. The chapter is partly adapted from "Y. Wu, 3D Printing of Soft Hydrogels Incorporating Functional Nanomaterials, Chem 794, Copyright © 2015, Yun Wu".

Aiming at exploring the printability and biocompatibility of our novel bioinks, in **Chapter 3,** I present a new shear-thinning bioink which employs alginate, CNC, and GelMA for direct printing cell-encapsulated and acellular architectures. Our results demonstrated the great potential of the bioink materials for printing complex constructs with multiple cell types and varying ECMs. This chapter is adapted from the following publications:

[1] Wu, Y., Lin, Z. Y. W., Wenger, A. C., Tam, K. C., & Tang, X. S., 3D bioprinting of liver-mimetic construct with alginate/cellulose nanocrystal hybrid bioink. *Bioprinting*, **2018**, 9, 1-6; Copyright © 2018, Elsevier B.V.

[2] Wu, Y., Wenger, A., Golzar, H., & Tang, X. S., 3D bioprinting of bicellular liver lobule-mimetic structures via microextrusion of cellulose nanocrystal-incorporated shear-thinning bioink. *Scientific reports*, **2020**, *10*, 1-12; Copyright © 2020.

In light of the limited research of 3D printing walled vessels and the need of vascular phantoms used for the investigation of cardiovascular disease, **Chapter 4** describes PVA-based biomaterials. Several properties, such as swelling, mechanical, and hemodynamic properties, were characterized. Embedded printing was employed to print large-scale constructs with great spatial resolutions and pattern fidelity. It has been found the ink compositions are suitable for fabricating vascular phantoms for both fundamental biomedical research, such as ultrasound imaging, and the translational tissue

engineering.

In the last chapter (**Chapter 5**), I conclude the results drawn from this research and provide recommendations for future research on the 3D bioprinting.

Chapter 2 Materials Preparation and Characterization Techniques

2.1 Polymer Preparation

Although natural (gelatin) and synthetic (PVA) polymers are chemically reactive with crosslinking agents, such as genipin and borax,[182,183] the photo-responsive polymers are preferred in 3D bioprinting. In this thesis, methacrylic anhydride (MAA) and glycidyl methacrylate (GMA) act as a modifier to introduce vinyl groups in gelatin and PVA, separately. The polymer methacrylation incorporate carbon-carbon π-bonds from the modifier onto the backbond of gelatin and PVA, enabling to gelate via radical crosslinking polymerizations. The physical properties of the methacrylated hydrogels can be readily adjusted by varying DOS, UV exposure time, and polymer and photoinitiator concentrations.

2.1.1 Synthesis of Gelatin Methacryloyl

MAA reacts with amine groups in gelatin via an addition mechanism involving acyl substitution and elimination of the leaving group. An additional proton transfer is also involved (**Figure 2.1**). The amine attacks a carbonyl group in MAA and forms a tetrahedral intermediate and the second carbonyl becomes part of the leaving group. The tetrahedral intermediate then collapses, recreating the carbonyl C=O bond, and ejects the leaving group.

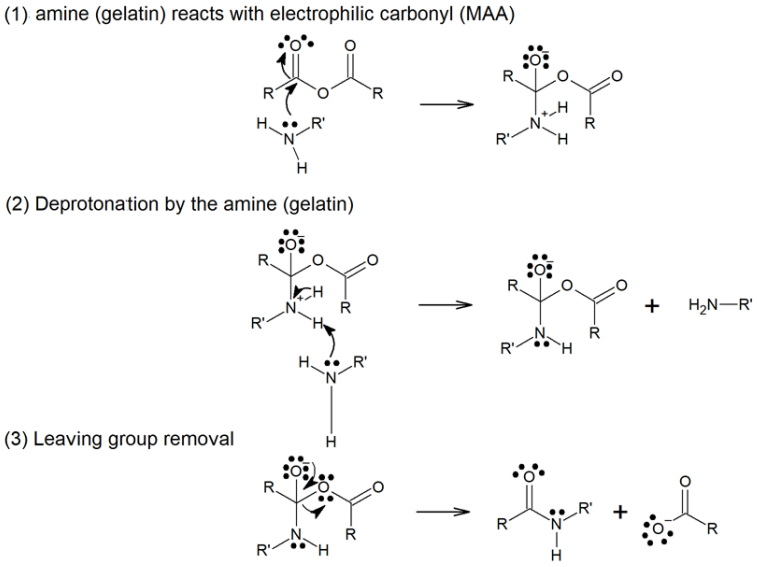

Figure 2.1 Mechanism of the reaction between amine and anhydride.

In this thesis, 0.25 M carbonate-bicarbonate (CB) buffer at a pH of 9 was used to maintain the pH of the reaction solution above the isoelectric point of type A gelatin (typically 8-9) at which the free amino groups of lysine are neutral, allowing them to react with MAA. It was reported that the degree of substitution of GelMA produced in CB buffer can be as high as 97% when MAA/gelatin molar ratio is lower than 2.2, which is much lower than the ratio of the conventional method.[184]

2.1.2 Synthesis of PVAGMA

The presence of hydroxyl groups in PVA allow the chemical modification of GMA via transesterification and epoxide ring-opening under basic conditions, and the ring-opening reaction is the preferred pathway.[104] Dimethyl sulfoxide (DMSO) and 4-(N,N-dimethylamino)pyridine (DMAP) act as a solvent and a catalyst in the reaction, respectively. The mechanism of the epoxide ring-opening is that the reactive RO- attacks the epoxide at the least substituted carbon in an S_N2 mechanism followed by a proton transfer as shown in **Figure 2.2**. The transesterification reaction occurs with the addition of base catalyst that deprotonates PVA, forming an alkoxide anion. It attacks the carbonyl of

GMA, forming a tetrahedral intermediate. The C=O bond is broken and the negative charge is transferred to the carbonyl oxygen. The OR' group of GMA is removed from the intermediate as a leaving group, resulting in the transesterified product (RCOOR") as illustrated in **Figure 2.3**.

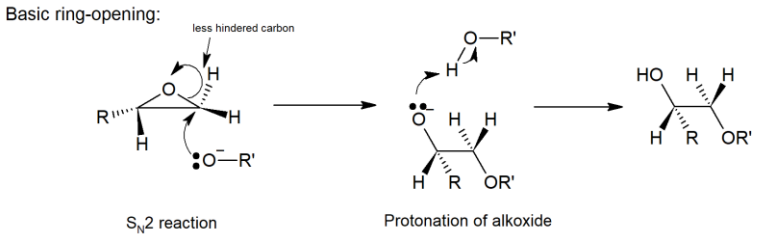

Figure 2.2 Mechanism of ring-opening reaction under basic condition.

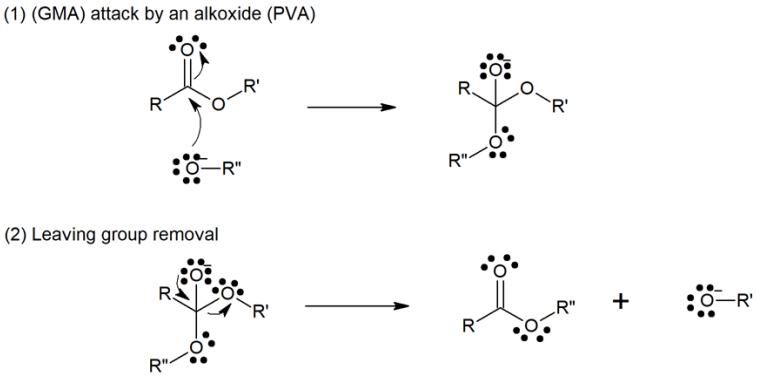

Figure 2.3 Mechanism of transesterification under basic condition.

2.1.3 Free Radical Polymerization

Free radical polymerization is one of the most versatile polymerization methods for obtaining vinyl polymers, by which a polymer is formed from the successive addition of free radical building blocks. Three kinds of reactions are involved: initiation, propagation, and termination, and the process is illustrated in **Figure 2.4**. A free radical R* is produced by the photoinitiator with the exposure to UV light and added to the vinyl polymers by opening the π-bond to form a new radical center. The propagation comprises the successive additions of repeat units to the previous molecule. The polymer growth is terminated by a coupling reaction between two radicals.[185]

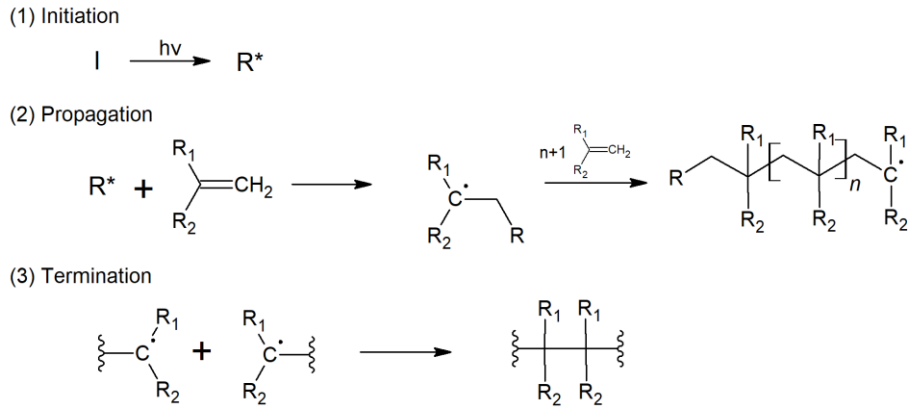

Figure 2.4 Mechanism of free radical polymerization.

Currently, the most commonly used UV photoinitiator is 1-[4-(2-hydroxyethoxy)-phenyl]-2-hydroxy-2-methyl-1-propanone (Irgacure 2959), but with significant limits. The water solubility of Irgacure 2959 is reported to be lower than 2 wt% and the molar extinction coefficient at 365 nm is lower than 4 M^{-1} cm^{-1} and trails off entirely before 370 nm (**Figure 2.5a**), thus limiting the polymerization kinetics.[186] However, the newly developed lithium phenyl-2,4,6-trimethylbenzoylphosphinate (LAP) with optimal properties, such as high water solubility (up to 8.5 wt%), cytocompatibility, and improved polymerization kinetics, enables lower initiator concentrations and wider absorbance wavelength light compared to Irgacure 2959 (**Figure 2.5b**),[186] thus LAP was used as the photoinitiator in this thesis.

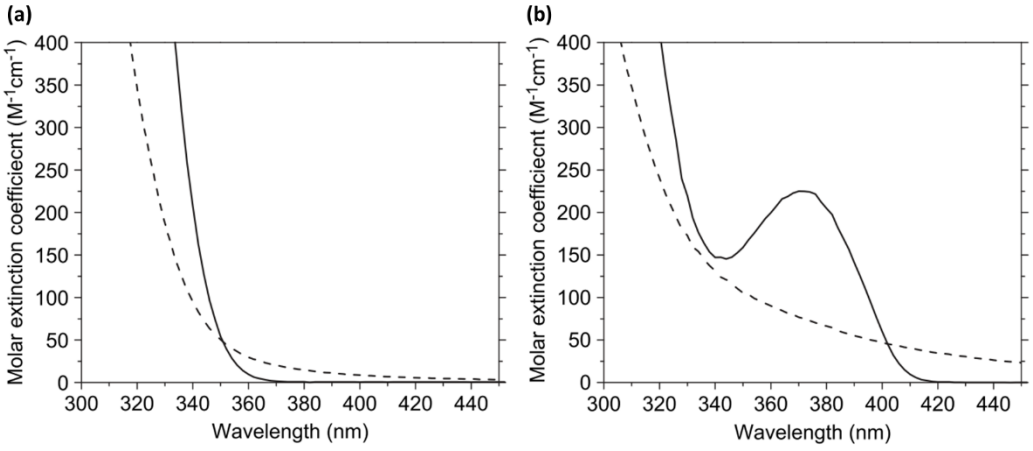

Figure 2.5 Molar absorptivities of (a) Irgacure 2959 and (b) LAP (solid line) and their corresponding cleavage products (dashed line). Reproduced from Ref. 184.

2.2 Nuclear Magnetic Resonance (NMR)

Nuclear magnetic resonance (NMR) spectroscopy (Bruker 300 MHz) was utilized to confirm the obtained compounds and the degree of substitution. NMR works on the principle that all nuclei that are electrically charged and have spin will orient to magnetic field. When the magnetic field is applied, an energy transfer happens at a wavelength that corresponds to radio frequencies. When the magnetic field is removed, the spin return to its base level (lower energy state) and emits at the same frequency. The proximity to electronegative atoms and unsaturated groups shield the proton causing the NMR chemical shift. The chemical shift in the frequency can be detected by a radio wave detector and Fourier-transformed to produce the spectra of NMR absorption versus frequency.[187]

In the sample preparation steps, good-quality NMR tubes must be fully cleaned and dried prior to using. Because the magnetic field homogeneity is crucial to the NMR experiment, the depth to which sample tubes are filled is critical. Tubes must be neither under- nor overfilled. The sample must be soluble in a solvent (D_2O in this project) which must have no resonance in the region of the analyte (GelMA and PVAGMA). The integration of the signal peak is proportional to the number of nuclei creating that peak, thus providing an approach to determining methacrylation efficiency.

2.3 Rheology

A viscometer (Bohlin-CS Rheometer) is an instrument that measures the viscosity and flow

parameters of a fluid. Rheology is an important characterization about the pre-gel solutions behavior. Based on the viscosity of the materials, different test modes could be used due to different sensitivities. For instance, for materials with a low viscosity comparable to water, a cup and bob mode is used. CP 4-40 mode is usually used for materials with high viscosity.

Fluids can be categorized into two main groups, Newtonian and non-Newtonian, as illustrated in **Figure 2.6**. The viscosity of Newtonian fluids is independent on the shear rate, while non-Newtonian fluids do not obey Newton's law of viscosity. The non-Newtonian fluid can be Bingham, shear-thinning, or shear-thickening based on their behavior under shear strain. Bingham plastics, such as toothpaste and clay suspension, has a linear relationship between shear stress and shear rate but needs a yield stress to induce the flow. Shear-thinning occurs when the viscosities decrease with the increased shear rates, which is preferred in designing bioinks for 3D printing, as lower shear stress is required to extrude bioinks. Once the bioinks are extruded, the shear rate decreases and the viscosity increases, therefore the bioinks are capable to hold their structure without spreading and collapsing. The opposite fluid is shear-thickening fluid, such as corn starch in water. The viscosity increases with the increase of shear rate, which is not ideal for the bioinks.

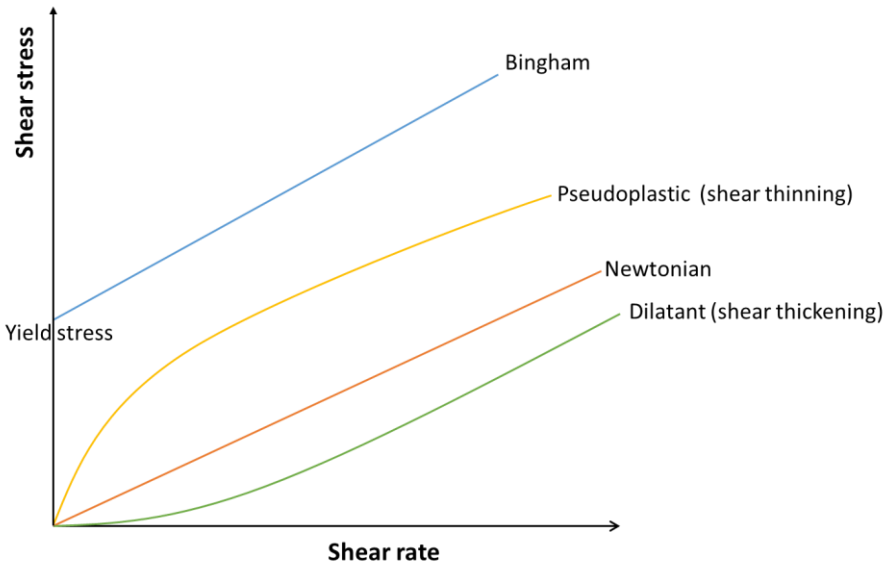

Figure 2.6 Shear stress vs. shear rate of different fluids.

The viscosity of a material can be significantly affected by variables such as shear rate, temperature, pressure, and the time of shearing. The viscosity of Newtonian materials does not depend on shear rate, as opposed to non-Newtonian liquids which do. The viscosity-versus-shear rate curves of the shear-thinning fluids show that at very low shear rates, the viscosity is constant, while at high shear rates, the viscosity is constant again, but at a lower level. In the shear-thinning region, there is a relationship between shear rate and viscosity as shown below:

$$\eta = K\gamma^{n-1} \qquad \textbf{Equation 2-1}$$

This is the well-known "power-law" model and *n* is termed as the power-law index. *K* is the consistency. η is the viscosity, and γ is the shear rate. The equation shows that the slope of the shear-thinning region is equal to *n-1* if the x-axis and y-axis are in the logarithmic form.

There are other important parameters in rheology such as the complex shear modulus *G**, the storage/elastic modulus *G'* and the loss/viscous modulus *G''*. The storage modulus shows the elastic response of the material whereas the loss modulus expresses the liquid-like behavior. These

parameters can be obtained through an oscillatory test. *G** is defined through the following equation:

$$\sigma(t) = G^{*}\gamma(t) \qquad \textbf{Equation 2-2}$$

where σ is the shear stress varied with time, and *G'* and *G''* are obtained from *G** from this equation:

$$G^{*} = G' + iG'' \qquad \textbf{Equation 2-3}$$

If $G' < G''$, the material indicates liquid behavior.

When a non-Newtonian liquid flows through a straight circular tube with a radius of *r* at a volumetric flow rate *Q*, the shear rate at the wall is modified to

$$\gamma_w = \frac{4Q}{\pi r^3}\left(\frac{3}{4} + \frac{1}{4}\frac{d\,ln\,Q}{d\,ln\,\sigma_w}\right) \qquad \textbf{Equation 2-4}$$

For shear-thinning liquids in the region following "power-law", $\frac{d\,ln\,Q}{d\,ln\,\sigma_w}$ is greater than 1 and equal to $1/n$. So the shear rate at the wall can be simplified to

$$\gamma_w = \frac{4Q}{\pi r^3}\left(\frac{3}{4} + \frac{1}{4n}\right) \qquad \textbf{Equation 2-5}$$

2.4 Mechanical Property Measurements

Once the bioinks are crosslinked into gels, the mechanical properties of the gels need to be tested to ensure that the bioinks have comparable mechanical strength to that of the mimetic tissues. Two main types of mechanical strengths, including compression and tensile strength, were evaluated with a Universal Macro-Tribometer (UNMT-2MT, T1377 by Centre for Tribology, Inc.). Tensile tests measured the stress applied to stretch the dog-bone shape samples while compression tests measured the force applied to compress a cylinder-like sample. In both cases, the load to yield a given deformation is monitored as the specimen is deformed at a constant rate, generating a load-versus-compressibility/tensibility profile. The resulting stress-versus-strain curve is given where the stress, σ,

is defined as

$$\sigma = \frac{P}{A_0} \qquad \textbf{Equation 2-6}$$

where *P* (in Pa) is the load on the sample with an original cross-sectional area A_0. The strain, ε, is defined as

$$\varepsilon = \frac{|l - l_0|}{l_0} \qquad \textbf{Equation 2-7}$$

where *l* is the gage length at a given load, and l_0 is the original length.

Elastic modulus, *E*, is determined by the slope of the stress-strain curve in the elastic region. The linearity of the stress-strain plot in the elastic region is a graphical statement of Hooke's law:

$$\sigma = E\varepsilon \qquad \textbf{Equation 2-8}$$

Herein the modulus, E, represents the stiffness of a material.

2.5 Microscopy

2.5.1 Optical Microscopy

Microscopy with low magnification objective lenses is a useful tool for characterizing the dimensions of the printed constructs, such as the diameter of the printed filament and the inner diameter and wall thickness of the printed hollow tubing. Based on the measure dimensions of the printed filament, printing parameters, such as pneumatic pressure, can further be optimized.

Optical microscopy (Zeiss) was also used to observe the cell morphology and growth during cell culturing. The cell viability can be obtained when the cells are stained with trypan blue and counted in a hemocytometer under an optical microcope. Trypan blue is taken up by dead cells due to the broken cell membrane while the viable cells with intact membrane do not take up trypan blue, thus

dead and live cells can be distinguished. By counting the cells in the four corner quadrants using a hemocytometer under optical microscope, cell number can be obtained by the following equation:

$$cell\ \# = \frac{total\ cell\ \#\ in\ the\ four\ corner\ quadrants}{4} \times cell\ suspension\ dilution\ ratio \times 10^4 \times$$

$$total\ cell\ suspension\ volume \qquad \textbf{Equation 2-9}$$

The cell viability can then be determined by:

$$cell\ viability\ (\%) = \frac{live\ cell\ \#}{total\ cell\ \#} \times 100\% \qquad \textbf{Equation 2-10}$$

2.5.2 Fluorescent Microscopy/Confocal Fluorescent Microscopy

To determine the cytotoxicity and cells growth in the bioinks, and the effect of the printing process on cells, fluorescence microscope (Nikon) and confocal fluorescence microscope (Zeiss) was used to observe the cell behavior in the biological experiments. Different fluorescent dyes were used to stain and differentiate different chemical compounds. The cell nuclear was stained with 4',6-diamidino-2-phenylindole (DAPI). It exhibits about a 20-fold enhancement in fluorescence when binding to dsDNA. F-actin, the most abundant proteins in cells, can be visualized by binding it to fluorophore-conjugated phalloidin. It helps demonstrate the structure and morphology of cells. The cell viability can be investigated by using a live/dead assay kit composed of calcein AM and ethidium homodimer-1 (EthD-1). Nonfluorescent cell-permeant calcein AM is converted to the green and fluorescent calcein by intracellular esterase activities with an excitation wavelength at 495 nm and emission wavelength at 515 nm. EthD-1 enters cells with damaged cell membranes and reacts with nucleic acids, thus producing red fluorescent signal that is excited at 495 nm and emitted at 635 nm. In order to distinguish hepG2 and fibroblast, Qtracker 655 with Excitation/Emission (Ex/Em 405-615/655 nm) was utilized to stain the hepG2 cell line due to its long-lasting, targeted signal and

minimal impact on live cells. After culturing for certain time period, the encapsulated cell in the bioinks were stained by calcein, therefore live fibroblast showed green signals while live hepG2 cells had green and dark red signals.

2.6 Ultrasound Imaging

Diagnostic ultrasound is an imaging method that uses high frequency sound wave of over 20 kHz to produce images of human body. It can penetrate several centimeters through the medium or the tissue, but the intensity of the sound wave decreases exponentially as a function of depth, known as attenuation. A change in the material acoustic impedance, usually caused by local density and compressibility, will cause the reflection and scattering of the sound wave, thus images displaying the distance and the intensities of the echoes are generated.[167] Gels are applied on the surface of samples to prevent air pockets from blocking the sound waves when creating images.

CHAPTER 3 3D Bioprinting of Bicellular Liver Lobule-Mimetic Structure via Microextrusion of Cellulose Nanocrystal-Incorporated Shear-Thinning Bioink

3.1 Introduction

Bioprinting, a subset of 3D printing, holds promise for depositing biomaterials and cells precisely to create heterogeneous tissue-mimetic constructs that promote cell-cell and cell-extracellular matrix (ECM) interactions in a 3D environment which are absent in two-dimensional (2D) cell culture systems.[10–12] Among the different bioprinting techniques such as extrusion-based, light-induced, and inkjet-based methods,[13–15] the microextrusion-based (ME) 3D bioprinting technique has attracted much attention due to its ease of use and the potential to accommodate a wide range of bioink viscosity, offer high cell loading density, and take use of multiple polymerization methods.[25–28] As mentioned in **Chapter 1**, although there has been a rapid rise in ME bioprinting research, bioink materials and methods remain limited. Ideal bioinks must meet the requirements for printability, in addition to fulfilling the essential properties required for tissue engineering, such as biodegradability, biocompatibility, cell attachments, and comparable mechanical strength to human tissues.[46–48] Shear-thinning is considered as one of the most important bioink properties for ME since it determines the ultimate printability (e.g. resolution, pattern fidelity) by preventing clogging and reducing shear stress that can lead to cell damages.[25,28] Furthermore, to obtain constructs with a high resolution and a high aspect ratio, the printed scaffold should be mechanically strong enough to avoid

collapsing. Instant gelation after deposition or partially pre-gelled hydrogels are also preferred to ensure high structural integrity.[9,54]

In this chapter, we designed ink formulations from nano- (CNCs) to micro-/macro-scale (alginate and gelatin network). By devising multi-scale inks, their micro-scale (e.g. molecular interactions, porous structures, cell behavior) and macro-scale behaviors (e.g. elastic properties, swelling, rheology, etc.) were optimized. We first prepared a hybrid bioink by blending alginate and CNCs, which combines the desirable properties and overcomes the inherent disadvantages of the individual components and investigated its rheological and mechanical properties. It has been shown that the incorporation of nanoparticles and nanofibers into biopolymers, such as CNCs into alginate, can induce favorable shear-thinning behavior.[64] An optimized bioink formulation was then selected to print a liver-mimetic 3D honeycomb construct, which was cultured with fibroblasts in the honeycomb structure and hepatoma cells in the middle cavities. It demonstrated that viability of cells encapsulated in this bioink was unaffected during printing. However, CNCs/alginate hydrogel cannot provide a suitable microenvironment for cell proliferation. In particular, it lacks cell attachment sites. Thus, an auxiliary material must be incorporated into the CNCs/alginate to increase its bioactivity. A new version of a hybrid bioink (ACG) composed of alginate, CNCs, and gelatin methacryloyl (GelMA) were then developed. Naturally-derived proteins, such as gelatin, collagen, and fibrinogen, are common materials that have been utilized in tissue engineering to promote cell growth.[55–57] Among these materials, gelatin has the advantages of low cost and high purity.[79] However, gelatin tends to liquefy at high temperatures (~ 37 ℃), dramatically hindering its application for bioink development. Hence, GelMA derived from gelatin with methacrylamide and methacrylate groups has been used to

ensure easy solidification of the printed constructs via UV crosslinking.[84] Moreover, the physical properties of crosslinked GelMA hydrogel can be easily tuned by tailoring the degree of substitution. It has been found that hydrogels made of low concentrations of GelMA with a low degree of modification can improve the cell viability and facilitate cellular organization.[85,86] Here, we designed two types of bioinks, namely the ACG hybrid ink and a low concentration GelMA ink. To evaluate the printability of our bioinks and their efficacy in mimicking the native cellular microenvironment, liver-lobule mimicking structure was chosen as a model. Liver-lobules have well defined geometry that can be printed to scale. In-vitro liver tissue models are in great demand for disease modeling, drug discovery, and clinical applications.[136,138] Recently, multiple literatures have demonstrated the fabrication of liver tissues using various methods and materials, including biofabricating liver lobule-mimetic constructs via dynamic optical projection stereolithography and a piece of liver tissue via ME bioprinting.[149,152,153] Taken together, our results showed that, through bioink material design, ME bioprinting techniques have enormous potential for creating 3D heterogeneous and physiologically-relevant tissue constructs.

3.2 Materials and Methods

3.2.1 Materials

Sodium carbonate, sodium bicarbonate, gelatin (type A, 300 g Bloom, from porcine skin), deuterium oxide (D_2O), methacrylic anhydride (MAA), calcium carbonate, D-(+)-gluconic acid δ-lacton, and lithium phenyl-2, 4, 6,-trimethylbenzoyphosphinate (LAP) were purchased from Sigma Aldrich. Xanthan gum was purchased from CP Kelco. Pharmaceutical grade sodium alginate (PROTANAL LF

10/60 FT) with 60–70% guluronate (G) residues was acquired from FMC (Philadelphia, PA). Dulbecco's Modified Eagle's Medium (DMEM), Eagle's Minimum Essential Medium (EMEM), fetal bovine serum (FBS), trypan blue stain (0.4%), and OmniPur 10X phosphate buffered saline (PBS) concentrate were purchased from VWR. Polydimethylsiloxane (PDMS) was purchased from Dow Corning. Penicillin/streptomycin, TrypLE Express, LIVE/DEAD viability/cytotoxicity kit, trypsin/EDTA solution, DAPI, Alexa Fluor 488 conjugated-phalloidin, and Qtracker 655 cell labeling kit were purchased from Thermo Fisher. Human albumin ELISA kit was purchased from Abcam. Cellulose nanocrystals were donated by Professor Michael K.C. Tam from the Department of Chemical Engineering at the University of Waterloo.

3.2.2 Synthesis of Gelatin Methacryloyl (GelMA)

GelMA was synthesized with the method developed by Shirahama *et al.*[184] In brief, gelatin solution (10%) was obtained by dissolving gelatin power in 0.25 M carbonate-bicarbonate (CB) buffer and adjusted to pH 9.0 in round bottom flask at 50 °C. MAA (0.1 mL MAA/1 g gelatin) was added dropwise. After three hours of reaction, the reaction mixture was centrifuged at 3250 g for 10 min and adjusted to pH 7.4. The solution was diluted with double the volume of DI water and dialyzed with a 12 kDa molecular-weight-cutoff (MWCO) membrane against DI water at 50°C for one week, followed by flash frozen in liquid N_2 and lyophilized. The GelMA product was stored in the dark at −20 °C. Nuclear magnetic resonance (NMR) spectroscopy was utilized to confirm the obtained compounds and the degree of methacrylation. The lyophilized GelMA was dissolved in D_2O at 50 mg/mL and analyzed via proton nuclear magnetic resonance spectroscopy (^{1}H NMR).

3.2.3 Bioink Preparation

CNC powder was dispersed in Milli-Q water to prepare 8 wt% CNC suspensions and alginate powder was dissolved in Milli-Q water to prepare 4 wt% alginate solutions. To prepare the alginate/CNC hybrid pre-gel solutions (20/40), equal volumes of CNC and alginate solutions were mixed. The pre-gel solution was sterilized by autoclaving at 121℃ for 20 min for cell culture.

The second version hybrid bioinks were prepared as following: CNC powder was suspended in Milli-Q water at a concentration of 6 wt% and sonicated for 10 min at 37 kHz. Alginate (2 wt%) was then added to the mixture and vortexed for 5 min followed by centrifugation at 2000 g for 3 min. The resulting mixture was then vortexed and centrifuged again, followed by 10 min of sonication at 37 kHz. GelMA (10%) was dissolved in 2X PBS containing 0.2 wt% LAP. For the rheological measurements, the two different solutions were mixed at the same volume to reach a final concentration solution of 1 wt% alginate, 3 wt% CNC, and 5 wt% GelMA containing 0.1 wt% LAP, referred to as 135ACG, vortexed for 5 min, and centrifuged for 3 min twice. GelMA (4 wt%) was prepared by dissolving GelMA in 1× PBS containing 0.1 wt% LAP.

To make cell-laden bioink, the initial concentrations of all polymer solutions were prepared at 1.25 times the concentrations shown above. The GelMA solution was sterilized through a 0.22 μm filter. The alginate and CNC mixture was autoclaved at 121℃ for 20 min. Cell-laden GelMA (4%) solutions were obtained by mixing GelMA with cells via pipetting. Cell-laden 135ACG bioink was prepared by mixing the hydrogel and concentrated cell suspensions with a double-syringe mixer at a volume ratio of 4:1. The produced 135ACG bioink had a NIH/3T3 fibroblast cell density of 5 million per milliliter. The mixing procedure had no significant influence on the cell viability (data not shown).

3.2.4 Rheological Properties

The rheological measurements were conducted using a Bohlin-CS Rheometer with a cone-plate geometry (CP 4-40). ACG hybrid bioinks were refrigerated for 10 min before measurements at room temperature. The steady-state shear viscosities were measured with a shear rate in the range of 0.1 – 1000 s^{-1}. A strain-sweep test with a strain from 0.05% to 10% and a frequency at 1 Hz was performed to determine the linear viscoelastic regions. The optimal strain was chosen to be 0.1% for the oscillation frequency test from 0.1 to 10 Hz. Step-shear measurements were performed at 0.012 s^{-1} and 100 s^{-1}.

3.2.5 Preparation of Supporting Medium for Embedded Printing

The support bath medium for printing was prepared according to the procedure developed by Noor *et al*.[38] Briefly, sodium alginate (0.32 wt%), xanthan gum (0.25 wt%), and calcium carbonate (9.56×10^{-3} M) were dissolved in DI water and homogenized. Concentrated D-(+)-gluconic acid δ-lactone solution was added to the mixture to reach a final concentration of 19.15 mM and stirred constantly until the viscosity of the mixture increased and no precipitation of the calcium carbonate was observed. The mixture was then left at room temperature for 24 h. DI water was added to the mixture (4:1 volume ratio), homogenized, centrifuged at 11000 g for 20 min. The precipitated pellet was collected. 1 wt% xanthan gum was freshly prepared and added to the pellet at a volume ratio of 1:1. A homogeneous support bath was obtained through vigorous vortexing.

3.2.6 3D printer and Printing Procedure

A FlashForge Creator Pro (FlashForge, China) mounted with a custom-made syringe holder was used (**Appendix A**). The syringe was connected to an Ultimus V high precision dispenser (Nordson

EFD, USA). 3D models were designed using SolidWorks. For the print of the first version bioink 20/40, the outer honeycomb structures were printed using one syringe with fibroblast-containing bioinks (10^6 cells/mL) and the inner cavities were then printed using another syringe with bionk containing human hepatoma cells (10^6 cells/mL). The printed constructs were gelated in 1 wt% $CaCl_2$ solution for 10 min and then washed with serum-free DMEM. Next, the constructs were cultured in complete DMEM supplemented with 5 mM $CaCl_2$ in an incubator. Molded constructs were made as control samples using an extrusion-free method. Briefly, 20/40 bioink containing fibroblasts or hepatoma cells was placed on a sterilized glass slide with two spacers (150 μm thickness) and covered with an ion permeable membrane to make a slab (26 mm x 26 mm x 0.15 mm), which was then immersed in 1 wt% $CaCl_2$ for 10 min and was cultured in the same condition as that of the honeycomb constructs.

For the second version bioink ACG printing, bioinks were loaded into 10 mL pneumatic syringes and refrigerated for 10 min before printing to increase viscosity, taking advantage of the temperature-responsive GelMA. Structures were printed on cover glasses directly or in the support bath with a 32-gauge needle at a printing speed of 20 mm/s and under an air pressure of 20 psi. After printing, the structures were then crosslinked under UV light (365 nm) for 2 min. The embedded 3D-printed constructs were washed with DI water to remove excess support bath materials.

3.2.7 Cell Culture and Characterization

Human hepatoma cells were culture in EMEM with 10% FBS and 100 unit/mL penicillin, 100 μg/mL streptomycin. Fibroblasts (NIH/3T3) and liver hepatocellular carcinoma (hepG2) cells were cultured in DMEM supplemented with 10% FBS and 1% penicillin/streptomycin and maintained in a 5% CO_2 incubator at 37°C. For fluorescence imaging, with a Zeiss LSM 700 confocal microscope (Carl

Zeiss AG, Germany), cells were stained using DAPI, Phalloidin, LIVE/DEAD viability/cytotoxicity kit or Q-tracker following manufacturer's instructions. The images were analyzed using ImageJ. Cell area distribution and total cell spreading areas were extracted from 6 replicates (n = 6) and are presented as mean ± standard deviation. Differences between samples were determined from the independent *t*-test and were considered statistically significant when $p < 0.05$. To evaluate HepG2 cell proliferation and viability inside a hydrogel matrix, cells were extracted by dissolving the matrix using TrypLE Express and then counted using a hemocytometer.

3.2.8 Mechanical Properties

Cylindrical PDMS molds with a diameter of 6 mm and a height of approximately 2 mm were made. The acellular and cell-laden bioinks were added into the molds and crosslinked prior to uniaxial compression tests. The initial 10% strain region of a strain-stress curve was chosen to determine the compressive modulus of each sample. To gauge degradation over time, samples were cultured under standard cell culture conditions (see below) for 2 weeks. Compressive modulus of each sample was measured immediately after fabrication, on day 7, and on day 14.

3.2.9 Measurement of Albumin Production

Cell-laden scaffolds were cultured in 6-well plates, with 1.2 mL phenol-red free DMEM per well. Cell medium was collected from each well on days 1, 4, 7, and 14 and stored in liquid nitrogen. The cell medium was changed every other day and 24 hours before being collected for albumin production test. A Human albumin ELISA kit was used to measure albumin concentrations according to manufacturer's instructions.

3.3 Results and Discussion

3.3.1 Characterizations of 20/40 Bioinks

The CNC used was produced by Celluforce Inc. with lengths of 200–400 nm and diameters of 10–20 nm as shown in **Figure 3.1a**. The CNC was derived from sulfuric acid hydrolysis with abundant negatively charged sulfate groups on the surface with the zeta potential of -40 mV at pH 7.0 (**Figure C.2a**). Additionally, the dynamic light scattering data illustrates that the average size of CNCs was approximately 20 nm (**Figure C.2b**).

The bioink 20/40 displayed excellent shear-thinning property with a power-law index *n* of 0.23, extrudability, and shape fidelity after deposition. In addition, the incorporation of CNC in the alginate network resulted in a highly porous microstructure with more uniform pores being about 20 μm in size (Data were not shown in this PhD thesis as they were presented in the master thesis.). A 3D liver-mimetic honeycomb structure was designed as shown in **Figure 3.1b**. **Figure 3.1c** exhibits an image of the 3D structure immediately after bioprinting. Food dyes were used to differentiate the fibroblasts-laden bioink (green) from the human hepatoma cells-laden bioink (purple). The viabilities of naked (before mixing with bioink) fibroblasts and hepatoma cells were 96.47% and 92.75%, respectively. On day 0, the cell viabilities of the molded constructs were 70.73% for fibroblasts and 55.07% for hepatoma cells, which could be attributed to mechanical stress during mixing and possibly the cytotoxicity of $CaCl_2$. The cell viabilities of fibroblasts and hepatoma cells in bioprinted constructs on day 0 were 71.00% and 67.06%, respectively. No significant differences in cell viability were observed between molded and bioprinted constructs, indicating that the bioprinting process resulted in no observable cell death and thus is cell-compatible. However, after 3 days, cell viabilities of

fibroblasts and hepatoma cells decreased to 58.91% and 49.51%, respectively (**Figure 3.1d**). **Figure 3.1 e-f** show the fluorescence images of homogeneously distributed fibroblasts and human hepatoma cells in the bioprinted constructs. The declining viability and non-obvious cell growth over time may arise from the lack of cell-binding sites in the hydrogel, which limit cell adhesion, viability and proliferation.

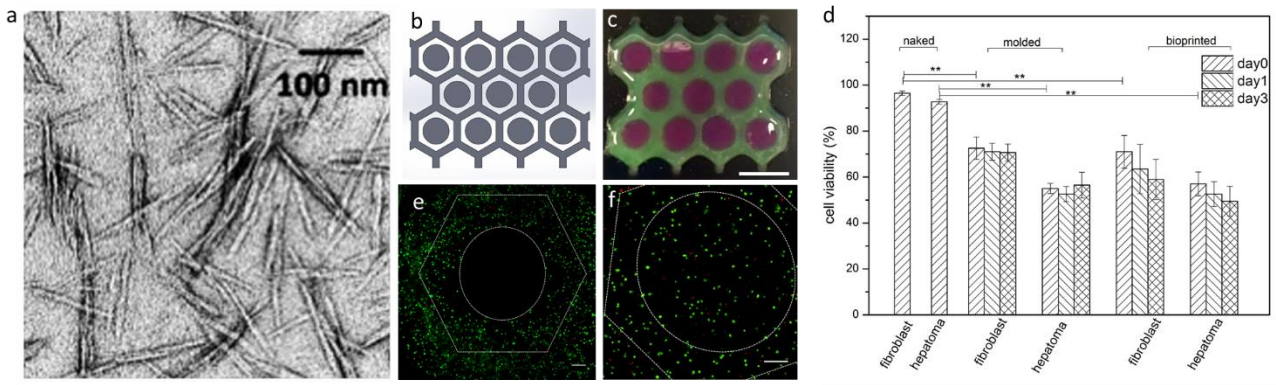

Figure 3.1 Characterization of CNCs and cell viability studies of bioink 20/40. (a) TEM image of CNCs used in this study. (b) Schematic top-down view of the liver-mimetic engineered tissue constructs. (c) 3D printed constructs with bioink 20/40. Food dyes were used to distinguish fibroblast-laden bioink (green) from hepatoma cell-laden bioink (purple). (d) Statistical analysis of viabilities (live cells populations/total cell populations) of fibroblast and human hepatoma cells on days 0, 1, and 3. Representative live/dead fluorescent images of bioprinted (e) fibroblast only and (f) fibroblast plus human hepatoma cells. The dashed lines are the boundaries of the designed structure. The cells were stained with Calcein-AM and ethidium homodimer-1 to show live (green) and dead (red) cells. Scale bars are 5 mm in (c) and 250 μm in (e) and (f).

To circumvent such issues, one potential solution is incorporating polymers containing cell-binding sites, such as gelatin, into the system. There is an ever-growing amount of evidence reported

in research literature that gelatin is effective in promoting the cell attachment due to its RGD tripeptide sequences, which are the major integrin-binding domains present within extracellular matrix (ECM). We found that the incorporation of gelatin in the alginate-CNCs hybrid bioink did not influence the viscosity significantly and hence printability of the bioink as shown in **Figure 3.2**. The viscosity of gelatin was approximately an order lower than that of the alginate/CNC mixture (data not shown), and therefore it may not change the viscosity of the hybrid ink significantly. Additionally, the hybrid bioink was prepared by mixing alginate in the CNC suspension followed by adding gelatin solution dissolved at elevated temperature (60℃). The rheology was measured once the ink was prepared and gelatin was not gelled under shearing, thus it did not change the viscosity of the hybrid alginate/CNC/gelatin bioink dramatically.

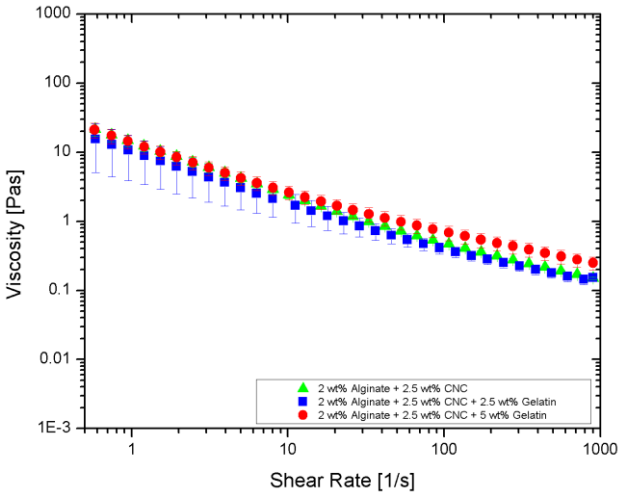

Figure 3.2 Flow curves of 2 wt% alginate and 2.5 wt% CNCs with different concentrations of gelatin.

3.3.2 Biofabrication of Liver Lobule-Mimetic Constructs

GelMA derived from gelatin with methacrylamide and methacrylate groups instead of gelatin was selected as one of the bioink components because GelMA can be easily gelled under UV light,

while gelatin tends to liquefy at high temperatures (~ 37 ℃). Herein, we fabricated liver tissue-mimetic constructs according to the process illustrated in **Figure 3.3**. To mimic an array of liver lobules to-scale, a honeycomb lattice was first printed with a bioink composed of 1% alginate, 3% CNC, and 5% GelMA (135ACG). The honeycomb lattice has a 0.48 mm wall thickness, 0.4 mm wall height, and 2.4 mm spacing. Then the inner cavities of the hexagon units were filled with 4% GelMA. Four different variations were 3D printed in this work, referred to as S1 (honeycomb: fibroblasts-laden 135ACG, middle cavities: acellular GelMA); S2 (honeycomb: acellular 135ACG, middle cavities: hepG2-laden GelMA); S3 (honeycomb: acellular 135ACG, middle cavities: fibroblasts/hepG2-laden GelMA); and S4 (honeycomb: NIH/3T3-laden 135ACG, middle cavities: hepG2-laden GelMA). The printed constructs were cultured in phenol-free cell culture media for 2 weeks. Cell viability, proliferation, and morphology in the constructs were studied using confocal fluorescence microscopy on days 1, 4, 7, 11, and 14. Cell culturing media were collected on days 1, 4, 7, and 14 to study the cellular activities through albumin production. The four variations allowed us to compare single-cell 3D structures (S1, S2) with heterogeneous bicellular structures (S3, S4). Furthermore, S3 and S4 were designed to enable direct-contact (S3) and non-contact (S4) interactions between hepG2 cells and the supporting cells NIH/3T3.

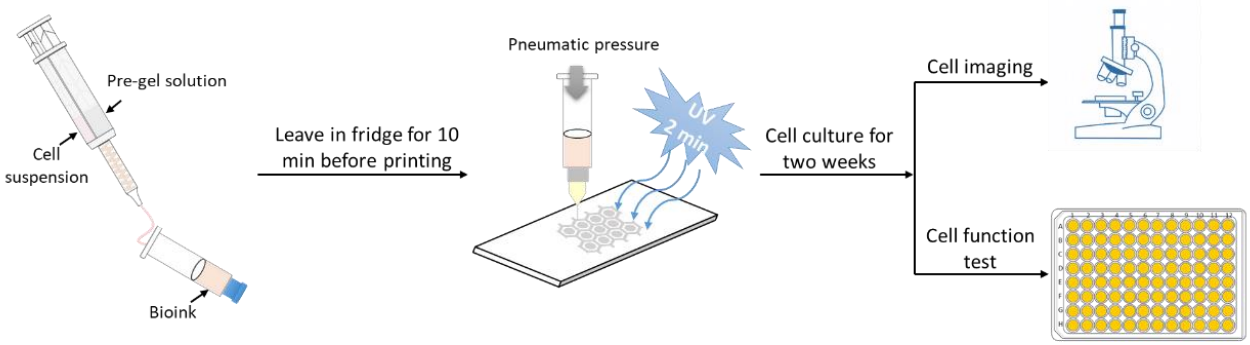

Figure 3.3 Schematic illustration of the biofabrication process.

3.3.3 GelMA Characterization

To enable high-resolution bioprinting, advanced bioink formulations and cross-linking mechanisms were developed. GelMA was synthesized by converting lysine groups contained in gelatin to methacryloyl groups to allow UV crosslinking. The synthesis of gelatin methacryloyl (GelMA) and the degree of substitution (DOS) was confirmed through ^{1}H NMR spectroscopy. As seen in **Figure 3.4**, there are four distinctive peaks at δ2.8 ppm, 5.5 ppm, 1.9 ppm, and 7.2 ppm, which can be attributed to methylene protons of unreacted lysine groups (i), acrylic protons of methacrylamide grafts on lysine groups (ii) and hydroxyl lysine groups (iii), methyl protons of methacrylamide grafts (iv), and aromatic groups (v), respectively. The decreased signal in peak (i) was observed in the spectrum of GelMA, indicating the successful conversion of lysine to methacryloyl functional groups. The degree of substitution was calculated from the ratio of the integrals of the unreacted lysine groups in GelMA and the lysine groups in gelatin after normalization to the aromatic peaks. The DOS of the GelMA used in this study is 85.33%, which is in agreement with the reported data by Shirahama *et al*.[51]

$$\mathrm{DOS} = 1 - \frac{I_{GelMA}}{I_{Gelatin}} = 1 - \frac{0.1092}{0.7443} = 85.33\%$$

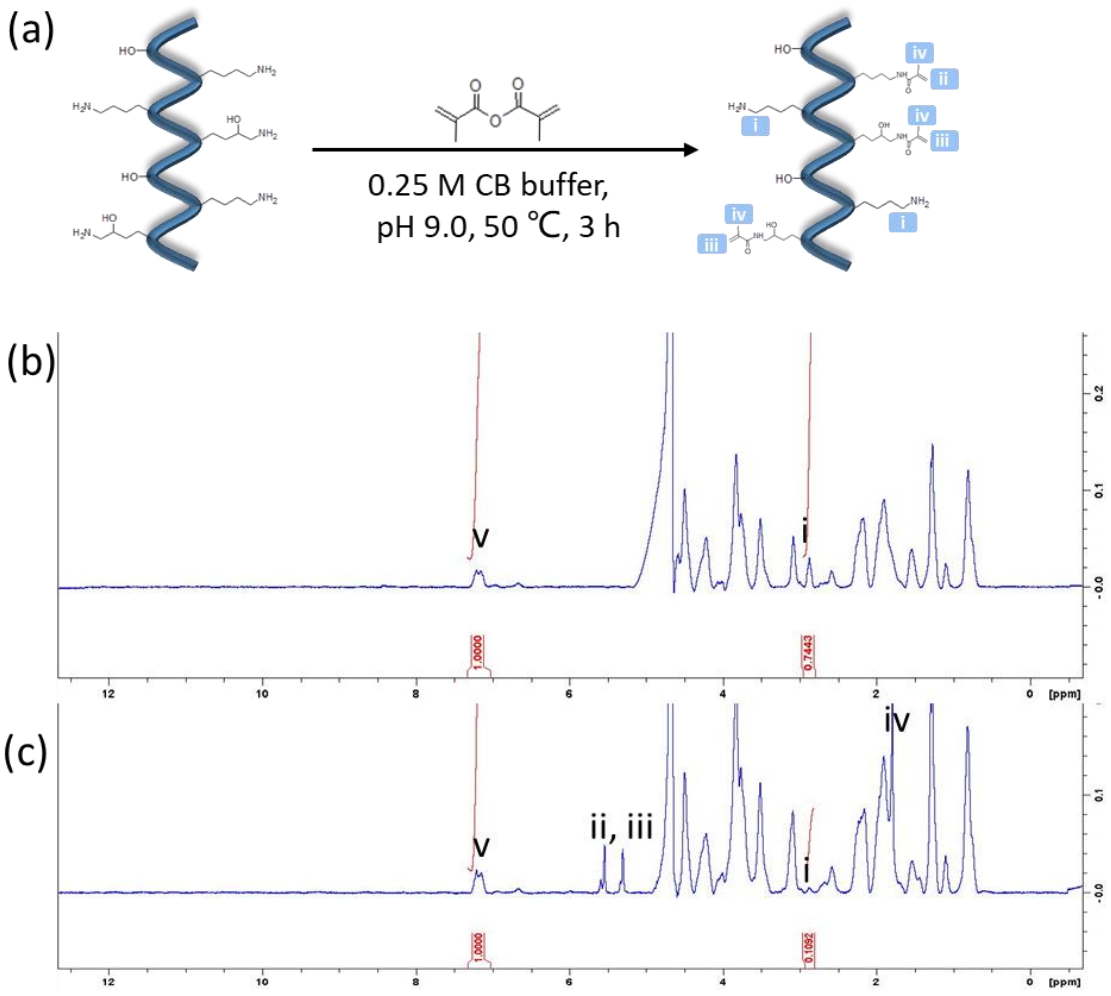

Figure 3.4 (a) Schematic illustration of GelMA synthesis process. ^{1}H NMR spectra of (b) gelatin and (c) GelMA

3.3.4 Bioink Formulation and Properties

The rheological properties of 4% GelMA and a hybrid bioink 135ACG were tested. Step-shear measurements illustrated the injectability and self-healing behavior of the 135ACG bioink after being applied high shear which is essential when the bioink is extruded through a high-gauge needle (**Figure 3.5**). As shown in **Figure 3.6a**, the viscosity of 4% GelMA is around 0.1 Pa·s and it shows a slight shear-thinning property. The GelMA coils can disentangle and orientate in the flow direction with increasing shear rate, leading to the observed shear-thinning behavior after a critical shear rate is reached. The

incorporation of CNCs and alginate into the GelMA solution significantly altered the intermolecular interactions, leading to drastically different rheological properties. The hybrid bioink, 135ACG, exhibited a strong shear-thinning property over the entire shear rate range of 0.1 to 1 000 s^{-1} with a curve slope of -0.85. The 135ACG ink showed a viscosity close to 200 Pa·s at static state and 0.2 Pa·s at the shear rate of 1000 s^{-1} (i.e. 3 orders lower). The repulsive interaction between the both negatively charged alginate and CNCs surface makes the ink homogenous without any aggregation. At static state, alginate molecules wrap around the surface of the CNCs mainly through H-bonding. When a shear stress is applied, the entangled polymers re-align and lowers the bioink's viscosity. Compared with hybrid bioinks reported previously by our group and other groups,[64,192–194] the new 135ACG bioink showed a much stronger shear thinning behavior and one order of magnitude higher viscosity at static state, indicating its superiority for ME printing. Further, as shown in **Figure 3.6b**, the viscous modulus G" was higher than the elastic modulus G' in 4% GelMA at low frequencies, while G' overrode G" at around 8 Hz, indicating that pure GelMA was more liquid-like at low frequencies and not suitable for ME bioprinting since the modulus of 4% GelMA was lower than 10 Pa. On the other hand, for 135ACG, G' were higher than G" over the entire frequency range, suggesting that 135ACG is more solid-like and can produce scaffolds with good structural fidelity.[64]

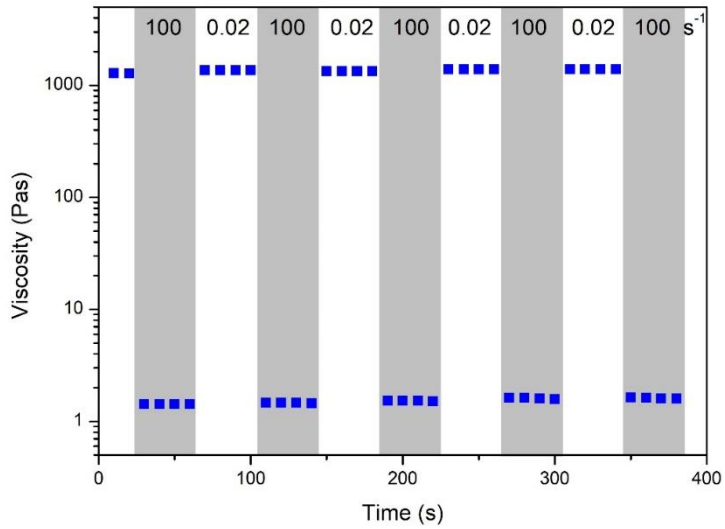

Figure 3.5 Step-shear measurements of 135ACG at high and low shear rate to illustrate the injectability and recovery behavior.

Besides printability, bioinks must offer scaffolds with suitable mechanical strength and degradation profile for tissue engineering. After printing, cell-laden and acellular constructs were crosslinked chemically (by UV), then cultured over two weeks. Their compressive moduli were measured on days 0, 7, 14. The compressive modulus of 4% GelMA was 4 269 ± 278 Pa immediately after preparation (day 0). Upon cell addition, the overall compressive modulus reduced to 3 175 ± 217 Pa (hepG2 cells only) and 2 624 ± 370 (hepG2/fibroblast cell mixture), respectively (**Figure 3.6c**). The Young's modulus of rat hepatoma cell line is 1.25 kPa,[195] which is much lower than the stiffness of GelMA matrix, therefore the incorporation of softer cells significantly decreases the compressive modulus of the hydrogel. Neither acellular nor cell-laden GelMA constructs exhibited significant decrease in overall mechanical strength over the two-week period (**Figure 3.6c**, day 7 & 14). According to literature research, the suggested reason for this is that the enzymatic degradation of GelMA and the generation of natural extracellular matrix by embedded cells were balanced.[196] Future

experiments to confirm such speculation can be adding collagenase inhibitor to the cell culturing media and measuring ECM protein production and gene expression in the crosslinked hydrogels over time. Furthermore, our data confirmed that the GelMA scaffolds can provide a stable and soft environment ideal for the growth of hepG2 cells over the entire study period. Ma *et al.* reported that the stiffness of the scaffolds influenced the hepG2 cellular growth and functions such that hepG2 cells cultured in the scaffolds with a stiffness of 0.5 kPa and 5 kPa tend to aggregate and form spheroids.[152]

The compressive modulus of acellular 135ACG scaffolds was 11 222 ± 2 381 Pa on day 0 and the addition of fibroblast cells lowered the stiffness to 6 800 ± 664 Pa (**Figure 3.6d**). This is consistent with previous literature reports that, when the stiffness of the substrate at the fibroblasts attachment sites were over 5 kPa, the cells were observed to decrease overall scaffold stiffness.[197] On soft substrates (1-5 kPa) fibroblasts adjust their stiffness matched to the substrate without forming stress fibers. However, as the stiffness of the substrate increases to 5 kPa, fibroblast cells spread and organize the actin cytoskeleton into stress fibers, forming more organized filament bundles and crosslinked actin filaments, and reach the limit of cytoskeleton reinforcement.[197] Hence, the decreased compressive modulus induced by the incorporation of cells was likely caused by the softer cells encapsulated and the material voids.[198] Interestingly, the compressive moduli of both acellular and cellular 135ACG increased to 15 876 ± 2 324 Pa and 9 204 ± 1 480 on day 14, respectively. The increased compressive moduli can be attributed to the strengthening of alginate network by Ca^{2+} in the cell medium.

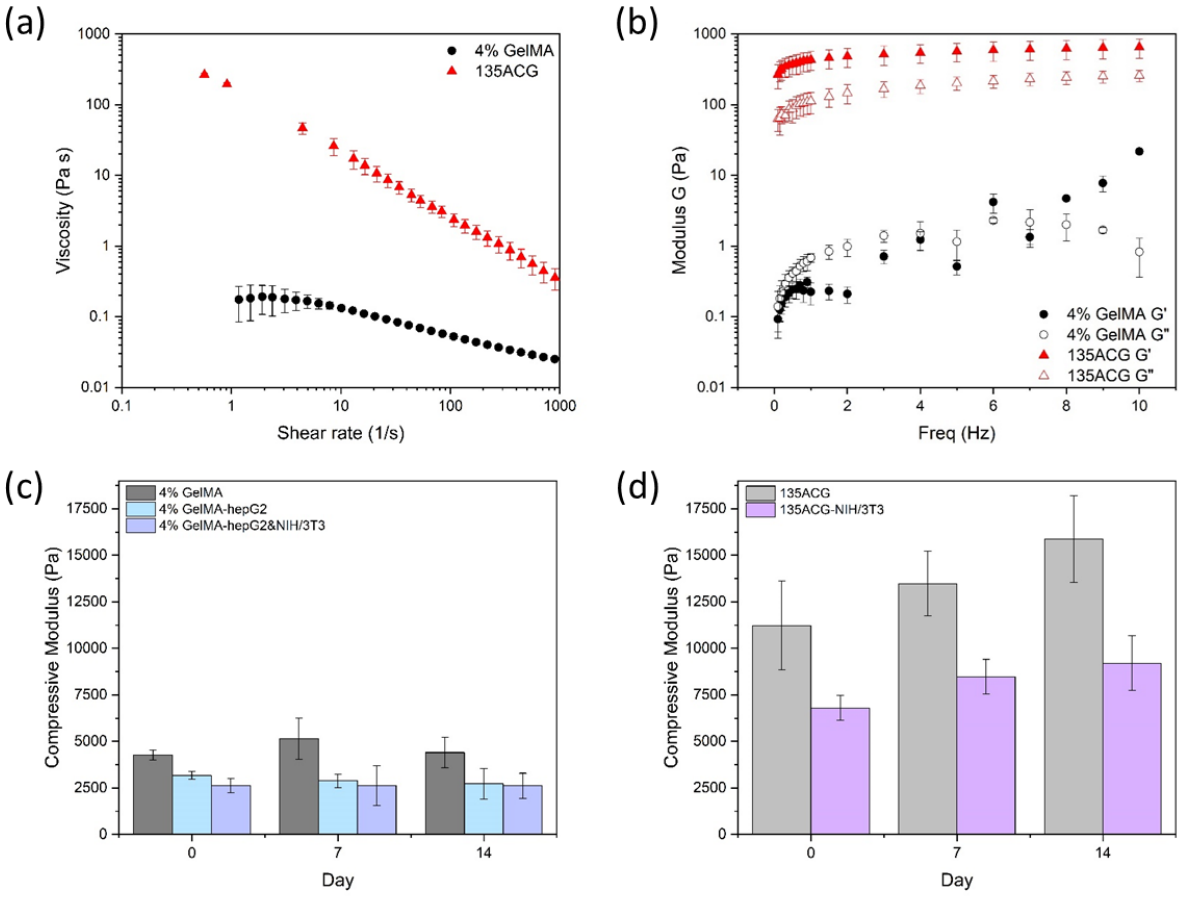

Figure 3.6 Characterization of the bioinks. (a) Flow curves of two different bioinks, 4% GelMA and 135ACG. (b) Elastic modulus (G') and viscous modulus (G'') of the two bioinks as function of oscillatory frequency. Compression modulus changes of (c) 4% GelMA and (d) 135ACG gels with/without cells over two weeks.

3.3.5 Printability of the Hybrid Bioink

Honeycomb architectures, with 0.48 mm wall thickness and 2.4 mm spacing, were printed using two printing methods (**Figure 3.7**), in order to evaluate the suitability of the hybrid ink 135ACG for printing 3D structures in terms of resolution, pattern fidelity, and geometrical aspect ratio. Free-form printing, that is to directly layer-by-layer ME printing on a cover glass, yielded structures with favorable fidelity up to a height of 1.8 mm (**Figure 3.7b**). Upon further addition of layers, spreading

and collapsing began to occur. Without in-situ crosslinking or support, ME printing using 135ACG bioink can yield honeycomb structures up to a height of 3.4 mm without completely filling up the inner cavities (**Figure 3.7c**). This is enabled by the excellent shear-thinning and solid-like properties of the hybrid bioink, which is not achievable using pure polymeric inks at much higher concentrations.

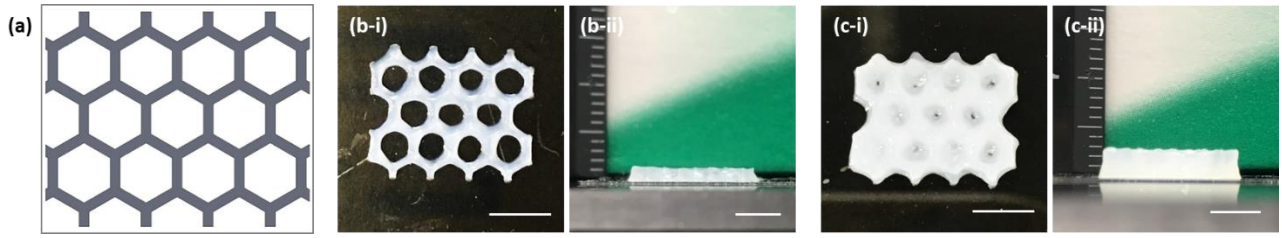

Figure 3.7 Printability of the hybrid bioink. (a) Schematic of the liver lobule-mimetic honeycomb structure. (b-I, c-i) Top and (b-ii, c-ii) side views of the free-form printed structures with a height of 1.8 mm and 3.4 mm, respectively. Scale bars: 5 mm.

An embedded printing strategy was also developed. Generally, the support bath for embedded printing must be stiff enough to hold the extruded filaments in place, rapidly self-heal, and possess a low yield stress to accommodate needle movement.[31,96] Thus, a Bingham plastic material is a good candidate to act as a rigid body at low shear rates and a viscous fluid at higher shear rates.[26,33] Previously, Noor *et al.* developed a transparent support medium composed of alginate microparticles in xanthan gum solution.[38] Based on their work, we further adjusted the composition to better fit our system and rheological properties of the modified support bath material were measured. It exhibited a shear-thinning behavior, and the viscosity was approximately 50 Pa·s at 0.1 s^{-1} (**Figure 3.8a**). The elastic modulus was larger than the viscous modulus over the entire frequency, and the elastic modulus was around 100 Pa (**Figure 3.8b**). In addition, the yielding stress of the mixture was approximately 10 Pa (**Figure 3.8 c-d**). **Figure 3.9a** illustrates the embedded printing process. As shown

in **Figure 3.9 b-c**, honeycomb structures with a height of 3.75 mm and 6.8 mm respectively were generated using embedded printing with better pattern fidelity than the 3.4 mm-tall structure generated by free-form printing (**Figure 3.9c**). With embedded printing, we demonstrated that the 135ACG formulation can be used to generate tall (up to 6.8 mm), high water content (> 90%), high porosity hydrogel structures (i.e. suitable ECM), due to the enhancement of hydrogel mechanical strength by CNC incorporation. Overall, these printing results exemplified the great potential of the unique CNC-incorporated 135ACG bioink for ME printing of cell-compatible structures with high aspect ratio.[34,199,200]

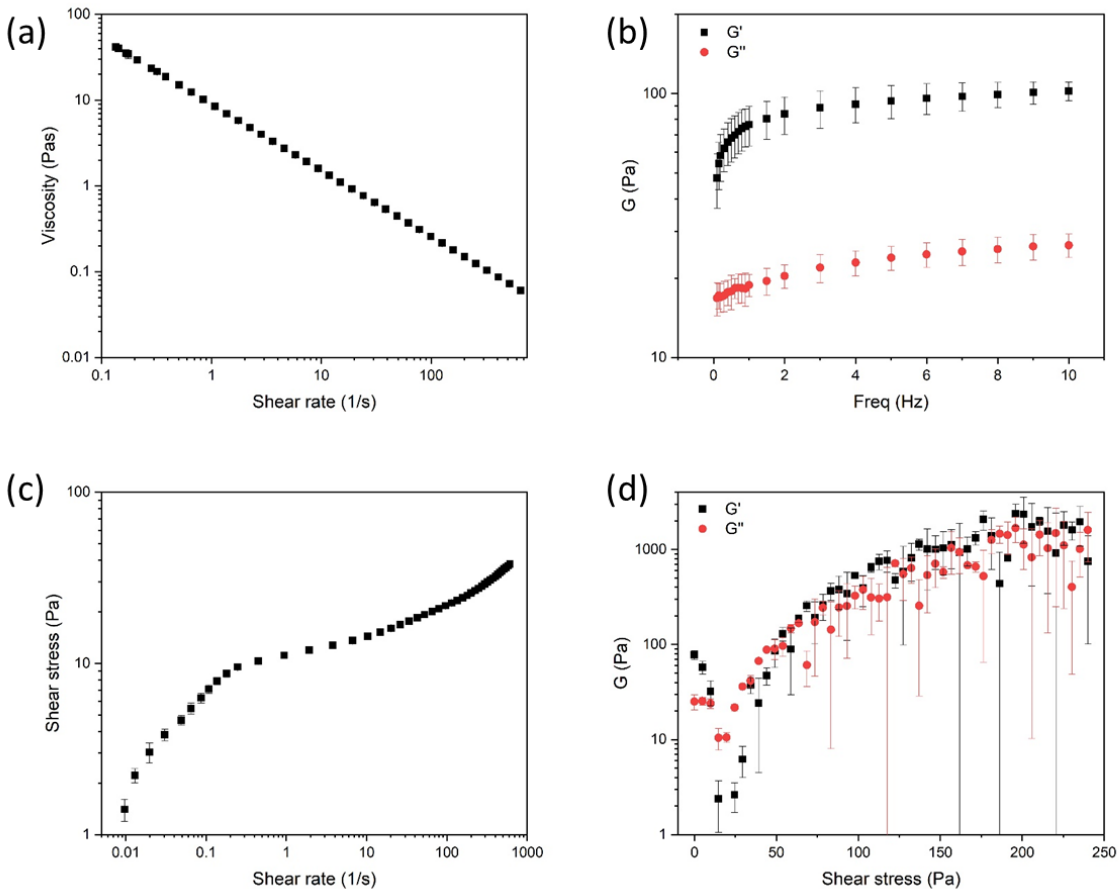

Figure 3.8 Rheological characterization of the supporting bath material. (a) Flow curves, (b) elastic modulus (G') and viscous modulus (G'') as a function of frequency, (c) yielding stress, and (d) elastic

modulus (G') and viscous modulus (G'') as a function of shear stress of the supporting bath material.

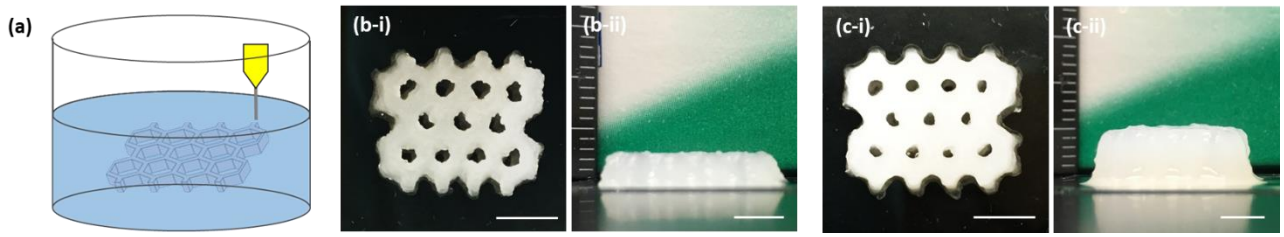

Figure 3.9 Printability of the hybrid bioink. (a) Schematic illustration of embedded printing of the honeycomb structure. (b-i, c-i) Top and (a-ii, b-ii) side views of the embedded printed structures with a height of 3.75 mm and 6.8 mm, respectively. Scale bars: 5 mm.

3.3.6 Cell Behavior in Bioprinted Mono-Cellular 3D Constructs

A mono-cellular construct with NIH/3T3 cells embedded in 135ACG (S1), as schematically illustrated in **Figure 3.10a**, was first printed. The inner cavities of the hexagon units were filled with acellular 4% GelMA. Cells proliferated over time (**Figure 3.10 b-c**), the elongation of NIH/3T3 being observed on day 7 (**Figure 3.10c**), confirming that the printing process did not reduce cell viability or influence cell morphology and the 135ACG gel is a suitable ECM for NIH/3T3. In comparison, fibroblasts were arrested in CNC/Alginate only (no GelMA) matrix (data not shown). Thus, GelMA provided cell adhesion sites and facilitated the proliferation of NIH/3T3 cells in the 135ACG scaffolds. In addition, cells were elongated and aligned along the boundary of the two different bioinks instead of migrating into the soft matrix. The phenomena can be explained by durotaxis, a mechanism of cell migration guided by the stiffness of the ECM (**Figure 3.10 d-g**). Fibroblast cells tend to migrate from softer toward stiffer substrates because a more stable focal adhesion and higher traction forces are formed in a stiffer region.[201] Therefore, when NIH/3T3 cells migrated in the stiffer 135ACG bioink, the protrusion of the cells' leading edge stopped at the interface of the two different bioinks due to

durotaxis and continued laterally along the boundary of the two hydrogels while the trailing edge retracted, leading to the observed orientation of the cells.[202,203]

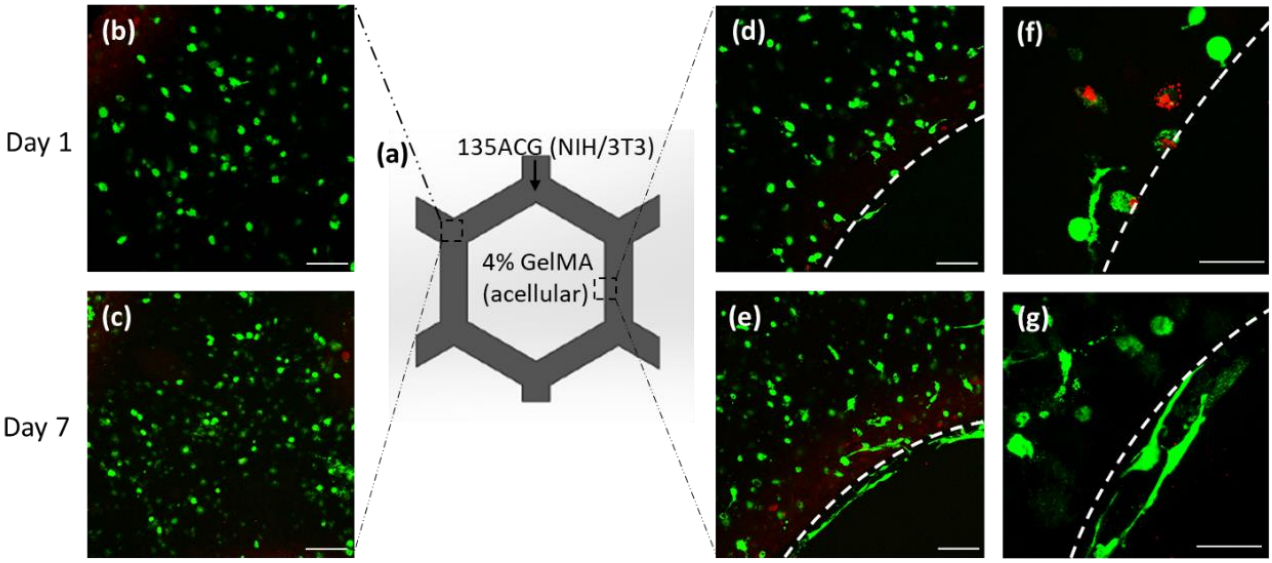

Figure 3.10 NIH/3T3 cell growth, proliferation and morphology in 135ACG. (a) Schematic of construct S1. Fluorescence images of NIH/3T3 on days 1 and 7 (green: live cells; red: dead cells) encapsulated in the middle of honeycomb wall (b & c), as well as at the boundary of 135ACG and GelMA (dashed line) (d & e). Zoomed-in images of NIH/3T3 at the boundary on (f) day 1 and (g) day 7. Scale bars are 100 µm in (b-e) and 50 µm in (f-g).

Furthermore, NIH/3T3 cells located near the bottom (cover glass) showed more elongated morphologies, while cells in the upper portion of the constructs exhibited rounder morphologies (**Figure 3.11**). The mechanical gradient between the soft hydrogel and the stiff substrate causes an edge effect, increasing the stress on the hydrogels near the bottom of the printed scaffolds. Cells sensed the stiffness of their environment and modulated their morphology accordingly.[201]

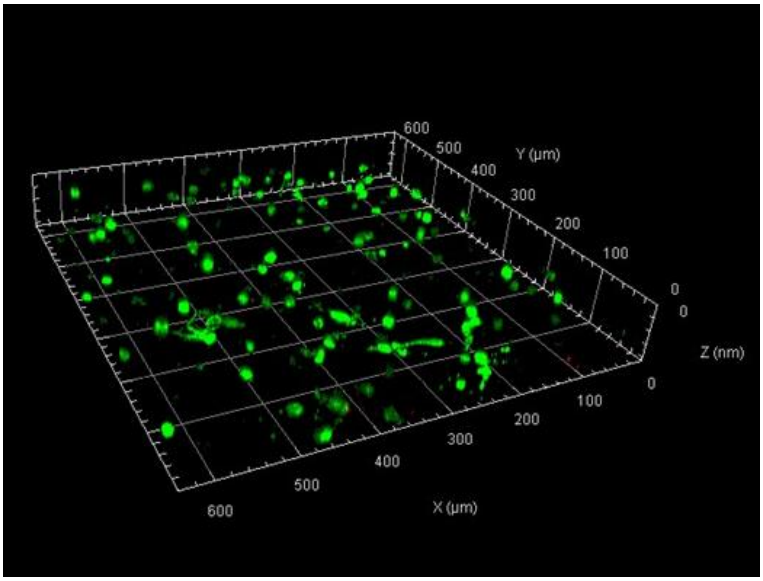

Figure 3.11 3D rendered confocal fluorescence image of NIH/3T3 cells embedded in 135ACG.

Cell proliferation and viabilities in 2D hepG2 and 3D (i.e. hepG2 embedded in GelMA) cultures were compared and illustrated in **Figure 3.12**. Our results showed that hepG2 cells in 2D cultures proliferated much faster than in 3D cultures, as shown in **Figure 3.12a**. Thus, the initial cell concentration in 2D cultures was chosen to be relatively low, at 50K cells/well in a 6-well plate, while in 3D cultures the initial cell density was 2.5M cells/mL. Cell viabilities in both 2D & 3D cultures were confirmed to be greater than 90% over the 14-day study period (**Figure 3.12b**). Additionally, hepG2 cells formed spheroids from day 1 in the 2D environments and the spheroids size increased significantly over the two weeks. A monolayer of hepG2 cells was formed in 2D. In comparison, hepG2 spheroids were much smaller and the proliferation rate was lower in 3D than that in 2D as shown in **Figure 3.12c**.

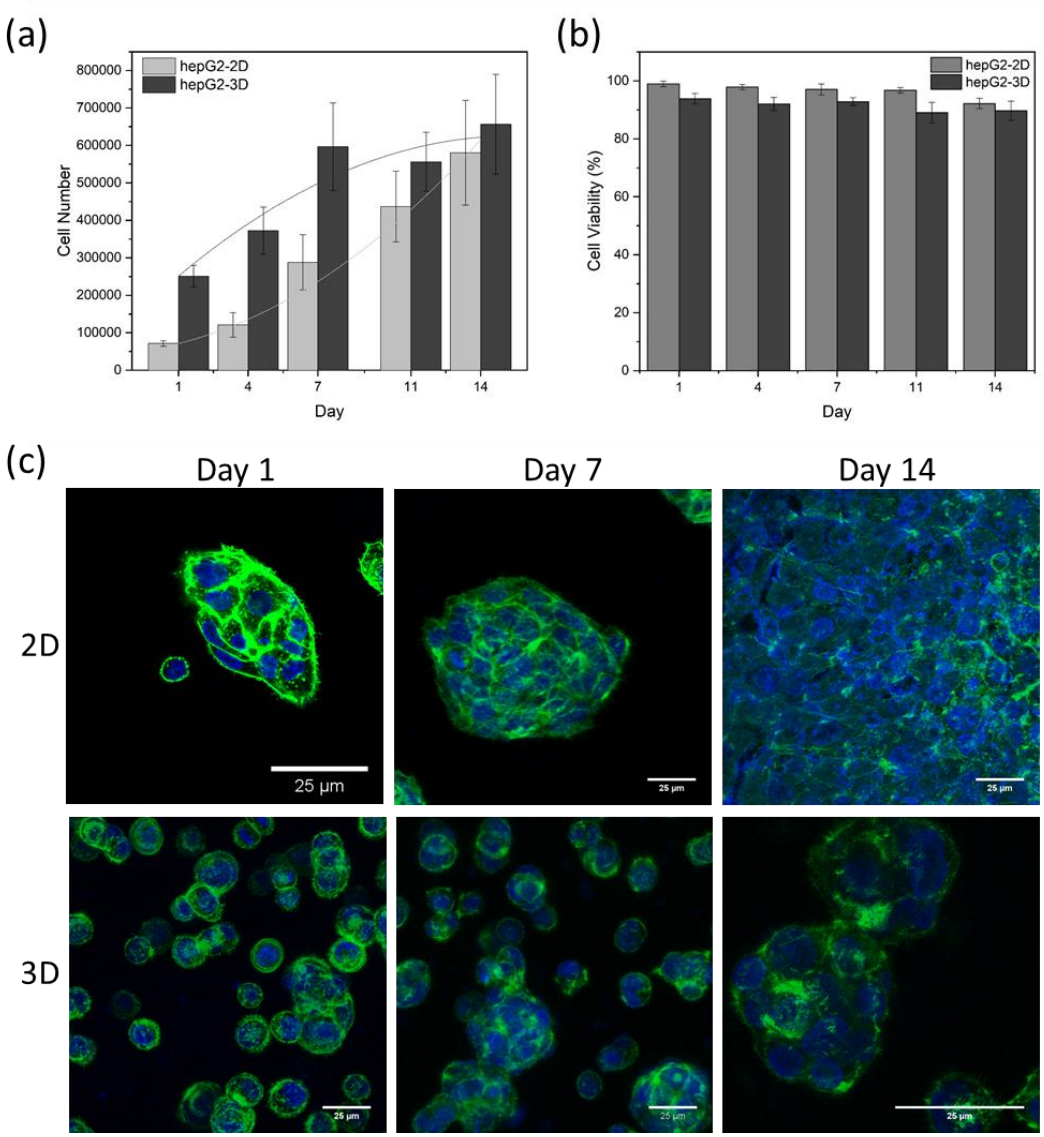

Figure 3.12 Cell studies on hepG2 cells in 2D and 3D environments. (a) Cell number and (b) cell viability in 2D and 3D hepG2 cultures over two weeks. (c) Fluorescence images of F-actin/DAPI stained hepG2 cells cultured in 2D and 3D for 14 days.

A second mono-cellular construct was then printed with acellular 135ACG ink first and the inner cavities were filled with HepG2 cell-laden GelMA (4%) (S2), as illustrated in **Figure 3.13a**. Furthermore, hepG2 cell morphology was studied using confocal fluorescence microscopy. HepG2 cells were observed to be mostly single or in small aggregates on day 1 (**Figure 3.13b**), form spheroids four days

post printing (**Figure 3.13c**), and the spheroids increased significantly in size over time (**Figure 3.13 c-d**). High cell viability was maintained until day 11 (**Figure 3.13d**). On days 11 & 14, dead cells were observed mainly in the centers of large spheroids (**Figure 3.13 d-e**), likely due to nutrient depletion and the accumulation of toxic products. A close examination of the boundary between the soft GelMA and the stiff 135ACG gels revealed that hepG2 propagated exclusively in the GelMA matrix (**Figure 3.13f**). Cell/cluster area distribution and the total cell spreading areas were extracted via statistical analysis of the fluorescence images and plotted in **Figure 3.13 g-h**. On day 1, most of the cell cluster areas were in the range of 100-300 μm^2, i.e the size of single cells and small cell aggregates. Cell/cluster sizes were shown to steadily increase in day 4 & 11 (**Figure 3.13g**), indicating that hepG2 cells formed larger cell clusters/spheroids over time in GelMA. However, the total cell spreading area plateaued on day 7 (**Figure 3.13h**), which is consistent with the growth curve shown in **Figure 3.12a**. Taken together, 4% GelMA hydrogel possessed a similar mechanical strength to the liver tissue and provided an optimal environment for the growth of hepG2 cells, which is consistent with the findings from Ma *et al.*[152]

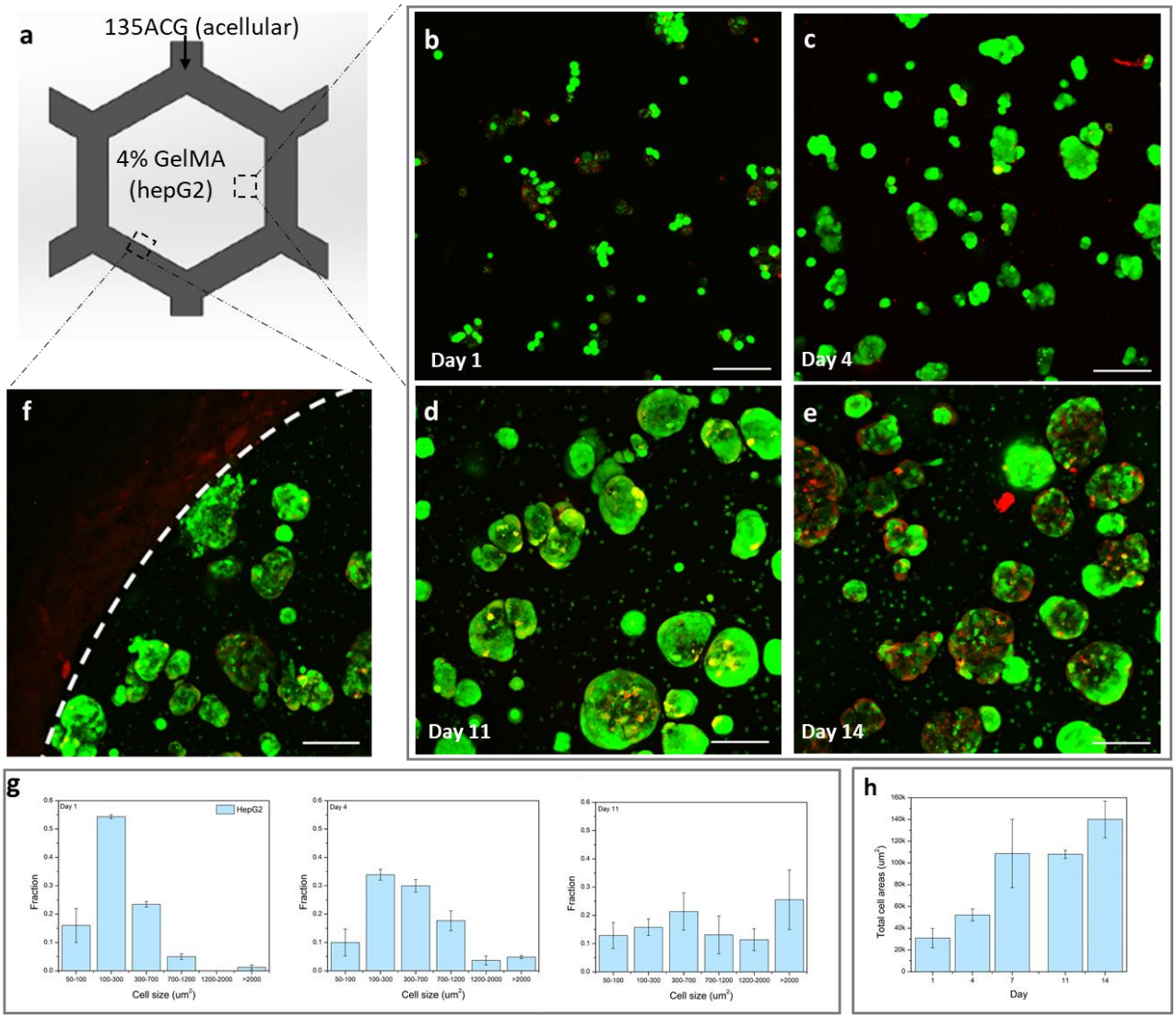

Figure 3.13 HepG2 cell growth, proliferation and morphology in GelMA. (a) Schematic of construct S2. (b-e) Fluorescence images of hepG2 in 4% GelMA on days 1, 4, 11, and 14 (green: live cells; red: dead cells). (f) HepG2 at the boundary of 135ACG and GelMA (dashed line). Scale bars are 100 µm. (g) HepG2 cell/ cluster area distribution on days 1, 4, and 11. (h) Total hepG2 cell spreading area over a 14-day period.

3.3.7 Cell Behavior in Bioprinted Bi-Cellular 3D Constructs

To investigate the effect of co-culturing NIH/3T3 cells with hepG2 cells in the bioprinted constructs, systems with direct intercellular contact (S3) and non-contact (S4) co-culture systems, as

described in **Figure 3.14a** and **Figure 3.14a**, were fabricated separately. To generate S3, acellular 135ACG honeycombs were first printed, followed by depositing a homogeneous mixture of hepG2 and NIH/3T3 fibroblasts in GelMA (4%) to fill the cavities. Both types of cells exhibited round morphology on day 1 (**Figure 3.14b**). Similar to S2, spheroids were observed to form over time in S3 (**Figure 3.14 b-d**), but with both cell types presenting in the clusters. Elongation and spreading of individual NIH/3T3 cells was also observed in S3, as shown in **Figure 3.14d**. The protrusion of NIH/3T3 cells into stiff 135ACG (orange arrow) and the parallel alignment of NIH/3T3 cells along the boundary of the two different matrices (135ACG and GelMA) (yellow arrow) were observed on day 14 (**Figure 3.14e**). Cell area distribution and total spreading areas in S3 were analyzed and plotted in **Figure 3.14 f-g**. Compared to S2, there were a much lower percentage of cell/clusters with an area larger than 2000 μm^2 and a higher percentage below 700 μm^2 in S3, indicating that spheroids formed in the hepG2/NIH/3T3 co-culture were smaller than those in the hepG2-only culture and some NIH/3T3 cells propagated as single cells (**Figure 3.14f**). The total cell spreading area increased persistently over the two weeks (**Figure 3.14g**), instead of plateauing on day 7 as in S2, which is ascribed to fibroblast growth.

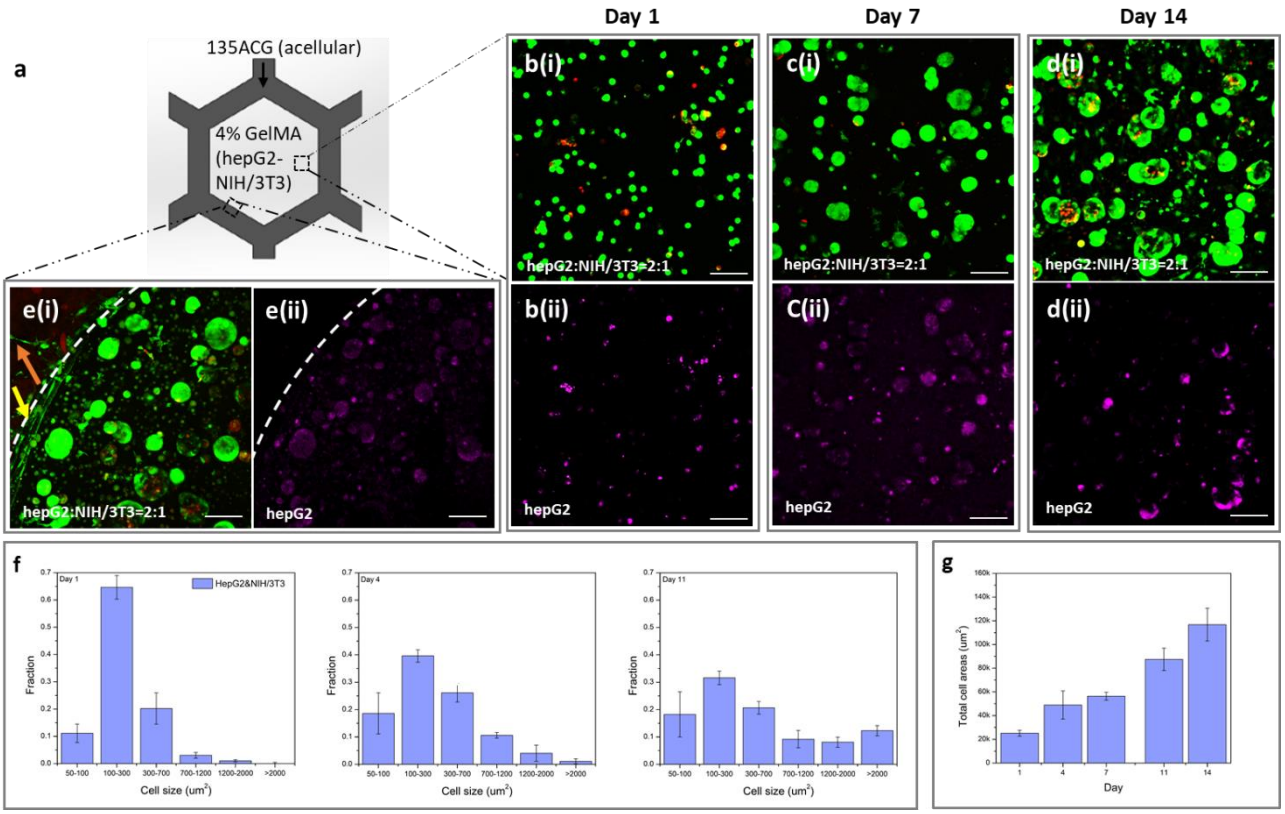

Figure 3.14 Mixed NIH/3T3 and hepG2 cell growth, proliferation, and morphology in GelMA. (a) Schematic of construct S3. Fluorescence images of the hepG2 and NIH/3T3 mixture (initial densities of hepG3: NIH/3T3=2:1) on (b-i) day 1, (c-i) day 7, and (d-i) day 14 (green: live cells; red: dead cells). The images of hepG2 cells stained with Qtracker 655 (magenta) on (b-ii) day 1, (c-ii) day7, and (d-ii) day 14. (e) Cells at the boundary of 135ACG and GelMA (dashed line). Scale bars are 100 µm in b-e. (f) Cell/cluster area distribution in S3 on days 1, 4, and 11. (g) Total cell spreading area in S3 over a 14-day period.

To fabricate S4, NIH/3T3-laden 135ACG was used to print the honeycombs and then hepG2-laden GelMA was used to fill the cavities. Interestingly, the two types of cells migrated towards each other over time (**Figure 3.15 b-d**). The spreading of NIH/3T3 cells in 135ACG (white arrow) was observed on day 7 (**Figure 3.15c**), aligning parallel to the boundary of the two bioinks on day 14 (**Figure 3.15e**).

Moreover, direct intercellular contact of the two types of cells at the boundary occurred as shown in **Figure 3.15e** labeled with a blue circle. The cell size distribution of NIH/3T3 and hepG2 cells at the boundary region were analyzed separately and plotted as stacked columns in **Figure 3.15 f-g**. The trend of the hepG2 cell/cluster area distribution in S4 (**Figure 3.15f**) was the same as that in S2. In contrast to hepG2, the size of fibroblasts was smaller, mainly in the range of 50-700 μm^2, and did not significantly change over time. It can be explained by the fact that NIH/3T3 cells grew in the form of single cells and did not aggregate over time. Moreover, the total hepG2 cell spreading area in S4 plateaued on day 7 (**Figure 3.15g**).

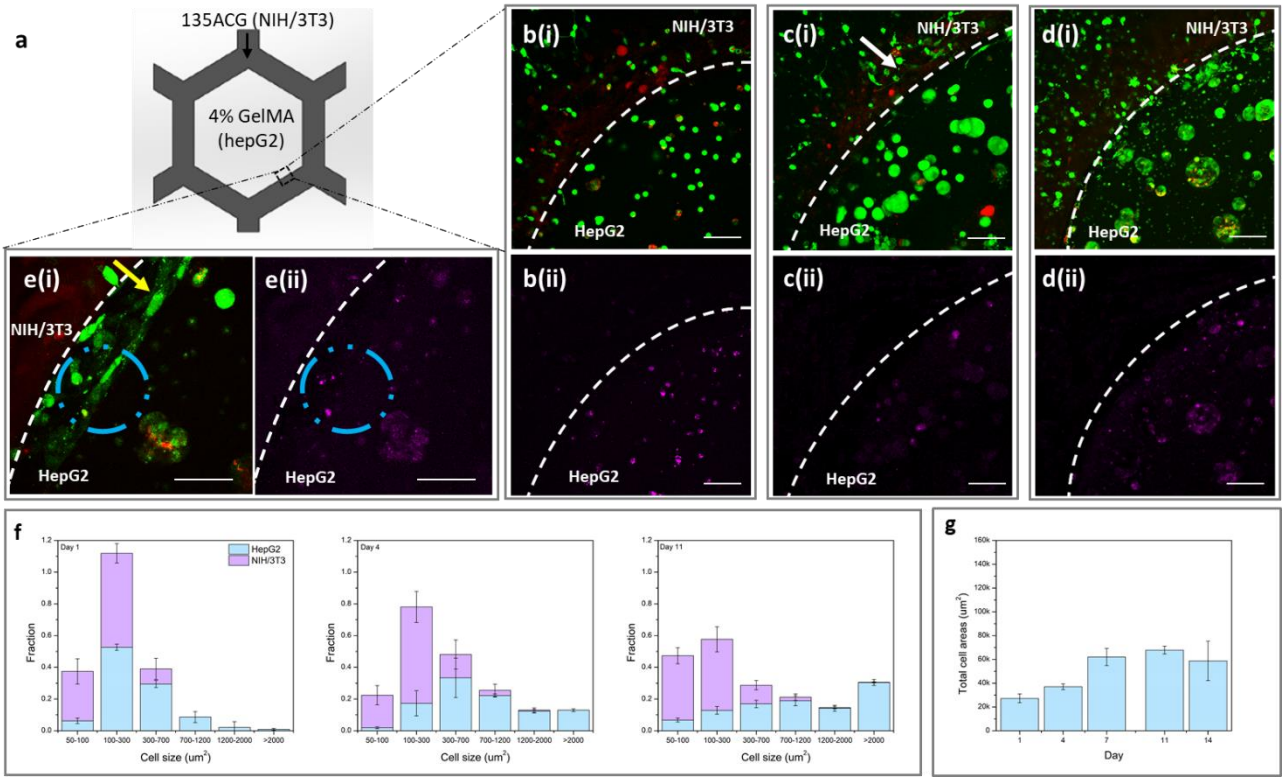

Figure 3.15 Adjacent NIH/3T3 (in 135ACG) and hepG2 (in GelMA) cell growth, proliferation and morphology. (a) Schematic of construct S4. Fluorescence images of both types of cells near the boundary of 135ACG and GelMA (dashed line) on (b-i) day 1, (c-i) day 7, and (d-i) day 14 (green: live cells; red: dead cells). Images of hepG2 cells stained with Qtracker 655 (magenta) on (b-ii) day 1, (c-

ii) day 7, and (d-ii) day 14. (e) Zoomed-in images of the cells at the boundary. Scale bars are 100 µm in (b-d) and 50 µm in (e). (f) Cell/cluster area distribution of hepG2 spheroids and NIH/3T3 cells separately on days 1, 4, and 11. (g) Total hepG2 cell spreading area over a 14-day period.

3.3.8 Albumin Secretion

One of the most important functions of hepatocytes is the synthesis of serum protein, specifically serum albumin. Thus, to assess hepG2 cell function in 3D mono-cellular (S2) and bicellular co-culture systems (S3, S4), levels of albumin production were measured over two weeks and compared to that in a 2D system (S0). In each culture, the amount of albumin produced was measured every 24 hours and plotted in relative to the level on day 1 (**Figure 3.16**). Albumin secretion hiked up dramatically in all 3D cultures starting on day 7 and reached about 35-40 times on day 14, even though hepG2 proliferated much faster in a 2D culture, and cell numbers in 3D cultures plateaued on day 7 (**Figure 3.12a**). This result indicates that, compared to culturing in 2D, encapsulation of hepG2 in the 3D GelMA ECM promoted per-cell albumin secretion significantly. From day 7 to 14, higher amount of albumin was produced from the co-culture system which could be explained by the presence of NIH/3T3 fibroblasts. Among the 3D systems, albumin secretion was slightly higher in the hepG2/NIH/3T3 co-cultures (S3, S4) than that in the hepG2-only culture (S2), consistent with literature data. Previous studies have shown that hepatocytes co-cultured with non-parenchymal cells in a 3D environment exhibited enhanced liver functions, such as albumin secretion and urea production, when compared to the traditional 2D and mono-cellular 3D culturing techniques.[161,204,205] Jeong *et al.* have found that rat albumin secreted by fibroblasts in cell media was negligible,[206] meaning that albumin was only produced by hepG2 cells. Interestingly, there was no significant

difference in the level of albumin production in the co-cultures with direct (S3) and in-direct intercellular contacts (S4), suggesting that the physical contact of the dual cell lines might not be necessary to influence the hepatocyte function, rather the fibroblast-secreted factors matter.[206]

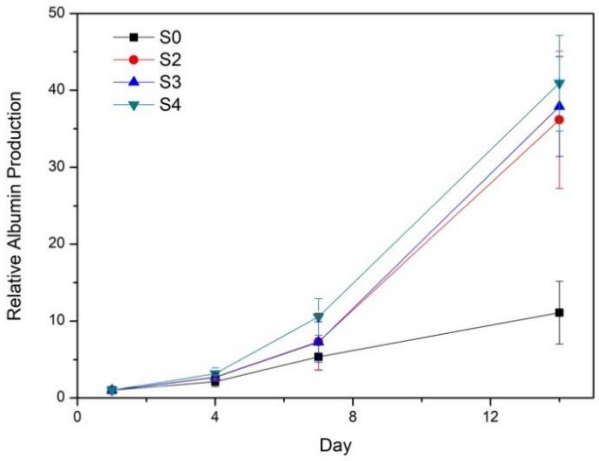

Figure 3.16 Relative albumin production by hepG2 cultured in 4 different systems: S0 (2D), S2, S3, and S4 on days 1, 4, 7, and 14.

3.4 Conclusions

We have developed two types of bioinks and methods suitable for the ME printing of heterogeneous 3D constructs. A CNC-incorporated alginate/GelMA hybrid bioink (135ACG) was formulated for precision printing of high aspect ratio cell-laden structures. Due to the excellent shear-thinning and solid-like properties of 135ACG, honeycombs (with a 0.48 mm wall thickness) up to 3.4 mm and 6.8 mm were demonstrated with free-form printing and embedded printing respectively. After UV crosslinking, scaffolds printed with 135ACG were also confirmed to offer a stiff ECM, with a compressive modulus on the order of 10 KPa, to accommodate the adhesion, spreading, and proliferation of fibroblasts, an example stromal cell line. A softer GelMA hydrogel that possessed

stiffness (compressive modulus ~ 2.5 kPa) comparable to the native liver tissue was used to encapsulate hepatocytes (hepG2). Four different 3D liver lobule-mimetic structures with precise placement of hepG2 and NIH/3T3 cells were bioprinted. The four structures allowed us to observe effects of mechanical cues and intercellular interactions on cell behaviors, including hepatic spheroid formation, cell alignment and migration at the boundaries of stiff/soft ECMs, as well as albumin secretion, the most important function of hepatocytes. Interestingly, fibroblasts thrived in stiff 135ACG matrix and aligned at the 135ACG/GelMA boundary due to durotaxis, while hepG2 formed spheroids exclusively in the soft GelMA matrix. Hepatic spheroids formed by a homogeneous mixture of hepG2/NIH/3T3 were found to be smaller than those formed by hepG2 only. Improved albumin production was observed when hepG2 cells were co-cultured with NIH/3T3 both with and without direct intercellular contact, indicating that improved hepatic function can be attributed to soluble chemical factors. Overall, our results demonstrated the great potential of the bioink materials and ME-based printing methods developed in this study, which offered new strategies to address the central challenge in tissue engineering to create complex constructs with multiple cell types and varying ECMs to recapitulate biological functions.

CHAPTER 4 Embedded 3D Printing of Vascular Constructs

4.1 Introduction

The ability to develop living functional tissues and organs to recapitulate the native tissue functions is rapidly growing in the field of tissue engineering and regenerative medicine. Integration of cell biology and materials science is the prerequisites for fabricating tissue and organs *in-vitro*. Tissues with relatively simple geometry, such as skin, have been successfully constructed, however, it remains challenging to accurately develop functional human tissues with more complex hierarchical structures. As such, 3D bioprinting, which allows precise positioning of biomaterials, has emerged as a promising strategy to fabricate complex biological constructs that imitate natural tissues and organs.[10] The potential impact of 3D bioprinting on fundamental biomedical research and its applications in regenerative and personalized medicine are enormous. The past few years saw a rapid rise in research on 3D bioprinting to develop enabling technologies, namely bioink materials, printing tools and methods. To address the challenges in creating large and heterogeneous 3D tissues, strategies to print in a supporting bath, namely embedded 3D printing, have been developed. Materials used for the supporting bath include viscous oil,[29] elastomer,[30] self-healing hydrogels,[31] and granular gel suspension[32–34]. The bath acts like a Bingham plastic, being rigid at low shear stress but flowing at higher shear stress.[26,31–33]

Here, we present a hybrid ink composed of glycidyl methacrylated poly(vinyl alcohol) (PVAGMA) and cellulose nanocrystal (CNC). Polyvinyl alcohol (PVA) hydrogel has been widely used in various areas owing to its high water content, low frictional behavior, and biocompability.[98–100] The elasticity

of PVA materials is similar to that of the human artery, making it uniquely suitable for constructing vascular phantoms. The abundant hydroxyl groups on the backbone of PVA not only make them hydrophilic but also increase the viscosity and elasticity of PVA solution over time which is induced by H-bonding.[101] PVA is crosslinked either physically (e.g. through freeze-thaw cycles), or chemically using crosslinkers such as glutaraldehyde, epochlorohydrin, and boric acid.[99,102] The physically crosslinked PVA aerogel driven by the phase separation benefits from the low cytotoxicity but with poor mechanical properties and structure stability.[99,103] In comparison, chemical crosslinkers are typically cytotoxic. Therefore, the UV crosslinkable PVA, which renders chemically crosslinked gels that are stable and biocompatible, is favored for tissue engineering and medical applications. PVA materials are typically strain-softening, a notable deficiency for mimicking human soft tissues which often exhibit a strain-stiffening behavior.[108] Therefore, nanomaterials, such as CNC, graphite, and methacrylate silica, and polymers, such as gelatin and chondroitin sulfate, are incorporated into PVA to make up for the deficiency.[99,103,107,207–210] For instance, graphite was incorporated into PVA to better mimic vessel elasticity and adjust the material attenuation and scattering properties for ultrasound imaging.[158,169] In this study, CNC is used as a nano-filler, replacing graphite, since graphite tends to sediment in the mixture and clog extruder nozzle. CNC not only enhances the mechanical strength of gels, but also introduces shear-thinning behaviors due to the alignment of the chiral nematic liquid crystalline domains.[127,129–131]

Recently, image-guided minimally invasive diagnostic imaging and therapeutic interventions techniques, like computed tomography scan (CT), magnetic resonance imaging (MRI), and ultrasound imaging, have significantly improved lives. They support accurate therapeutic procedure and help

guide and monitor the intervention for optimal results. Ultrasound, specifically, is widely used to image internal organs and aid in fluid management because it provides real-time, low-cost, and radiation-free imaging.[167] The field is constantly evolving for next-generation solutions, such as molecular imaging and imaging-guided ultrasound therapy.[108,168] Thus, *in-vitro* medical phantoms with adjustable biochemical and physical properties are in great demand for advancing diagnostic ultrasound techniques and exploring cardiovascular diseases mechanisms.

To evaluate the printability and feasibility of our bioink, PVAGMA/CNC, and supporting bath material, several constructs including carotid bifurcation and multi-segment hollow tubes were chosen as models. Further, hemodynamic study and ultrasound imaging of the printed vessel models were conducted. Taken together, our results demonstrate the great potential of our material compositions for 3D bioprinting of heterogeneous medical models, particularly applicable to ultrasound imaging.

4.2 Materials and Methods

4.2.1 Materials

Sodium carbonate, sodium bicarbonate, gelatin (type A, 300 g Bloom, from porcine skin), deuterium oxide (D_2O), calcium carbonate, D-(+)-gluconic acid δ-lacton, lithium phenyl-2, 4, 6,-trimethylbenzoyphosphinate (LAP), poly(vinyl alcohol) (PVA), glycidyl methacrylate (GMA), 4-dimethylaminopyridine (DMAP), and dimethyl sulfoxide (DMSO) were purchased from Sigma Aldrich. Xanthan gum was purchased from CP Kelco. PDMS were purchased from Dow Corning. Pharmaceutical grade sodium alginate (PROTANAL LF 10/60 FT) with 60–70% guluronate (G) residues

was acquired from FMC (Philadelphia, PA). 1-ethyl-3-(3-dimethylaminopropyl)carbodiimide (EDC) and N-hydroxysuccinimide (NHS) was purchased from G-biosciences and Alfa Aesar, separately. Cellulose nanocrystals were donated by Professor Michael K.C. Tam from the Department of Chemical Engineering at the University of Waterloo.

4.2.2 Synthesis of Glycidyl Methacrylate Modified Poly(vinyl alcohol) (PVAGMA)

PVAGMA was synthesized according to previously published work.[104,105,107,211] In brief, 20 g PVA powder was dissolved in 400 mL DMSO in a round bottom flask at 90 ℃ to obtain a 5 wt% PVA solution. DMAP (5 g), as a catalytic agent, was added into it after lowering the temperature to 60℃, followed by adding different amounts of GMA, ranging from 1 mL to 6 mL. The reaction mixture was purged with N_2 and stirred at 60℃ in dark for 24 hours. After that, the solution was dialyzed against DI water with a 12 kDa MWCO membrane at 50℃ for 4 days, followed by lyophilization and stored in dark at -20℃. NMR spectroscopy was utilized to confirm the obtained compounds and the degree of methacrylation. The lyophilized PVAGMA was dissolved in D_2O at 50 mg/mL and analyzed via proton nuclear magnetic resonance spectroscopy (^{1}H NMR).

4.2.3 Bioink Preparation

A 10 wt% PVAGMA solution with different degree of substitution (DOS) were prepared by dissolving PVAGMA foam in Milli-Q water at 90 ℃. LAP (0.5 wt%) was added into the PVAGMA solution after lowering the solution temperature to room temperature. CNCs were added to the mixture to get a final concentration of 4 wt% and vortexed for 5 min followed by centrifugation at 1500 g for 3 min. This step was repeated twice to disperse CNCs completely in PVAGMA solution. Then, the resulting mixture (PVAGMA/CNC hybrid) was sonicated at 37 kHz for 10 min.

4.2.4 Preparation of Supporting Bath Material for Embedded Printing

The supporting bath material for embedded 3D printing was prepared according to the procedure developed by Noor *et al*.[38] Briefly, sodium alginate (0.32 wt%), xanthan gum (0.25 wt%), and calcium carbonate (9.56×10^{-3} M) were dissolved in DI water and homogenized. Concentrated D-(+)-gluconic acid δ-lactone solution was added to the mixture to reach a final concentration of 19.15 mM and stirred constantly until the viscosity of the mixture increased and no precipitation of the calcium carbonate was observed. The mixture was then left at room temperature for 24 h. DI water was added to the mixture (4:1 volume ratio), homogenized, centrifuged at 11000 g for 20 min. The precipitated pellet was collected. Xanthan gum (2 wt%) was freshly prepared and added to the pellet at a volume ratio of 1:1. A homogeneous supporting bath was obtained through vigorous vortexing.

4.2.5 3D printer and Printing Procedure

A FlashForge Creator Pro (FlashForge, China) mounted with a custom-made syringe holder was used (**Appendix A**). The syringe was connected to an Ultimus V high precision dispenser (Nordson EFD, USA). 3D models were designed using SolidWorks and bioinks were loaded into 10 mL pneumatic syringes. A dual-syringe printing system was customized and utilized for multi-material printing as illustrated in **Appendix A**. In brief, one end of the Y-shape connector was attached to a long needle (7 cm) while the other two ends were attached to two check-valve connectors to avoid any back flow when pressure was on. Two syringes connecting to the Ultimus V high precision dispenser through two robust tubings were attached to the check-valve connectors. The switch of the pneumatic pressure on each syringe could be realized by a detented toggle control valve (Pneumadyne Inc.) connected to the pneumatic dispense. G-codes with a printing speed of 10 mm/s were generated by

ReplicatorG or Slic3r and modified to fit the embedded printing. Needles with different diameter were used based on the constructs dimensions. Spiral structures were first printed each time to determine the printing pneumatic pressure. The homogeneous supporting bath was transferred to a clear PMMA box or 50 mL centrifuge tube before printing. Food dyes were added to the ink to improve visualization. A snake eye UV light setup was used for *in-situ* crosslinking. After the printing process, the containers were exposed to UV light for 15 min to crosslink the hydrogels. Then the embedded printed constructs were washed with DI water to remove excess supporting bath materials followed by additional 15 min UV crosslinking.

4.2.6 Swelling

PVAGMA hydrogels with or without CNCs were casted in a rectangular PDMS mold and printed in supporting bath, followed by UV crosslinking for 15 min at ambient temperature. The casted and printed hydrogels with a dimension of 2 x 4 cm^2 were soaked in Milli-Q water for 72 hours. The hydrogels were taken out of water, dried with Kimwipes, and measured the length as L_t and width as W_t via a caliper. The swelling ratio (Q) was determined as relative length $(L_t\text{-}L_0)/L_0$, and relative width $(W_t\text{-}W_0)/W_0$.

4.2.7 Rheological Properties

The rheological measurements were conducted using a Bohlin-CS Rheometer with a cone-plate geometry (CP 4-40). The steady-state shear viscosities were measured with a shear rate in the range of 0.1 – 1000 s^{-1}. A strain-sweep test with a strain from 0.05% to 10% and a frequency at 1 Hz was

performed to determine the linear viscoelastic regions. The optimal strain was chosen to be 0.1% for the oscillation frequency test from 0.1 to 10 Hz.

4.2.8 Mechanical Properties

Dog bone-shaped samples were casted in PDMS molds (4 mm wide at middle narrow section, 70 mm in length, and 1 mm in thickness) and printed in a supporting bath (5 mm wide at narrow part, 47 mm in length, and 1.5 mm in thickness), separately. The samples were performed by using Universal Test Machine at a speed of 2 mm/s for modulus test and 0.2 mm/s for cyclic tensile tests. The tensile modulus was determined by the slope of the initial 10% strain, and the fracture strain and stress were obtained from the strain-stress curves.

4.2.9 Phantom Assembly

Due to the limitation of the operating volume of the 3D printer, a vessel tube with a length of 7 cm, inner diameter (ID) of 7 mm and wall thickness of 2 mm were printed for hemodynamic analysis and ultrasound imaging. The printed vessels were attached to two Tygon tubings with an ID of 6.35 mm, an outer diameter (OD) of 7.94 mm, and a length of approximately 15 cm through bridging polymers (**Figure 4.1a**). Briefly, polyallylamine (PAA) was dissolved in 0.1 M MES buffer at 2 % (v/v) and the pH was adjusted to 6. EDC and NHS were added to the PAA solution to a final concentration of 12 mg/mL. The bridging solution was applied to inner surface of the two ends of the printed vessel and the Tygon tubings which were covered with double-sided acrylic tapes at ends (3M 8213CL). Compression was applied to the connection region for 10 min and left in fridge overnight.[212]

Two holes were drilled at the inlet and outlet sides of an open-top phantom box that has a dimension of 30 x 6 x 7 cm^3 and installed with two quick-fit flow connectors. After the assembled

vessel tube was mounted into the phantom box, a metal rod was inserted into the tubing to straighten it and prevent it from collapsing. Subsequently, a tissue-mimetic solution made of 10 wt% gelatin was poured into the phantom box and left in fridge until gelled, and the phantom box was then connected to a customized programmable pump system with controlled constant and pulsatile flow modes via the inlet and outlet connectors as illustrated in **Figure 4.1b**. A fluid reservoir provided water for circulation at a certain flow rate or pulsatile flow. Water was perfused at a constant flow rate of 5 mL/s to remove air bubbles inside the flow system before testing.

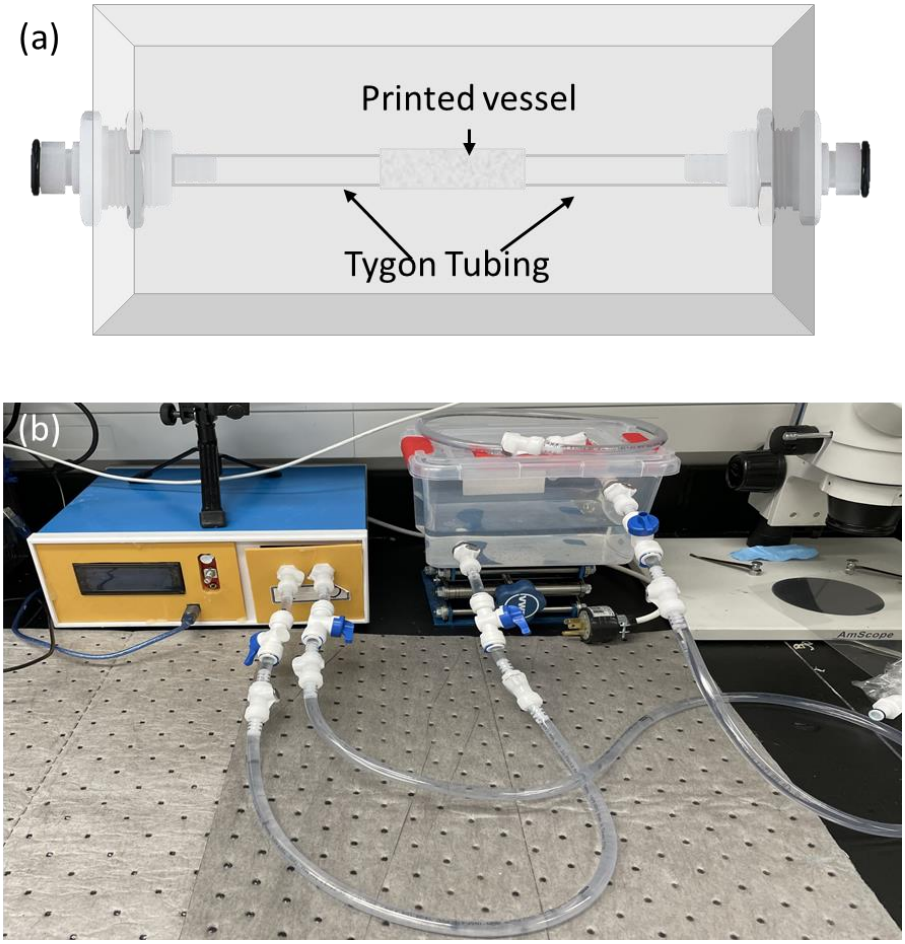

Figure 4.1 Phantom assembly. (a) Schematic of the phantom box. The printed vessel was attached to Tygon Tubings via acrylic tape and a bridging polymer solution. (b) Images of the flow pump working system with the phantom box connected to the pump and a reservoir.

4.2.10 *In-vitro* Hemodynamics Analysis of Vascular Phantom

For the burst pressure analysis, a pressure gauge was attached to the inlet of the phantom box and the valve at the outlet of the phantom box was closed. The vessel was filled with water at a rate of 2 mL/s until failure and the burst pressure (P) was recorded by taking a video of pressure gauge readings. The wall burst tensile stress (T) in the circumferential directions was calculated using Laplace's Law

$$T = \frac{Pr}{h},$$

where r is the vessel radius and h is the vessel wall thickness. A thin slice of the vessel at rupture region was cut and examined under a microscope to determine r and h. The average shear stress (τ) at the vessel wall was calculated using Poiseuille's law.

$$\tau = \frac{4\mu Q}{\pi r^3},$$

where Q is the volumetric flow rate, μ is water viscosity.

To test the durability and stability of the vessel, flow rate in the range of 1 to 27 mL/s were initially investigated using the phantom assembly. Then, pulsatile flow that features carotid pulses (60 beats/min with a peak flow of 27 mL/s) were fed continuously through the vessels for 10 days.

4.2.11 Ultrasound Imaging and Signal Processing

Ultrasound imaging experiments were conducted to visualize and characterize the distention property of different segments of the printed vessel phantoms. PVAGMA with a DOS of 2% and 4% were dissolved in water to prepare 10 wt% PVAGMA solution followed by adding 4 wt% CNC to get the final bioink materials, namely PVAGMA2/CNC and PVAGMA4/CNC. To facilitate comparative analysis, experiments were conducted on three different models, that is (1) a single-segment vessel

made from PVAGMA2/CNC; (2) a single-segment vessel made from PVAGMA4/CNC; and (3) a three-segment vessel in which the middle segment (lesion) was printed with PVAGMA4/CNC and the two flank were printed with PVAGMA2/CNC. An L14-5 linear array transducer was positioned to image the phantom's long axis using a research scanner that was equipped with a pre-beamformed data acquisition system. Images of the non-pressurized vessels were first captured. Videos of the vessel wall movement under carotid pulse-mimetic pulsatile flow were recorded. Frames at the peak flow rate were captured for further analysis. Vessel wall thickness and diameter were measured using the built-in scale in the scanner via ImageJ. Each value was calculated based on an average of six measures.

4.3 Results and Discussion

4.3.1 Preparation of PVAGMA

Photocrosslinkable PVA, PVAGMA, was synthesized through transesterification and epoxide ring-opening between PVA and GMA under basic conditions as illustrated in **Figure 4.2a**.[104] Six PVAGMA samples (namely, PVAGMA0.25, PVAGMA0.5, PVAGMA1, PVAGMA2, PVAGMA4, and PVAGMA6) were prepared by changing the molecular ratio between PVA and GMA as listed in **Table 4-1**. The degree of substitution (DOS) was confirmed by ^{1}H NMR spectra (**Figure 4.2b**) and determined by the relative integration of the vinyl protons peaks at 6.1 and 5.8 ppm with respect to the unsubstituted methane moiety at 3.5-4.3 ppm.[106] All of the six PVAGMAs dissolved easily in water at a concentration of 10 wt%, but the solution became semitransparent when the DOS was higher than 4%. When 10 mL GMA was added to 20 g PVA, the resulting product did not dissolve in water due to the introduction of hydrophobic methacryloil groups at a high density. Additionally, the PVAGMA6 hydrogels were too

fragile, thus swelling and mechanical measurements on PVAGMA6 hydrogels were not performed.

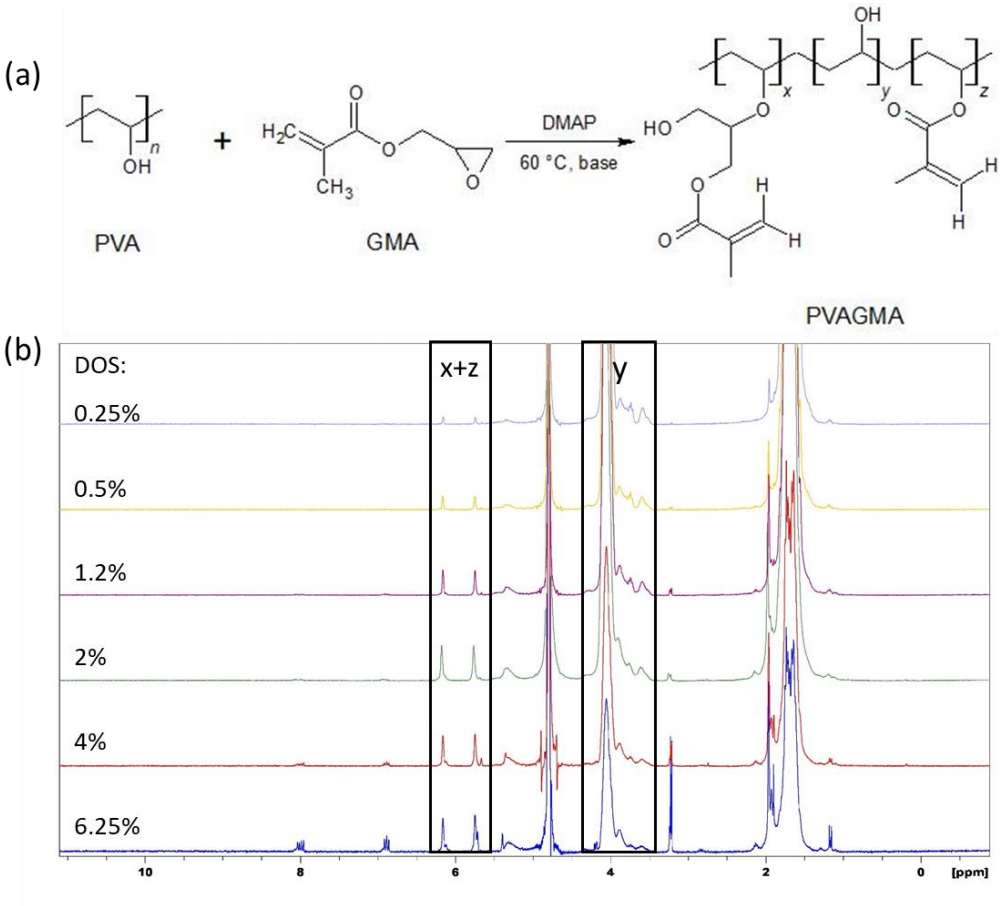

Figure 4.2 (a) Synthesis of photocrosslinkable PVAGMA. (b) ^{1}H NMR spectra of PVAGMA with different DOS.

Table 4-1 Summary of the synthesized PVAGMA

PVA (g)	GMA (mL)	DOS	Formulation
20	1	0.25%	PVAGMA0.25
	2	0.5%	PVAGMA0.5
	3	1.2%	PVAGMA1
	4	2%	PVAGMA2
	6	4%	PVAGMA4
	8	6.25%	PVAGMA6
	10	N/A	N/A

4.3.2 Rheology of the Inks and Granular Supporting Bath Material

The rheological properties of PVAGMA and PVAGMA/CNC hybrid inks were first tested in order to demonstrate the feasibility of various inks for microextrusion-printing. As shown in **Figure 4.3 a-b**, pristine 10 wt% PVAGMA solutions exhibit Newtonian behavior with viscosity about 1 Pa s over a wide range of shear rates (0.1 to 10 s^{-1}) with no significant difference between PVAGMA2 and PVAGMA4, suggesting that the slight difference in DOS does not influence the viscosity of the PVAGMA solutions. Both solutions are slightly shear-thinning above 10 s^{-1}. The PVAGMA coils disentangle and realign in the shear direction with increasing shear rate, leading to the observed shear-thinning behavior after a critical shear rate is reached. Adding high aspect ratio CNC nano-fillers into the PVAGMA solutions significantly reshaped the rheological curves compared to the pure PVAGMA counterparts. PVAGMA/CNC hybrids exhibited a pronounced shear-thinning property over the entire shear rate range with a curve slope of approximately -0.35. Both solutions possessed a viscosity of 0.5 Pa s at a shear rate of 1000 s^{-1}, about three orders of magnitude lower than that at 0.1 s^{-1}. The apparent decline in viscosity as a function of shear rate could be ascribed to the shear-thinning property of CNC itself and the strong intermolecular interactions, i.e. hydrogen bonding, between PVAGMA and CNC. At static state, CNCs are homogenously dispersed and entangled in PVAGMA matrix. When a shear stress is applied, the coiled polymer network elongates, rearranges, and lowers the inks' viscosity. As the shear stress increases, the physical interaction between CNC and PVAGMA begins to dominate the viscoelasticity via hydrogen bonding. Further, as shown in **Figure 4.3 c-d**, the viscous moduli G" of both pristine PVAGMA and PVAGMA2/CNC were higher than elastic moduli G' over the entire frequency range of 1 to 10 Hz and the elastic modulus of pure PVAGMA (~

10 Pa) was lower than that of the hybrid (~ 100 Pa). This data indicates that they were all liquid-like, but the PVAGMA2/CNC hybrid was stronger than the pure PVAGMA. In contrast, the elastic modulus G' of PVAGMA4/CNC was higher than its viscous modulus G" at low frequencies, suggesting that PVAGMA4/CNC was more solid-like at lower frequencies.

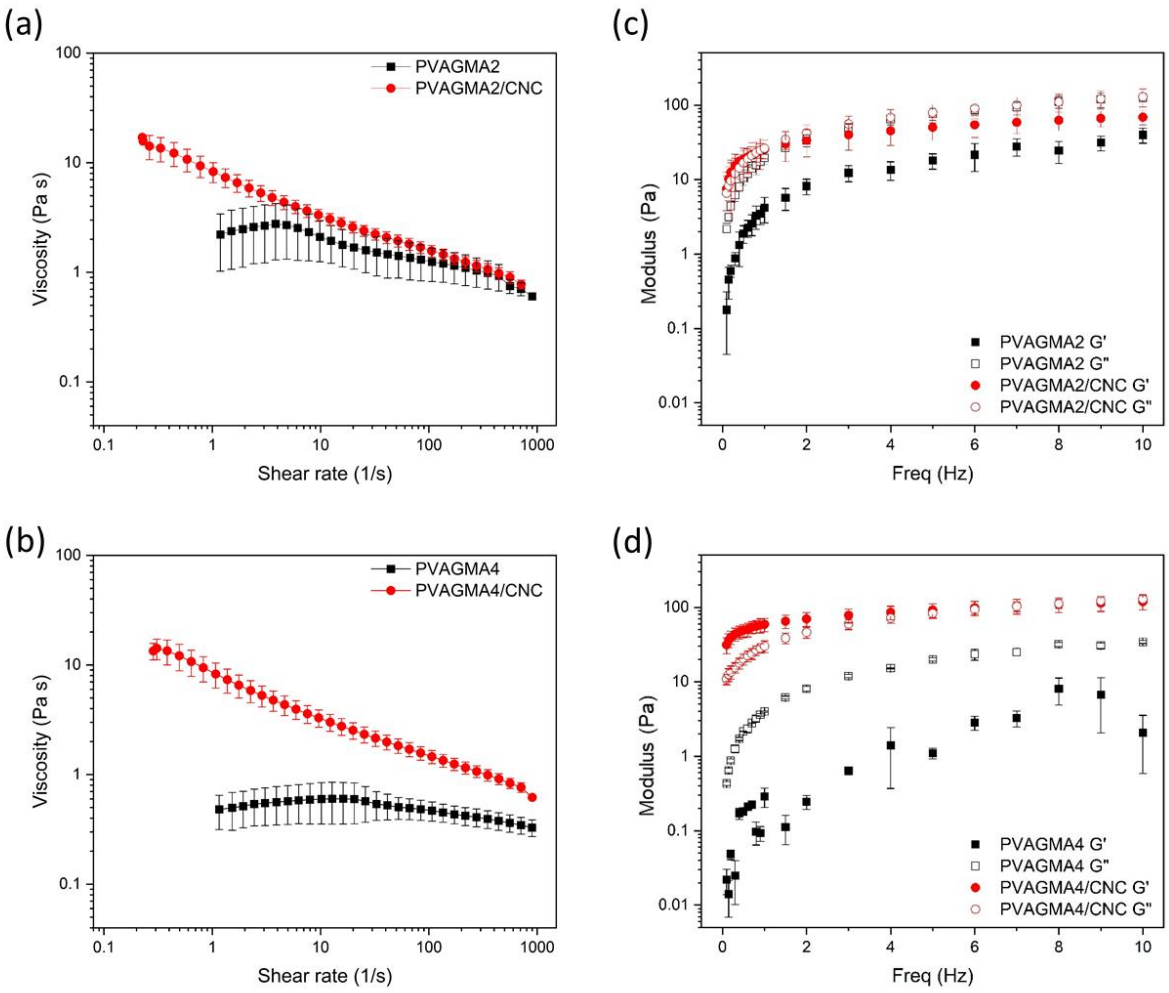

Figure 4.3 Rheological properties of the bioinks. Flow curves of (a) PVAGMA2 and PVAGMA2/CNC and (b) PVAGMA4 and PVAGMA4/CNC. Elastic moduli (G') and viscous moduli (G") as a function of oscillatory frequency of (c) PVAGMA2 and PVAGMA2/CNC and (d) PVAGMA4, and PVAGMA4/CNC.

A transparent granular supporting bath material (ALG-XG) composed of partially crosslinked alginate microparticles and xanthan gum was prepared based on the method developed by Noor et

al.[38] Rheological measurements were conducted to explore the ability of ALG-XG to hold the printed structures. The supporting bath exhibited a shear-thinning behavior with a viscosity of approximately 30 Pa s at 0.1 s^{-1} (**Figure 4.4a**), and its yielding stress was approximately 5 Pa (**Figure 4.4b**). Additionally, as shown in **Figure 4.4c**, the elastic modulus is larger than the viscous modulus over the frequency range of 1 to 10 Hz, suggesting the mixture is solid-like.

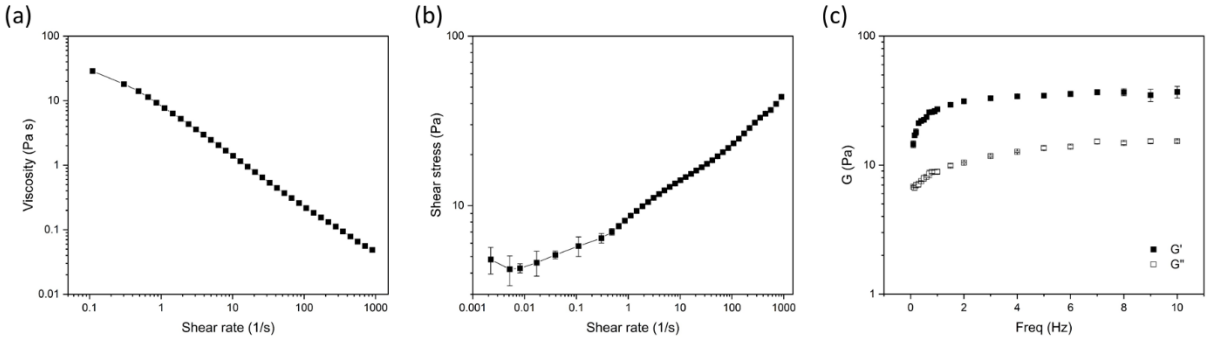

Figure 4.4 Rheological properties of supporting bath material. (a) Flow curve, (b) yielding stress, and (c) moduli of the supporting bath material (ALG-XG).

4.3.3 Swelling of PVAGMA Hydrogels

The swelling property of hydrogels is critical to their application in tissue engineering because it can influence the mechanical property and permeability of the hydrogels.[21] The swelling property of molded and printed PVAGMA and PVAGMA/CNC hybrid hydrogels in water is displayed in **Figure 4.5**. All molded and printed hydrogels exhibited rapid swelling during the initial 6 hours and reached the equilibrium swelling state within 24 hours (**Figure 4.5 a-d**). The swelling degree proportionally decreased with increasing DOS (**Figure 4.5e**). For instance, the dimensions of PVAGMA0.25 gels expanded by 30% within 6 hours while no significant changes in the sample dimensions were observed in PVAGMA2 hydrogels. In comparison, approximately 14% shrinkage occurred in PVAGMA4

hydrogels due to the different inter-chain distances caused by the high crosslinking density of hydrogels (**Figure 4.5a**). Two factors, inter-chain distances and crosslinking density, affect the water retention capabilities of a hydrogel. High inter-chain distances allow water to be easily absorbed by the flexible hydrogel matrix, whereas high crosslinking density in the hydrogel limits the matrix network expansion, thus decreasing the water retention capability. Therefore, as shown in **Table 4-2**, the porosities of the hydrogels decline as DOS increases. Moreover, the incorporation of CNCs in the hydrogels causes the swelling degree to increase at a fixed DOS owing to the abundant hydrophilic groups on the CNC surface, which favors the retention of water in the hydrogel network. Rectangular strips were then printed using the various pure PVAGMA and hybrid PVAGMA/CNC pre-gel solutions through embedded printing to investigate the relationship between swelling and printing directions. Based on **Figure 4.5f**, there was no significant difference in the swelling ratio along (relative width) and perpendicular to (relative length) the printing direction, suggesting the optimal integrity and isotropic property of the printed patterns. However, the printed hydrogels exhibited slightly higher swelling behavior compared to molded samples and the addition of CNC did not influence the swelling degree of printed pristine PVAGMA hydrogels.

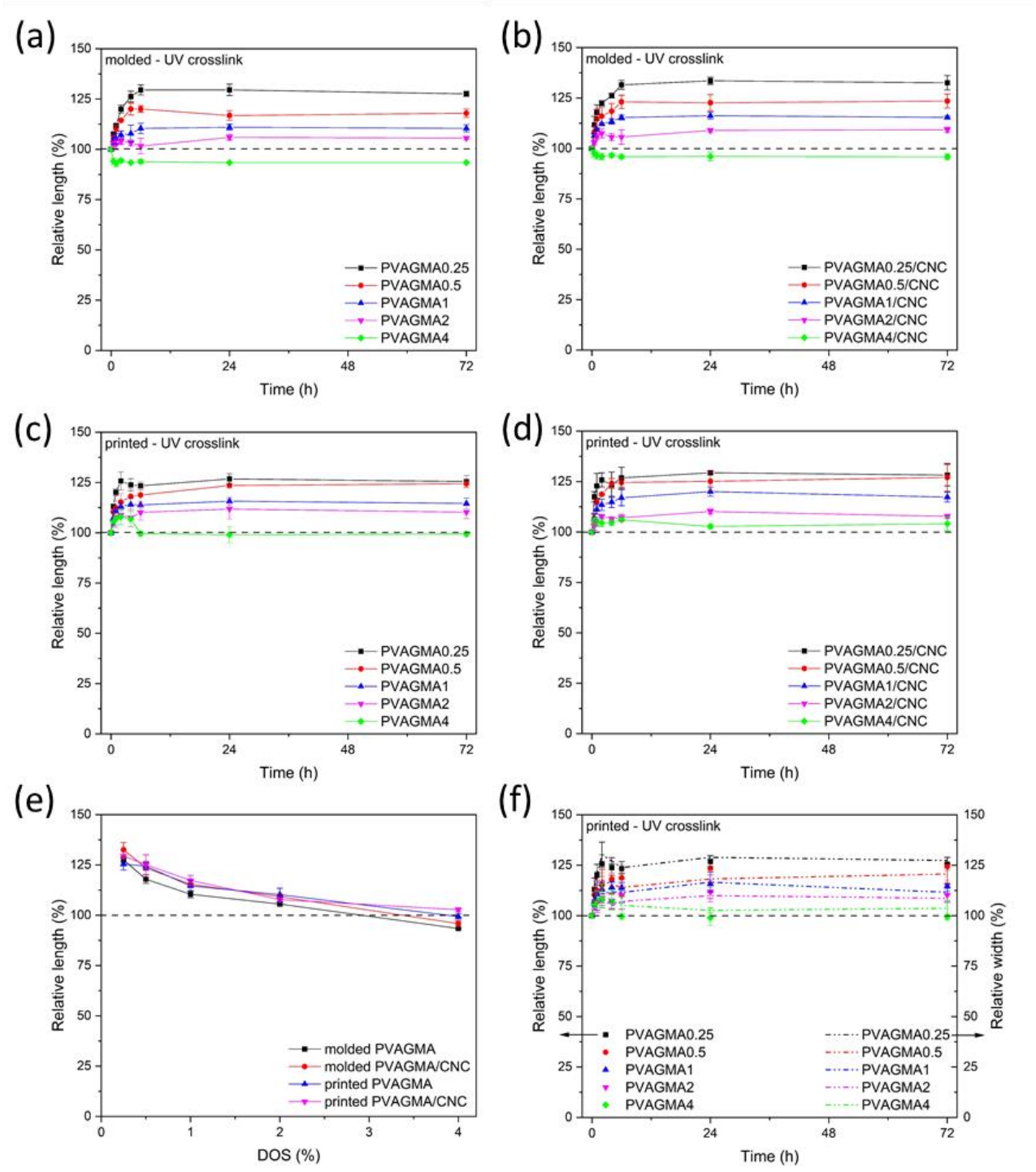

Figure 4.5 Swelling properties of pure PVAGMA and PVAGMA/CNC hybrid hydrogels. Swelling kinetics of (a) molded PVAGMA, (b) molded PVAGMA/CNC hybrid hydrogels, (c) printed PVAGMA, and (d) printed PVAGMA/CNC hybrid hydrogels with different DOS. (e) Swelling degree as a function of DOS of molded and printed pure PVAGMA and PVAGMA/CNC hybrid hydrogels. (f) Swelling kinetics of

printed photocrosslinked PVAGMA hydrogels along and perpendicular to printing directions.

Table 4-2 Summary of the porosity of molded and printed PVAGMA hydrogel with different DOS

	PVAGMA (%)		PVAGMA/CNC (%)	
	Molded	Printed	Mold	Printed
PVAGMA0.25	93.81±1.56	94.61±2.57	93.81±1.56	97.43±3.44
PVAGMA0.5	86.21±2.38	97.3±1.46	97.08±2.46	98.76±8.3
PVAGMA4	86.97±4.53	90.73±7.1	87.97±4.95	94.30±3.32

4.3.4 Mechanical Property of PVAGMA Hydrogels

As a potential vascular phantom, the hydrogels are expected to possess comparable mechanical strength to that of blood vessel substitutes. It has been found that the DOS of the PVAGMA hydrogels influenced their tensile properties. PVAGMA hydrogels with a relatively low DOS exhibited a high fracture strain but a lower tensile modulus, whereas hydrogels with a higher DOS were susceptible to fracture at a lower tensile load with a higher tensile modulus. For instance, PVAGMA0.5 hydrogels ruptured when it was stretched two times of their initial length, while PVAGMA4 ruptured after 75% elongation (**Figure 4.6a**). The values of PVAGMA hydrogels' tensile moduli ranged from 21.80 ± 6.59 kPa to 123.45 ± 11.82 kPa as illustrated in **Figure 4.6b**. It can be inferred that for pure PVAGMA hydrogels with ultralow DOS, the reactive methacryloyl groups are far away from each other leading to the formation of long and flexible polymer chains. Thus, the gels can expand and deform without damaging the polymer network both at microscopic and macroscopic levels. By increasing polymer DOS, the additional crosslinking sites limit the mobility of the polymer chains, leading to lower gel stretchability. Interestingly, with the addition of borax crosslinking, PVAGMA0.5 did not break within

the test range (up to 400% strain) and the fracture strain and tensile moduli of PVAGMA hydrogels with higher DOS increased slightly as well as shown in **Figure 4.6 c-d**. This is attributed to the reversible didiol-borax complexation between borax and non-reacted –OH groups in PVAGMA, which provides the hydrogels with an effective energy-dissipating mechanism.[213,214]

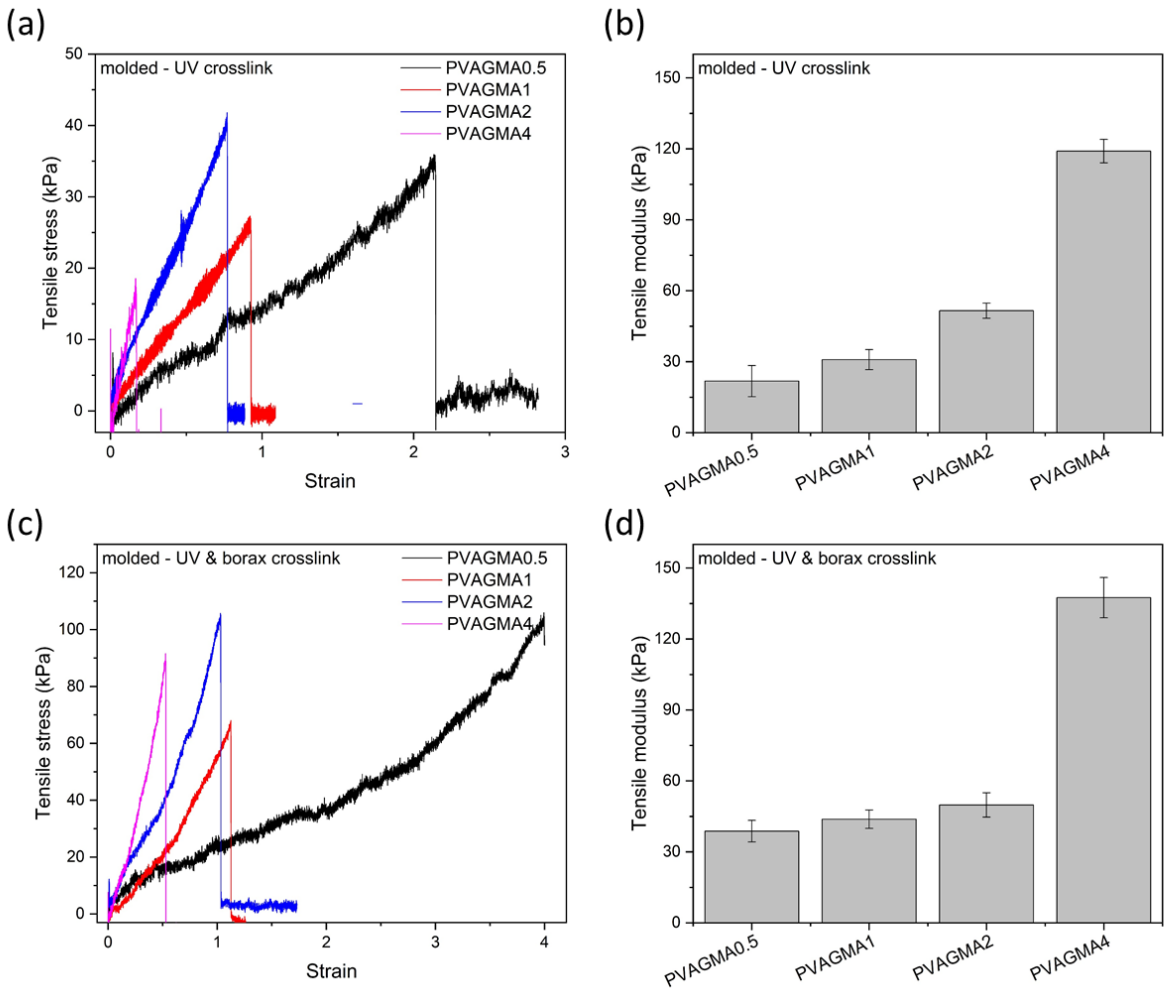

Figure 4.6 Mechanical strength of PVAGMA hydrogels with different DOS and crosslinking methods. (a) Tensile stress-strain curves and (b) tensile modulus of different UV-crosslinked PVAGMA hydrogels. (c) Tensile stress-strain curves and (d) tensile modulus of different dual-crosslinked PVAGMA hydrogels.

Due to the obvious swelling behavior and low mechanical strength of hydrogels with low DOS (<

2%), uniaxial tensile measurements were conducted on PVAGMA2 and PVAGAM4 hydrogels. The curves of tensile stress as function of strain for PVAGMA and PVAGMA/CNC hybrid hydrogels are presented in **Figure 4.7**. Compared to the pure PVAGMA counterparts, molded PVAGMA/CNC hybrid gels possessed higher fracture stress, ultimate strain, tensile modulus, and toughness. For instance, 1.76/1.18 and 2.36/1.09 fold increase in fracture stress/tensile modulus were found for the hybrid hydrogels as compared to pristine PVAGMA2 and PVAGMA4 gels, respectively (**Figure 4.7 a-b**). The enhancements are mainly attributed to the solid CNC nanorods and the macromolecular chain entanglements on CNC surface. Stress applied on the network is transferred from the PVAGMA polymer network to the nano-fillers, which prevents crack propagation at high deformation.[215] Additionally, the interfacial interactions between PVAGMA and CNC via hydrogen bonds serve as reversible sacrificial bonds to dissipate energy when tensile stress is applied.[215] Moreover, because CNC nanorods were randomly dispersed in the PVAGMA matrix, they tended to re-align along the stretching direction in the hybrid matrix upon tensile loading, which can further dissipate energy and increase the resistance against crack failure.[216] Therefore, both H-bonding and entangle-disentangle of the flexible polymer chains favor the improved tensile property of the hybrid hydrogels. However, unlike pure PVAGMA hydrogels, the additional borax crosslinking had little influence on the fracture strain of the hybrid hydrogels as shown in **Figure 4.7c**. Furthermore, the borax crosslinking did not change the tensile modulus significantly in all compositions. This could be due to the hydrogen bonding between PVAGMA and CNC that reduces the amount of available -OH groups on PVAGMA to react with borax.

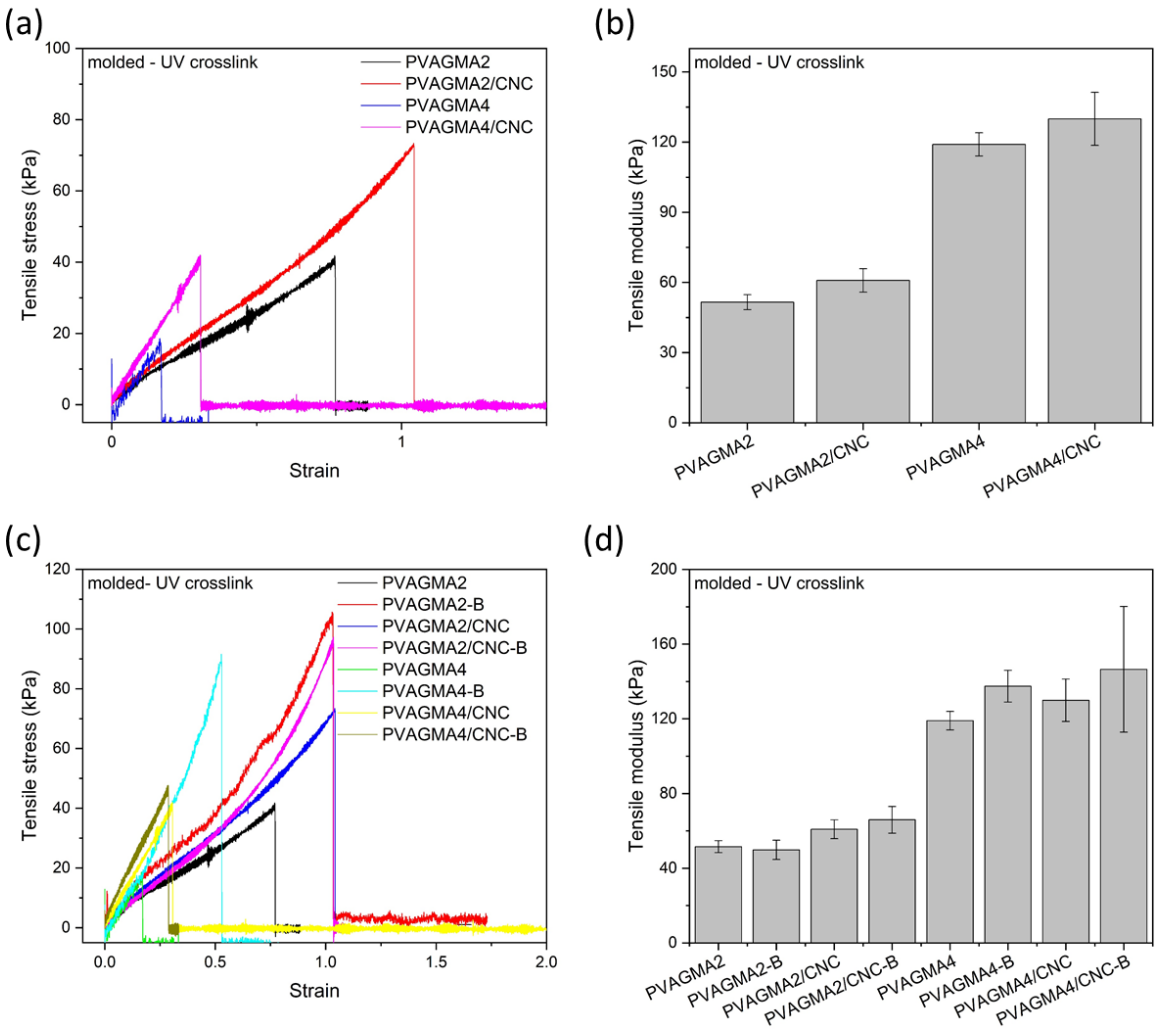

Figure 4.7 Mechanical characterization of molded pure PVAGMA2 and PVAGMA4 and hybrid PVAGMA2/CNC and PVAGMA4/CNC hydrogels. (a) Tensile stress-strain curves and (b) tensile moduli of molded UV-crosslinked hydrogels. (c) Tensile stress-strain curves and (d) tensile moduli of molded hydrogels with a DOS of 2% and 4% with or without secondary borax crosslinking. (B in ink formlations is short for borax crosslinking.)

Additional uniaxial tensile tests were performed on embedded printed hydrogels to compare molded and embedded printed samples. Noticeably, the printed samples showed lower ultimate strains but with a similar tensile modulus as compared to the molded ones (**Figure 4.8 a-b**). For instance, the molded PVAGMA2 hydrogels had an ultimate strain of 104%, about 3.06 times that of

the embedded printed hydrogels, and a tensile modulus of 51.55 ± 3.19 kPa, about 1.19 times that of the embedded printed hydrogels. This is expected because of the layer-by-layer fabrication strategy, and also indicates that mechanical properties of the printed structures can be further improved by adjusting the printing method and supporting bath material. Similar to the effect on UV crosslinked molded hydrogels, the additional borax crosslinking did not affect the fracture strain and tensile modulus in the printed samples, as illustrated in **Figure 4.8 c-d**.

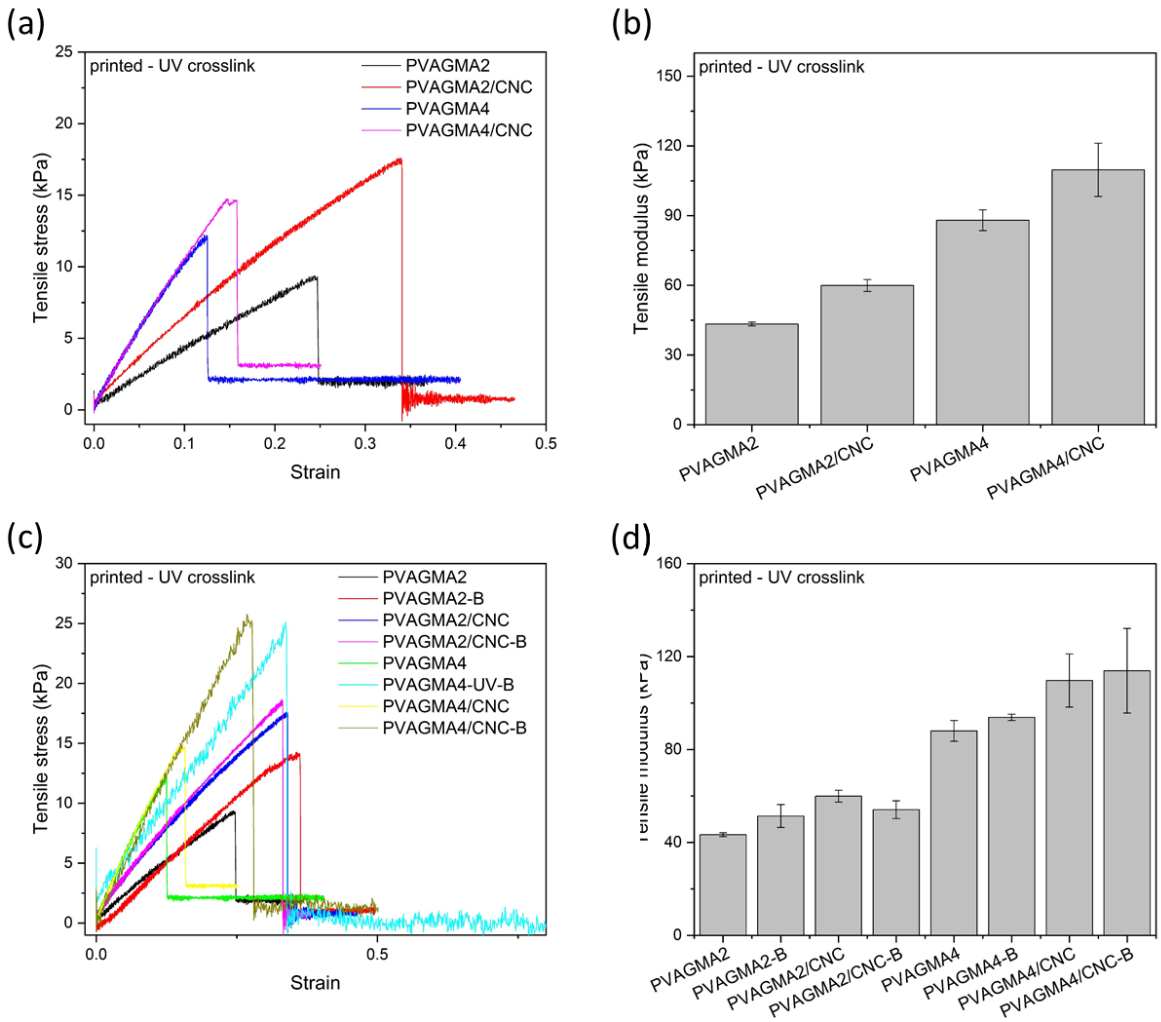

Figure 4.8 Mechanical characterization of printed pure PVAGMA2 and PVAGMA4 and hybrid PVAGMA2/CNC and PVAGMA4/CNC hydrogels. (a) Tensile stress-strain curves and (b) tensile moduli of molded UV-crosslinked hydrogels. (c) Tensile stress-strain curves and (d) tensile moduli of molded

hydrogels with a DOS of 2% and 4% with or without secondary borax crosslinking. (B in ink formlations is short for borax crosslinking.)

Cyclic loading tests were conducted to assess the mechanical stability of the polymeric network, which is vital to the application of hydrogels as vascular substitutes. The circumferential strain and strain rates of a normal carotid artery are in the range of 0.61% to 11% and 0.06 to 1.02 1/s, respectively.[159,217] Therefore, constant 10% strain was chosen for the cyclic loading tests. **Figure 4.9** shows representative cyclic tensile loadings on molded and printed dog bone-shaped samples made of pure PVAGMA2 and hybrid PVAGMA2/CNC hydrogels. As illustrated in **Figure 4.9a**, the stress-strain curves of the molded pristine PVAGMA2 overlapped (i.e. no hysteresis) while a small shift of the curves was observed in hybrid PVAGMA2/CNC hydrogels. This suggests that the elongation did not break the covalent crosslinking between PVAGMA chains and the incorporation of CNCs induces slight energy dissociation with no significant irrecoverable damage on the hydrogel network. Such hysteresis can be ascribed to the disintegration of hydrogen bonds between PVAGMA and CNC network from interfacial friction.[218] The addition of CNCs introduces interfacial interactions, such as H-bonding, that act as sacrificial bonds to limit the movement of PVAGMA chains. In the loading step, the coiled polymer chains start to elongate extensively and the rigid CNCs dissipate crack energy. When the stress is released, the flexible PVAGMA polymer chains move faster than CNC nanorods, causing internal friction and dissipating a certain amount of energy.[219,220] It was also observed that the additional borax crosslinking caused hysteresis (**Figure 4.9b**). Since the dissipated energy reflects the degree of freedom of the polymer chain movement, reversible didiol-borax complexation dissipated energy when the polymer network was stretched. It can be seen from **Figure 4.9c** that a relatively

wide hysteresis loop appeared in the 1st loading-unloading cycle of the embedded printed hydrogels and the width of the hysteresis loops reduced as cycles of loading-unloading increased in both PVAGMA2 and PVAGMA2/CNC hydrogels. The hydrogels became softer after the first loading cycle and then the moduli remained the same during the subsequent cycles. The main reasons for the significant hysteresis loop in the printed samples are the layer-by-layer fabrication strategy and relaxation effect of polymer chains, causing the loss of energy.[221] The cyclic tensile loading causes the internal damage of the polymeric network. Furthermore, the stress-strain curves shifted down slightly only after first cycle, which could be explained by the slow recovery of the samples after the initial stretch. Interestingly, the hysteresis behavior was less obvious and the mechanical properties, both elastic modulus and tensile stress, did not change significantly with the addition of CNCs and secondary borax crosslinking (**Figure 4.9d**).

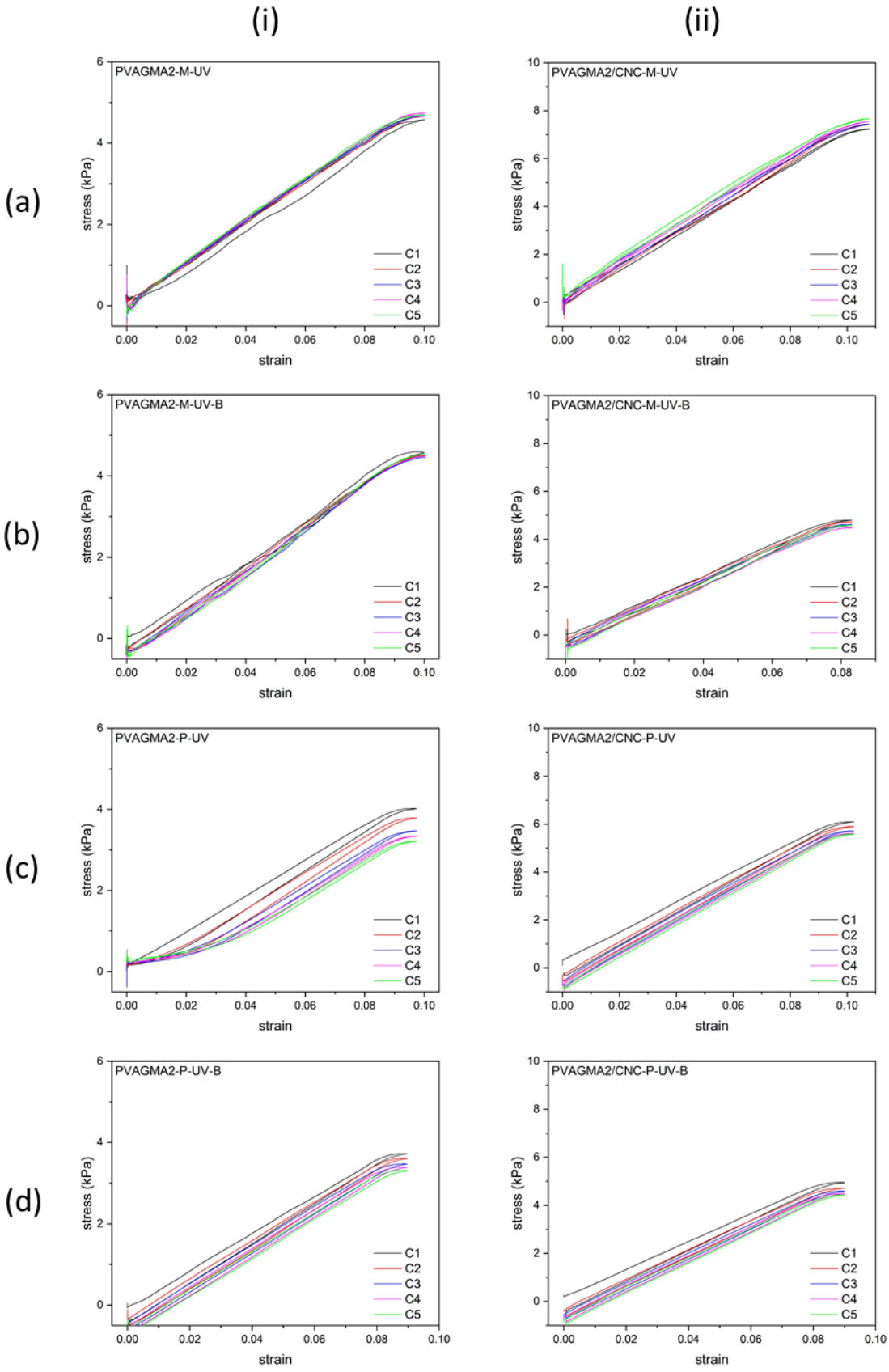

Figure 4.9 Representative cyclic tensile stress-strain curves under a continuous 5 tensile cycle tests

for (i) PVAGMA2 and (ii) PVAGMA2/CNC hydrogels with different preparation methods: (a) molded and UV-crosslinked (PVAGMA-M-UV), (b) molded and dual-crosslinked (PVAGMA-M-UV-B), (c) printed and UV-crosslinked (PVAGMA-P-UV), and (d) printed and dual-crosslinked (PVAGMA-P-UV-B).

Same cyclic loading behaviors were observed in PVAGMA4-containing hydrogels as shown in **Figure 4.10**. The results demonstrate that the small degree of strain did not influence the mechanical properties of the embedded printed dual-crosslinked PVAGMA4/CNC hydrogels such that they are strong enough to withstand the load and possess good recovery property. In combination with the swelling data, the PVAGMA2/CNC and PVAGMA4/CNC hydrogels with secondary borax crosslinking can be used to fabricate soft structures with excellent mechanical integrity.

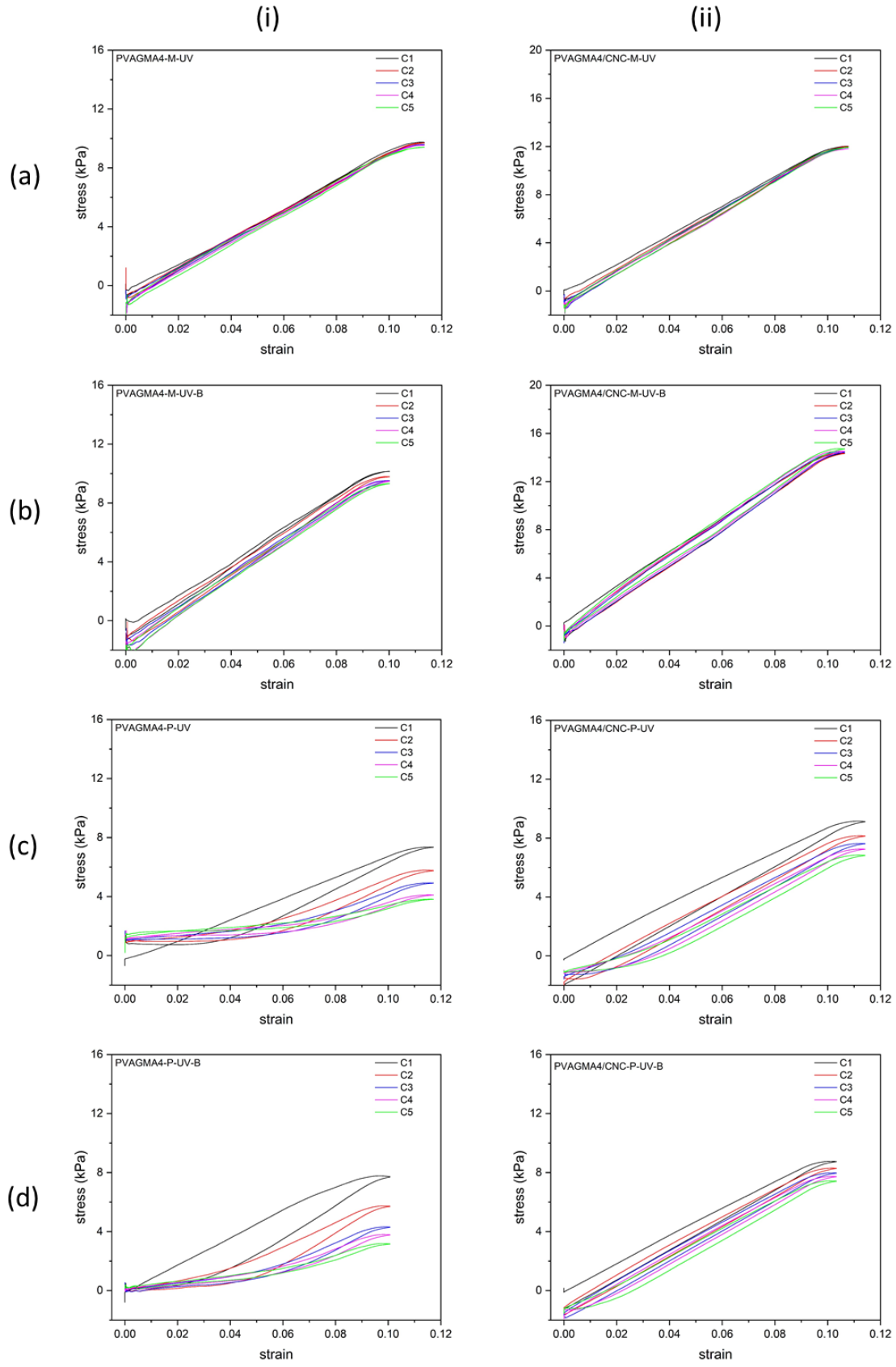

Figure 4.10 Representative cyclic tensile stress-strain curves under a continuous 5 tensile cycle tests

for (i) PVAGMA4 and (ii) PVAGMA4/CNC hydrogels with different preparation methods: (a) molded and UV-crosslinked (PVAGMA-M-UV), (b) molded and dual-crosslinked (PVAGMA-M-UV-B), (c) printed and UV-crosslinked (PVAGMA-P-UV), and (d) printed and dual-crosslinked (PVAGMA-P-UV-B).

4.3.5 Ink Printability and Granular Supporting Bath Versatility

In principle, the precision and stability of embedded printed construct is not dominated by the rheological properties of the inks.[30] To evaluate the versatility of the supporting material and inks for printing high aspect ratio constructs, PVAGMA2 that possessed relatively low viscosity and modulus compared to other composites was used as the printing ink. Several structures with different dimensions were designed and printed in 5 mg/mL borax-supplemented ALG-XG as shown in **Figure 4.11**. The additional low concentration of borax in the supporting bath is anticipated to promote *in-situ* PVAGMA crosslinking during printing and better maintain the printed geometry. A needle-like nozzle moved through the granular supporting bath with little mechanical resistance (around 5 Pa yield stress), and the inks were extruded through the needle and deposited in the desired position layer-by-layer (**Figure 4.11a**). Spiral structure was initially printed to determine the printing parameters, particularly pneumatic pressure, based on the measured diameter of the extruded filaments. A simple human-mimetic carotid bifurcation model and a carotid artery phantom with eccentric stenosis were printed in the supporting bath as shown in **Figure 4.11 b-i**, and *in-situ* UV crosslinking was employed to further help sustain the structure fidelity. Without *in-situ* UV crosslinking, the extruded inks sank due to gravity, thus decreasing the structure resolution (**Appendix B**). The models were further crosslinked after printing and removed from the supporting bath by immersing into a water bath. Moreover, patency of the models was demonstrated by perfusing the

constructs with red dye as illustrated in **Figure 4.11 e & i**, suggesting freestanding objects with microscopic structural details made from mono-material can be easily achieved in the granular supporting bath. To demonstrate the feasibility and the ease of multi-material printing, we created a dual-syringe system (**Appendix A**) and printed multi-segment hollow tube models (**Figure 4.11 j-m**). After removing the granular gel, models showed great strength and structural integrity (**Figure 4.11m**). Based on both the rheological results and the printed models, the soft granular gel permits the needle movement because the jamming/unjamming transition occurs on site and the printed structures are trapped in the location during extrusion in the supporting bath. The combination of both highly controlled, stable, precise printing process and *in-situ* UV crosslinking enable the production of precisely hierarchical structures. Overall, the printing results elucidated the great potential of the PVAGMA-based inks and the granular supporting material for embedded printing complicated 3D constructs.

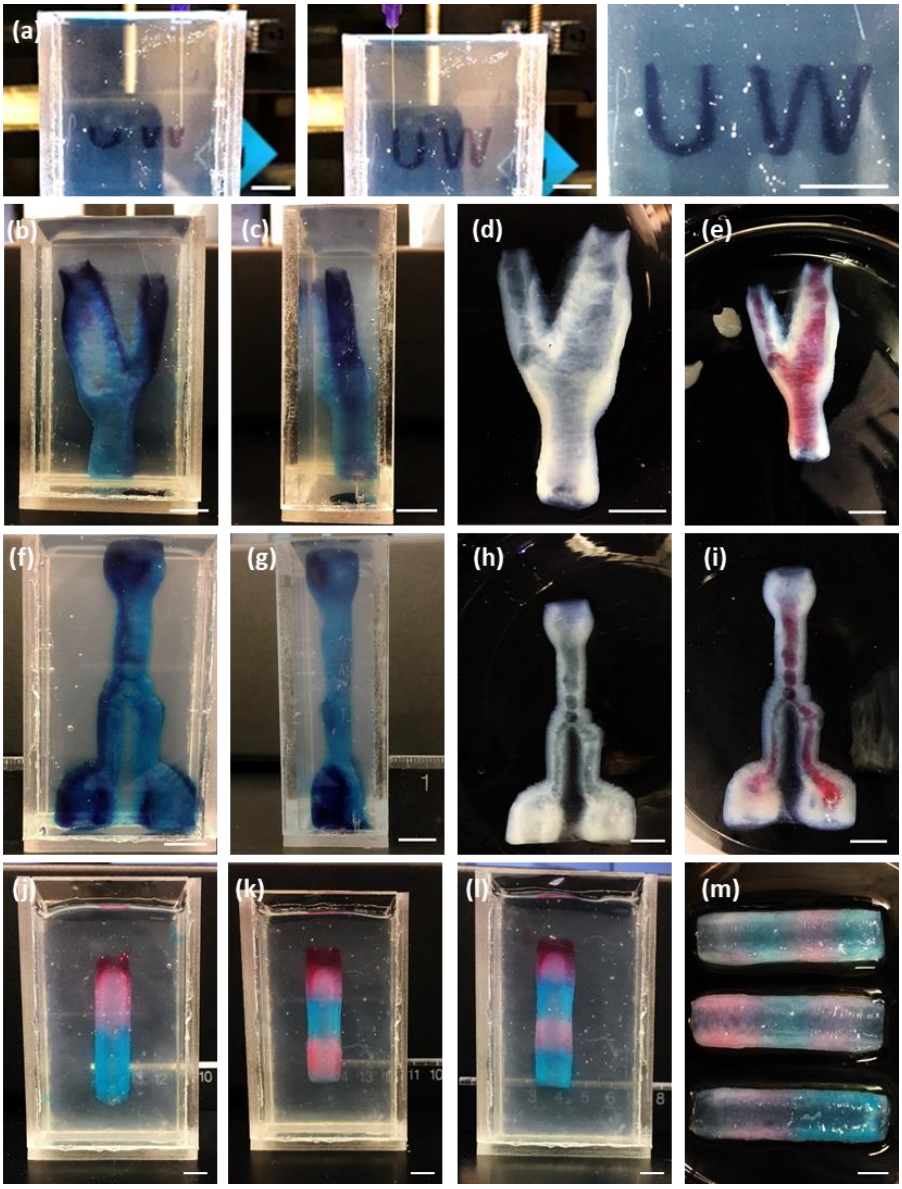

Figure 4.11 Printability of the ink and the versatility of the supporting bath material. (a) Images of letters “UW” embedded printed in ALG-XG. (b)The front and (c) side views of a carotid bifurcation structure as-printed inside the supporting bath, (d) after crosslinking and extraction, and (e) after red dye was injected through the structure. (f) The front and (g) side views of a carotid artery construct with a stenosis narrowing within ALG-XG. (h) The crosslinked construct was extracted and (i) perfused with red dye to detect the interconnectivity. (j) Two-segment, (k) three-segment, and (l) four-segment hollow tubes were printed inside ALG-XG with a customized dual-syringe printing setup. (m) The

printed tubes were crosslinked and extracted from the supporting bath, showing optimal structural integrity. Scale bars: 1 cm.

4.3.6 *In-vitro* Hemodynamic Study of Printed Vessels

To investigate the functional characteristics of the printed vasculatures, straight vessel models were assembled into a blood perfusion simulator, driven by a flow pump (**Figure 4.1b**). To connect to the pump, the printed vessels must form strong bonds with the Tygon tubings that are attached to the pump inlet/outlet. The design was inspired by the hydrogel-tissue adhesion.[212,222,223] An acrylic double-side tape was rolled at the end of the Tygon tubings, and a bridging polymer composed of polyallylamine (PAA) and coupling reagents, EDC and NHS, in MES buffer solution was applied on top. PAA is positively charged due to the primary amine groups under physiological conditions. It has been found PAA can lead to adhesion energies larger than 1000 Jm^{-2}.[212] The bridging polymer penetrated into the acrylic tape and the printed vessels, forming physical entanglement. Additionally, the positively charged bridging polymer can be absorbed to the printed vessel via electrostatic attractions. Furthermore, the primary amine groups covalently bond with the carboxylic acid groups in the printed vessel (CNCs) and acrylic double-side tapes. The adhesion energy increases and reaches plateau after 1 hour when pressure is applied on it.[222]

During the blood perfusion, the vasculature experienced circumferential tension and shear stress as illustrated in **Figure 4.12a**. It has been found that rupture was not caused by the layer-by-layer printing strategy (**Appendix B**). **Figure 4.12b** illustrates the burst pressure of the two different vessels with a diameter of 7 mm and wall thickness of 2.5 mm. The burst pressure of PVAGMA2/CNC (tensile modulus ~60 kPa) and PVAGMA4/CNC (tensile modulus ~114 kPa) vessels was 94.28 and 92.72 mmHg,

respectively, within the range of native healthy vessels, which is between 80 and 120 mmHg.[217] The wall rupture tensile stress calculated through Laplace's equation was 17.60 ± 0.79 kPa for PVAGMA2/CNC hydrogels and 17.31 ± 1.55 kPa for PVAGMA4/CNC hydrogels. The results were consistent with the tensile stress measured under uniaxial test that was 17.43 ± 2.34 kPa for PVAGMGA2/CNC and 14.30 ± 3.16 kPa for PVAGAM4/CNC, further demonstrating that the mechanical strength of the printed constructs was not influenced by the printing direction. Furthermore, it was found that both PVAGMA2/CNC and PVAGMA4/CNC vessels were able to withstand the 27 mL/s flow rate, thus a carotid pulse-mimetic pulsatile flow (60 beats/min with a peak flow rate of 27 mL/s) was selected for the durability and stability tests of the printed vessels. The vasculature phantoms were easily perfused with water for 10 days without any rupture, indicating their great stability and durability. Based on Poiseuille's equation under laminar flow, the maximum shear stress at wall was approximately 7.14 dyn cm^{-2}. The results are in the range of shear stress in microcirculation which is between 5 and 12 dyn cm^{-2}.[161]

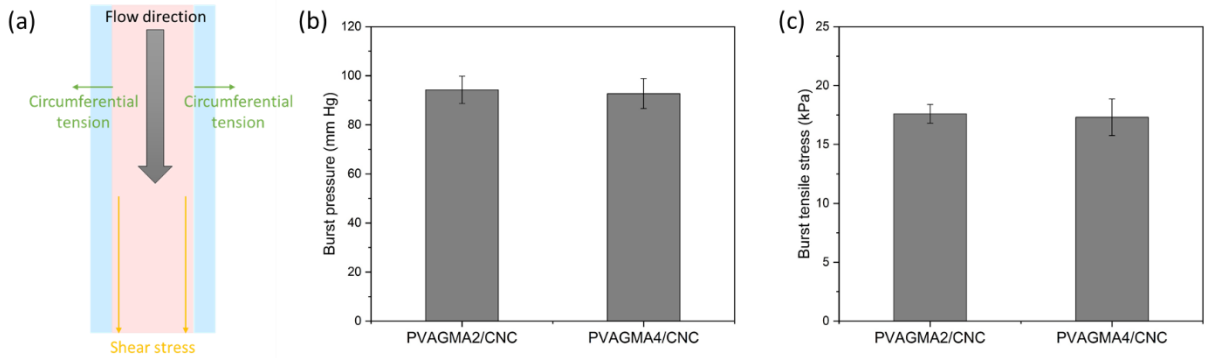

Figure 4.12 *In-vitro* hemodynamic characterizations of printed vessels. (a) Schematic illustration of circumferential tension and shear stress experienced by vascular walls during perfusion. (b) The burst pressure and (c) wall burst tensile stress of the two different 3D printed vessel lumens.

4.3.7 Ultrasound Imaging Analysis

To assess whether our vessel constructs could serve as a platform for the development of next-generation medical ultrasound technology, ultrasound imaging experiments were performed on the printed vessels. As characterized, the acoustic properties of both the vessel phantoms and tissue-mimetic slab were similar to that of human arteries and tissues. Particularly, the speed of sound was 1493 $\pm$ 2 m/s for both PVAGMA2/CNC and PVAGMA4/CNC. The attenuation coefficients of the aforementioned gels were measured to be 0.155 and 0.135 dB/cm at 5 MHz, respectively. Additionally, the elastic modulus of tissue-mimic (10% gelatin) was found to be 26.30 $\pm$ 7.19 kPa. **Figure 4.13a** shows B-mode images of the non-pressurized vessel phantoms. In all three different vessel phantoms, the vessel walls appeared homogenous despite of the three-segment vessel, suggesting the two different materials have comparable acoustic properties. The lumen diameters in soft PVAGMA2/CNC vessel (tensile modulus ~60 kPa) and stiff PVAGMA4/CNC vessel (tensile modulus ~114 kPa) were measured to be 5.71 and 7.38 mm, respectively. It can be observed that the lumen diameter of the lesion segment (6.07 mm, 114 kPa) was relatively smaller than that of the flank segments (8.12 mm, 60 kPa) whereas the wall of the lesion regions (4.16 mm) was thicker than that of the flank region (3.01 mm). Carotid pulsatile flows with a peak flow rate at 15 mL/s and 27 mL/s were applied on the three vessel phantoms and B-mode images of the phantoms at the peak flow are shown in **Figure 4.13 b-c**. **Figure 4.14** illustrates the corresponding peak vessel strain for the three vessel phantoms at 15 mL/s and 27 mL/s flow rates. The vessel strain for PVAGMA2/CNC and PVAGMA4/CNC in the single-segment vessels under pulsatile flows with a peak flow rate of 15 mL/s was found to be 18.5% and 6.5%, respectively. This value decreased to 12.4% and 3.8% in the three-segment vessel (**Figure 4.14a**).

When the peak flow rate increased to 27 mL/s, the vessel strain increased but with the same trend of that under 15 mL/s peak flow as shown in **Figure 4.14b**. The decreased vessel strain in single-segment vessel made of PVAGMA4/CNC is caused by the higher stiffness compared to that of PVAGMA2/CNC, and the lowered strain in the three-segment vessel phantom is ascribe from the thicker wall and the hysteresis of the transition between the two different compositions. Additionally, our experimental results are consistent with the finding that the vessel strain within carotid plaque ranges from 3.2% to 5.2% whereas the value for healthy carotid artery is slightly higher in the range of 5.6% and 11.0%,[155] indicating that our inks could be a good candidate for creating the vessel disease models. Furthermore, according to the finding that vessel strain was evidently reduced for higher wall thickness and stiffness, the phantoms could serve as a testbed to estimate the local vessel stiffness based on the vessel strain. Overall, our results inferred that the embedded printing strategy could be an optimal alternative to fabricate an assessment tool to test local arterial stiffness estimation algorithms. In turn, more mature diagnostic solutions may be devised in the future to benefit vascular medicine.

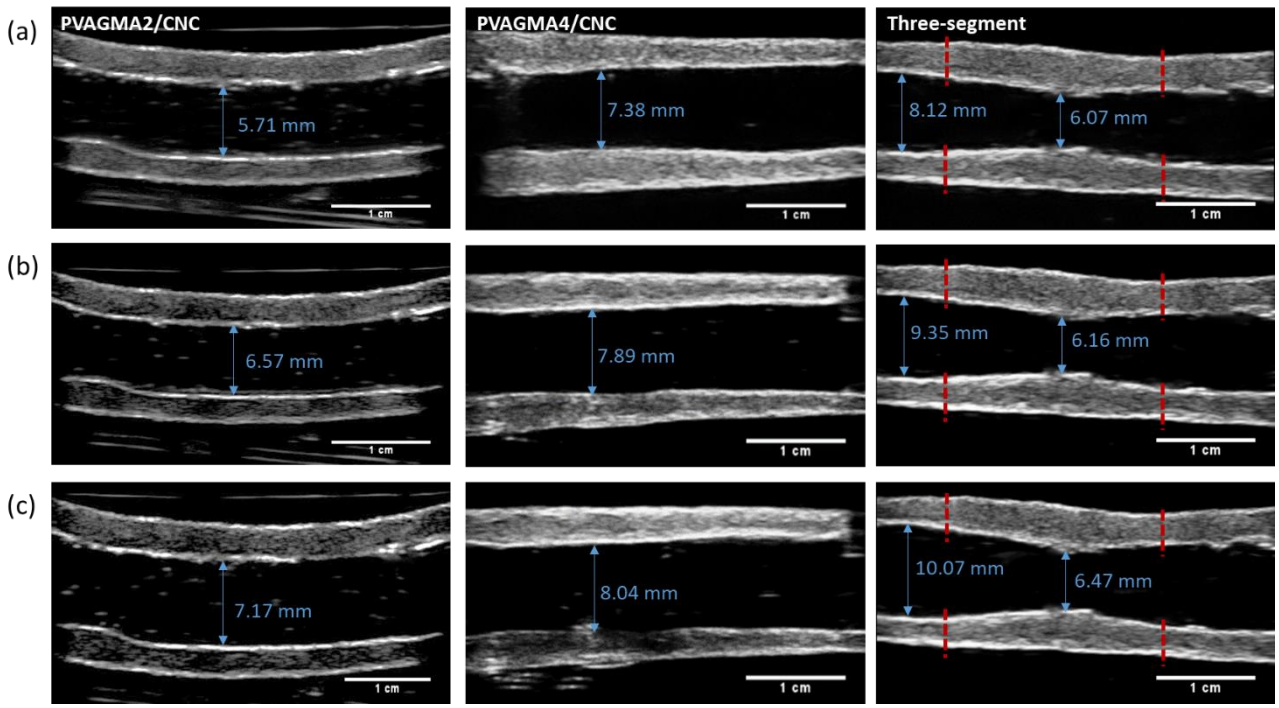

Figure 4.13 B-mode images for PVAGMA2/CNC, PVAGMA4/CNC, and three-segment vessel (borders: red dashed line) phantoms when vessel lumen was (a) not pressurized and under carotid pulse with (b) 15 mL/s peak flow rate) and (c) 27 mL/s peak flow rate.

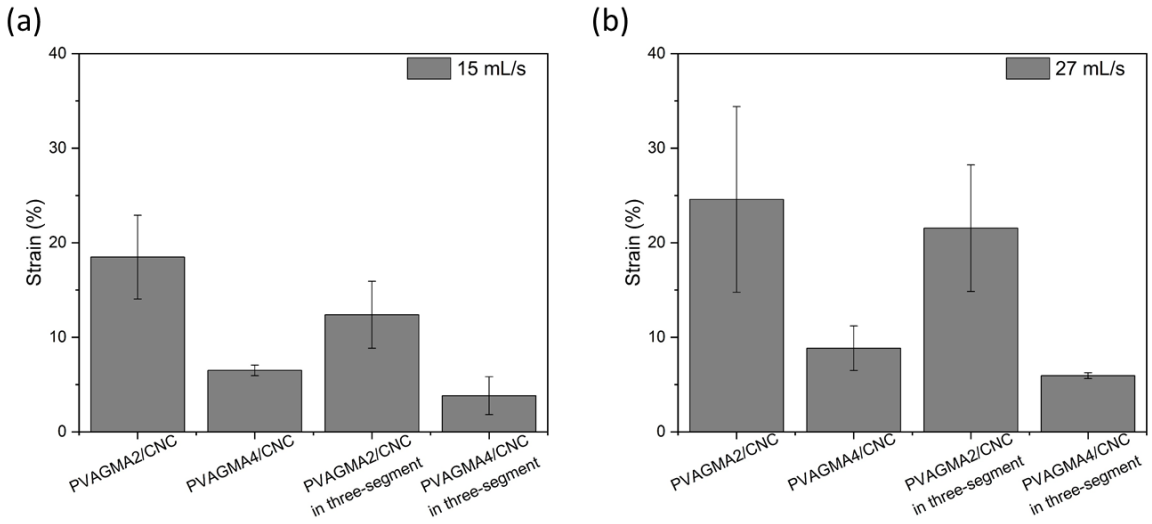

Figure 4.14 Vessel strains of the three different printed vascular phantoms when they were pulsed with carotid flow with a peak flow rate at (a) 15 mL/s and (b) 27 mL/s.

4.4 Conclusions

In this study, I report a novel ink composed of PVAGMA and CNCs and a granular supporting bath that is suitable for the embedded 3D printing. Due to the excellent Bingham property of the supporting bath, *in-situ* crosslinking strategy, and customized dual-syringe system, hierarchical constructs with high spatial resolution, structural integrity, and pattern fidelity were demonstrated via the embedded printing. By controlling the degree of substitution of PVAGMA, ink formulations, and the crosslinking methods of the inks, hydrogels with a wide range of tensile modulus from 21.80 kPa to 146.52 kPa were fabricated. The circumferential tensile stress acquired from the *in-vitro* hemodynamic study was comparable to the tensile stress obtained under uniaxial test. Since the swelling ratios of the hydrogels along and perpendicular to the printing direction were similar, it demonstrated that the mechanical strength were not affected by the printing direction. Cyclic loading tests and hemodynamic study show that our ink compositions, namely PVAGMA2/CNC and PVAGMA4/CNC, possessed great stability and durability which was confirmed by continuously pulsatile flowing for over 10 days without rupture. Additionally, the burst pressure of the bioink materials was comparable to the native carotid arteries, making them ideal biomaterials for the fabrication of artificial vessels. The novel acoustic property of PVA and CNC allowed us to visualize the printed vessel movement under carotid pulse-mimetic pulsatile flows via ultrasound imaging. The vessel strain of the soft PVAGMA2/CNC vessels (tensile modulus ~60 kPa) and stiff PVAGMA4/CNC vessels (tensile modulus ~114 kPa) was found to be 24.6% and 8.9%, respectively, indicating that the two bioink materials could be good candidates for the healthy and diseased arterial vessel-mimetic materials. Overall, our results elucidated the great potential of the PVAGMA-based inks and granular

supporting material to create functional heterogeneous tissue models via embedded printing strategy for regenerative medicine and tissue engineering applications.

Chapter 5 Conclusions and Future Work

5.1 Conclusions

Engineered tissue with adjustable biochemical and physical properties are required to closely mimic the human body environment to enable the study of cell behavior *in vitro* and allow the fabrication of artificial tissue constructs for the applications in regenerative medicine and tissue engineering. As such, extrusion-based 3D bioprinting has evolved with a great potential to generate complex tissue-mimetic constructs. Despite its advances, fabricating accurate and precise human-mimetic functional 3D constructs, however, remains challenging. The major issues include the need to develop biocompatible ink materials, recapitulate complex tissue, select suitable cell sources, and increase scalability while reduce the manufacturing time. As the bioink materials are of paramount importance that regulates cell functions and affects printability, structure resolution, and shape fidelity, this thesis was aimed to develop various printable bioink materials and investigate the influence of material properties on printing processes and cell behavior. Liver lobule and vessel structures were selected as the investigation models. Currently, micro-scale liver-mimetic tissue have been generated for cancer research and drug screening. However, few were working on fabricating liver lobule-mimetic constructs with cells deposited in defined regions, therefore, I aim to directly print liver lobule-mimetic cell-laden and acellular architectures to investigate the versatility of our developed bioink. Further, current studies on 3D printing vasculature focus on the perfusion test while neglecting the important mechanical properties, especially the effect of vessel morphology on blood flow. Additionally, these vascular phantoms are highly desirable calibration tools and training

platforms to develop next-generation medical ultrasound technologies and explore cardiovascular disease mechanisms.

In **Chapter 3**, I discussed the development of various alginate/CNC-based bioinks suitable for the ME printing of liver lobule-mimetic constructs. Despite the excellent rheological properties of the pre-gel solution and highly porous microstructure of the hydrogel, cell growth was limited. To circumvent such issues, GelMA that contains cell-binding sites was incorporated to improve cell behaviors. The second version hybrid bioink (135ACG) exhibited excellent shear-thinning and solid-like properties as well, leading to high printability without cell damage. Honeycombs with a height up to 3.4 mm was successfully ME printed. The UV crosslinked stiff 135ACG hydrogel possessed a compressive modulus on the order of 10 kPa, allowing fibroblast adhesion, spreading, and proliferation. By controlling the degree of substitution and polymer concentration, 4 wt% GelMA bioink was designed to encapsulate hepG2 cells, as the GelMA hydrogel possessed a compressive modulus of approximately 2.5 kPa which is comparable to the native liver tissue. Four different versions of to-scale liver lobule-mimetic constructs with precise placement of hepG2 cells and fibroblasts embedded in matching ECMs were fabricated via ME bioprinting, allowing us to investigate the influence of mechanical cues and intercellular interactions on cell behaviors, such as hepatic spheroid formation, cell alignment, migration at the boundaries of stiff/soft ECMs, and albumin production. Interestingly, fibroblasts thrived in stiff 135ACG matrices and aligned at the 135ACG-GelMA boundary due to durotaxis, while hepG2 cells formed spheroids exclusively in the soft GelMA matrix. Hepatic spheroids formed by a homogenous mixture of hepG2/fibroblasts were found to be smaller than those formed by hepG2 only. Enhanced albumin secretion was observed in the bicellular co-culture system, both with and

without direct intercellular contact, suggesting that improved hepatic function is ascribed to the soluble chemical factors produced by fibroblasts.

In **Chapter 4**, I presented a granular supporting bath-based, embedded 3D printing strategy to fabricate hierarchical architectures. Due to the excellent Bingham property of the supporting bath consisting of microparticle alginate and xanthan gum, *in-situ* crosslinking, and customized dual-syringe system, high aspect ratio constructs with high spatial resolution, structural integrity, and shape fidelity were achieved. A series of novel ink composed of PVAGMA and CNCs with strong shear-thinning properties were developed. By controlling the degree of substitution of PVAGMA, ink formulations, and the crosslinking methods of the inks, hydrogels with wide range of tensile moduli ranging from 21.80 kPa to 146.52 kPa were fabricated and can be used to recapitulate healthy arteries and diseased arteries. The circumferential tensile stress of PVAGMA2/CNC and PVAGMA4/CNC acquired from the *in-vitro* hemodynamic study was comparable to the tensile stress obtained under uniaxial test. Since the swelling ratio of the hydrogels along and perpendicular to the printing direction are similar, it demonstrated that the mechanical strength was not affected by the printing direction and optical layer integrity was achieved. Cyclic loading and hemodynamic study were performed on the PVAGMA2/CNC and PVAGMA4/CNC hydrogels, showing that our ink compositions possessed great mechanical stability, durability, and recovery, which were further confirmed by continuously flowing water with a carotid pulse-mimetic pulsatile flow (60 beats/min with a peak flow rate of 27 mL/s) for over 10 days without rupture. Additionally, the burst pressure of the bioink materials was similar to the native carotid artery, making them ideal biomaterials for the fabrication of artificial vessels. The novel acoustic property of PVA also allowed us to visualize the printed vessel

movement under carotid pulse-mimetic pulsatile flows via ultrasound imaging. B-mode imaging confirmed the vessel dimensions, and the vessel strain of the softer PVAGMA2/CNC and stiffer PVAGMA4/CNC was found to be 24.6% and 8.9%, respectively, indicating that the two bioink materials could be good candidates for healthy and diseased artery vessel-mimetic materials. Overall, our results elucidated the great potential of the PVAGMA-based inks and granular supporting material to create functional heterogeneous vasculature via an embedded printing strategy for regenerative medicine and tissue engineering applications.

In summary, this thesis investigated the development of the bioink materials to ensure high shape resolution and cell viability and function. Our results demonstrated the great potential of the bioink materials and ME-based freeform and embedded printing methods developed in this study, which offer new strategies to address the central challenge in tissue engineering to create complex constructs with multiple cell types and varying ECMs to recapitulate biological functions.

5.2 Future Work

Based on the literature review and the achievements from this thesis, recommendations for future research are proposed.

1. Cells are sensitive to the local environment of the ECM, including stiffness, surface charge, and topology. In this thesis, we focused on the mechanical property of the developed bioink materials to mimic real tissue rather than investigating surface charge and geometry of the biomaterials. Therefore, the effect of surface charge and topology of biomaterials on cell behaviors should be investigated in the next step. (1) The cell membrane possesses a negative charge with an electric

potential ranging from -10 to -90 mV, thus the electrostatic interaction between cells and matrix plays an important role in regulating cell behavior, including cell adhesion, proliferation, differentiation, and spreading. Additionally, the surface charge affects the protein adsorption due to the amphoteric nature of protein and thus the associated cell adhesion.[224] Our preliminary results on the modification of CNCs are shown in **Appendix C**. Less negatively-charged and positively-charged CNC were prepared to compare with pure CNC. It was found that the surface modification influenced the rheological property of the nanomaterial and the cell growth as well. Fibroblasts elongated and proliferated in the pure CNC and the less negatively-charged CNC (DS-CNC)-containing hybrid bioinks, whereas cells exhibited round morphology in the positively-charged CNC (GTMAC-CNC) bioink. In addition, the cell proliferation rate and cell size were larger in the DS-CNC bioink compared to the CNC bioink, which was caused by the less negative charge of DS-CNC. However, cells cultured in GTMAC-CNC-containing bioink exhibited lower cell viability, which may be caused by the impurity of GTMAC-CNC. Another assumption is that the overly high positive charge may damage cells, but needs to be confirmed with future study. (2) The ECM is composed of a network of fibrous proteins and glycosaminoglycans *in vivo*. The fibrillar structure of ECM influences the physical properties, growth factor signalling, the structural anisotropy, and physical properties, thus influencing the cell growth, migration, and differentiation.[45] ECM anisotropy is necessary to guide the alignment of cells in many tissues, such as cardiac and muscle tissues,[45] hence fibrillar biomaterials should be incorporated in the bioink materials. Preliminary results on cellulose nanofibers (CNF) were illustrated in **Appendix C**. Although a higher cell proliferation rate and cell size were observed in the CNF-incorporated bioink when compared to

the CNC-incorporated bioink, the needle (ID. 100 μm) was easily clogged due to the large dimensions of the CNFs, limiting its application in printing tiny constructs. In the future, CNF with different dimensions should be investigated to develop an optimal fibrillar bioink material that can be utilized to print multi-scale constructs. Furthermore, as structural anisotropy plays a crucial role in modulating cell behaviors, anisotropic hydrogels should be generated. This can be realized by applying shear, electric, or magnetic fields depending on the material properties followed by chemical or physical crosslinking.[225] When the bioink is extruded through the needles, shear stress is applied on the materials thus aligning the orientation of nanofillers. In this thesis, GelMA, a thermoresponsive polymer, was the main component of the bioink, thus it is anticipated that lowering the temperature of printing substrate or supporting bath to 4 ℃ will trap the nanofillers in the hydrogels, making the hydrogel anisotropic. In addition, as photosensitive polymers were the main polymers in our research, *in-situ* UV crosslinking may help fix the nanofiller as well.

2. Although the feasibility of the embedded printing presented in this thesis has been proved for the fabrication of large-scale architectures, the structural resolution of the printed structures was not able to reach the same size as the inner diameter of the needles. One major reason is the limiting property of the supporting bath materials. To overcome this, a supporting bath composed of a small, uniform microparticles with a strong modulus and low yield stress should be developed for producing hierarchical constructs. In addition, two snake-eye UV lights were used to induce *in-situ* crosslinking, thus only crosslinking two sides of the printed structures facing the UV light while the other regions tended to sediment and deform during printing. It is

suggested that a UV light chamber is equipped with the 3D printer, allowing all-round crosslinking during printing and preventing structure deformation due to gravity. Besides the materials science and setup of the printing strategy, the biological properties also need to be investigated. Cytotoxicity should be first conducted to confirm the biocompatibility of the supporting bath material. Furthermore, since embedded printing large-scale constructs takes time, cell viability should be investigated, especially within the initial layers of the large-scale constructs. To maintain high cell viability, a cell medium should be used to replace water or PBS in both supporting bath and bioinks, and the supporting bath may be contained in a temperature control setup to keep the temperature at 37 ℃ during printing.

3. The present study (**Chapter 4**) has proven the hemodynamic performance of the vessel phantoms and promising applications in ultrasonics, however, only simple structures were printed, therefore more complex models should be devised and printed including (1) carotid artery bifurcations with various levels of arterial stenosis developed by the same or different vessel wall stiffness, (2) heterogeneous vascular constructs with two layers of different elasticity, and (3) tortuous vascular structures based on patient's information. Cell-laden vascular phantoms and the gas and molecule permeability of the printed vessels should also be investigated. Vessel tubes should be fabricated by multi-material bioprinting to mimic the stiffer intima-media complex (inner layer) of an artery relative to the adventitia (outer layer). Moving forward with vessel permeability tests and *in vitro* cell studies, such as cell viability, proliferation, and growth, the more challenging problem is to fabricate biomimetic diseased vascular phantoms to support the research on ultrasound diagnostics. It is proposed that a thrombus phantom will be developed

by the following three steps: (i) fibroblast-laden bioinks will be extruded directly into the supporting bath to create non-endothelialized, damaged vessel-mimicking microchannels; (ii) human blood will be infused into the microchannels followed by adding calcium chloride to induce clotting; (iii) the phantom will be cultured in an incubator to foster fibrotic clot formation through fibroblast migration into the microchannels. Additionally, atherosclerosis phantoms with intraplaque neovascularization should be designed. Endothelialized monolayer should be fabricated by culturing endothelial cells within the channel and the endothelial cells should be biochemically induced to express high levels of cell adhesion molecules to mimic inflammation. These endothelialized microchannels should be encapsulated within a plaque mimicking slab that is in turn implanted onto the inner wall of a vessel-mimicking tube.

4. Besides liver lobules and carotid artery structures, other models, such as heart aortic valve and cartilage, can be printed in the future. Based on the property of various tissues, future studies should still focus on the development of the bioink materials. For instance, conductive nanofillers should be incorporated to introduce the electrical conductivity to the cardiac matrix. Additionally, G-codes generated from the slicing software have some limitations in the defined print paths. For instance, when a ring structure needs to be printed, it prints the perimeter (the outer shell) and the loops (the inner shell) followed by filling the inner regions. However, the infilling process makes some parts of the ring structure much thicker than others, making the printed ring structure inhomogeneous. Therefore, efforts should be devoted to formulating algorithms that can generate desired print paths to increase shape resolution.

References

1. Selcan Gungor-Ozkerim, P., Inci, I., Zhang, Y. S., Khademhosseini, A. & Dokmeci, M. R. Bioinks for 3D bioprinting: an overview. *Biomater. Sci.* **6**, 915–946 (2018).

2. Armstrong, J. P. K., Burke, M., Carter, B. M., Davis, S. A. & Perriman, A. W. 3D bioprinting using a templated porous bioink. *Adv. Healthc. Mater.* **5**, 1724–1730 (2016).

3. Guvendiren, M., Molde, J., Soares, R. M. D. & Kohn, J. Designing biomaterials for 3D printing. *ACS Biomater. Sci. Eng.* **2**, 1678–1683 (2016).

4. Fedorovich, N. E. *et al.* Hydrogels as extracellular matrices for skeletal tissue engineering: state-of-the-art and novel application in organ printing. *Tissue Eng.* **13**, 1905–1925 (2007).

5. Gross, B. C., Erkal, J. L., Lockwood, S. Y., Chen, C. & Spence, D. M. Evaluation of 3D printing and its potential impact on biotechnology and the chemical sciences. *Anal. Chem.* **86**, 3240–3253 (2014).

6. Berman, B., Zarb, F. G. & Hall, W. 3-D printing: The new industrial revolution. *Bus. Horiz.* **55**, 155–162 (2012).

7. Murphy, S. V., De Coppi, P. & Atala, A. Opportunities and challenges of translational 3D bioprinting. *Nat. Biomed. Eng.* **4**, 370–380 (2020).

8. Gibson, I. & Rosen, D. *Additive Manufacturing Technologies*. (Springer, 2015).

9. Gao, G., Kim, B. S., Jang, J. & Cho, D.-W. Recent Strategies in Extrusion-Based Three-Dimensional Cell Printing toward Organ Biofabrication. *ACS Biomater. Sci. Eng.* **5**, 1150–1169 (2019).

10. Kang, H.-W. *et al.* A 3D bioprinting system to produce human-scale tissue constructs with structural integrity. *Nat. Biotechnol.* **34**, 312–319 (2016).

11. Mazzocchi, A., Devarasetty, M., Huntwork, R., Soker, S. & Skardal, A. Optimization of collagen type I-hyaluronan hybrid bioink for 3D bioprinted liver microenvironments. *Biofabrication* **11**, 015003 (2018).

12. Isaacson, A., Swioklo, S. & Connon, C. J. 3D bioprinting of a corneal stroma equivalent. *Exp. Eye Res.* **173**, 188–193 (2018).

13. Skylar-Scott, M. A., Mueller, J., Visser, C. W. & Lewis, J. A. Voxelated soft matter via multimaterial multinozzle 3D printing. *Nature* **575**, 330–335 (2019).

14. Krishtul, S., Baruch, L. & Machluf, M. Processed Tissue–Derived Extracellular Matrices: Tailored Platforms Empowering Diverse Therapeutic Applications. *Adv. Funct. Mater.* 1900386 (2019). doi:10.1002/adfm.201900386

15. Liu, W. *et al.* Extrusion Bioprinting of Shear-Thinning Gelatin Methacryloyl Bioinks. *Adv. Healthc. Mater.* **6**, 1601451 (2017).

16. Guvendiren, M., Molde, J., Soares, R. M. D. & Kohn, J. Designing biomaterials for 3D printing. *ACS Biomater. Sci. Eng.* acsbiomaterials.6b00121 (2016). doi:10.1021/acsbiomaterials.6b00121

17. Jang, J., Yi, H. & Cho, D. 3D printed tissue models: present and future. *ACS Biomater. Sci. Eng.* **2**, 1722–1731 (2016).

18. Billiet, T., Vandenhaute, M., Schelfhout, J., Vlierberghe, S. Van & Dubruel, P. A review of trends and limitations in hydrogel-rapid prototyping for tissue engineering. *Biomaterials* **33**, 6020–6041 (2012).

19. Wüst, S., Müller, R. & Hofmann, S. Controlled positioning of cells in biomaterials—approaches towards 3D tissue printing. *J. Funct. Biomater.* **2**, 119–154 (2011).

20. Murphy, S. V & Atala, A. 3D bioprinting of tissues and organs. *Nat. Biotechnol.* **32**, 773–785 (2014).

21. Arslan-Yildiz, A. *et al.* Towards artificial tissue models: past, present, and future of 3D bioprinting. *Biofabrication* **8**, 014103 (2016).

22. Moroni, L. *et al.* Biofabrication strategies for 3D in vitro models and regenerative medicine. *Nat. Rev. Mater.* **3**, 21–37 (2018).

23. Matai, I., Kaur, G., Seyedsalehi, A., McClinton, A. & Laurencin, C. T. Progress in 3D bioprinting technology for tissue/organ regenerative engineering. *Biomaterials* **226**, 119536 (2020).

24. Vikram Singh, A. *et al.* The Adoption of Three-Dimensional Additive Manufacturing from Biomedical Material Design to 3D Organ Printing. *Appl. Sci.* **9**, 811 (2019).

25. Miri, A. K. *et al.* Effective bioprinting resolution in tissue model fabrication. *Lab Chip* **19**, (2019).

26. Lee, A. *et al.* 3D bioprinting of collagen to rebuild components of the human heart. *Science* **365**, 482–487 (2019).

27. Mehrotra, S., Moses, J. C., Bandyopadhyay, A. & Mandal, B. B. 3D Printing/Bioprinting Based Tailoring of in Vitro Tissue Models: Recent Advances and Challenges. *ACS Appl. Bio Mater.* **2**, 1385–1405 (2019).

28. Placone, J. K. & Engler, A. J. Recent Advances in Extrusion-Based 3D Printing for Biomedical Applications. *Adv. Healthc. Mater.* **7**, 1701161 (2017).

29. O'Bryan, C. S. *et al.* Self-assembled micro-organogels for 3D printing silicone structures. *Sci.*

Adv. **3**, e1602800 (2017).

30. Bhattacharjee, T. *et al.* Writing in the granular gel medium. *Sci. Adv.* **1**, e1500655 (2015).

31. Jeon, O. *et al.* Individual cell-only bioink and photocurable supporting medium for 3D printing and generation of engineered tissues with complex geometries. *Mater. Horizons* **6**, 1625–1631 (2019).

32. Luo, G. *et al.* Freeform, Reconfigurable Embedded Printing of All-Aqueous 3D Architectures. *Adv. Mater.* **31**, 1904631 (2019).

33. Hinton, T. J. *et al.* Three-dimensional printing of complex biological structures by freeform reversible embedding of suspended hydrogels. *Sci. Adv.* **1**, e1500758 (2015).

34. Choi, Y.-J. *et al.* A 3D cell printed muscle construct with tissue-derived bioink for the treatment of volumetric muscle loss. *Biomaterials* **206**, 160–169 (2019).

35. Skylar-Scott, M. A. *et al.* Biomanufacturing of organ-specific tissues with high cellular density and embedded vascular channels. *Sci. Adv.* **5**, eaaw2459 (2019).

36. Ning, L. *et al.* Embedded 3D Bioprinting of Gelatin Methacryloyl-Based Constructs with Highly Tunable Structural Fidelity. *ACS Appl. Mater. Interfaces* acsami.0c15078 (2020). doi:10.1021/acsami.0c15078

37. Abdollahi, S., Davis, A., Miller, J. H. & Feinberg, A. W. Expert-guided optimization for 3D printing of soft and liquid materials. *PLoS One* **13**, e0194890 (2018).

38. Noor, N. *et al.* 3D Printing of Personalized Thick and Perfusable Cardiac Patches and Hearts. *Adv. Sci.* **6**, 1900344 (2019).

39. Sachlos, E. & Czernuszka, J. T. Making tissue engineering scaffolds work. Review on the application of solid freeform fabrication technology to the production of tissue engineering scaffolds. *Eur. Cells Mater.* **5**, 29–40 (2003).

40. Nerem, R. M. & Sambanis, A. Tissue engineering: from biology to biological substitutes. *Tissue Eng.* **1**, 3–13 (1995).

41. Khademhosseini, A., Langer, R., Borenstein, J. & Vacanti, J. P. Microscale technologies for tissue engineering and biology. *PNAS* **103**, 2480–2487 (2006).

42. Hutmacher, D. W., Sittinger, M. & Risbud, M. V. Scaffold-based tissue engineering: rationale for computer-aided design and solid free-form fabrication systems. *Trends Biotechnol.* **22**, 354–362 (2004).

43. Yang, S., Leong, K., Du, Z. & Chua, C. The design of scaffolds for use in tissue engineering. part I. traditional factors. *Tissue Eng.* **7**, 679–689 (2001).

44. Klaas, M. *et al.* The alterations in the extracellular matrix composition guide the repair of damaged liver tissue OPEN. *Sci. Rep.* **6**, 27398 (2016).

45. Prince, E. & Kumacheva, E. Design and applications of man-made biomimetic fibrillar hydrogels. *Nat. Rev. Mater.* **4**, 99–115 (2019).

46. Xue, D., Zhang, J., Wang, Y. & Mei, D. Digital Light Processing-Based 3D Printing of Cell-Seeding Hydrogel Scaffolds with Regionally Varied Stiffness. *ACS Biomater. Sci. Eng.* **5**, 4825–4833 (2019).

47. Berg, J. *et al.* Optimization of cell-laden bioinks for 3D bioprinting and efficient infection with influenza A virus. *Sci. Rep.* **8**, 13877 (2018).

48. Retting, K. *et al.* Modeling Liver Biology and the Tissue Response to Injury in Bioprinted Human Liver Tissues. *Appl. Vitr. Toxicol.* **4**, 288–303 (2018).

49. Billiet, T., Vandenhaute, M., Schelfhout, J., Vlierberghe, S. Van & Dubruel, P. A review of trends and limitations in hydrogel-rapid prototyping for tissue engineering. *Biomaterials* **33**, 6020–6041 (2012).

50. Tumbleston, J. R. *et al.* Continuous liquid interface production of 3D objects. *Science* **347**, 1349–1352 (2015).

51. Robert, B. *et al.* Direct-write assembly of 3D hydrogel scaffolds for guided cell growth. *Adv. Mater.* **21**, 1–4 (2009).

52. Duoss, E. B., Twardowski, M. & Lewis, J. A. Sol-gel inks for direct-write assembly of functional oxides. *Adv. Mater.* **19**, 3485–3489 (2007).

53. Lewis, J. A. Direct ink writing of 3D functional materials. *Adv. Funct. Mater.* **16**, 2193–2204 (2006).

54. Tan, Y. J., Tan, X., Yee, W., Shu, Y. & & Tor, B. Hybrid microscaffold-based 3D bioprinting of multi-cellular constructs with high compressive strength: A new biofabrication strategy. *Sci. Rep.* **6**, 39140 (2016).

55. Cem Millik, S. *et al.* 3D printed coaxial nozzles for the extrusion of hydrogel tubes toward modeling vascular endothelium. *Biofabrication* **11**, 045009 (2019).

56. Luckert, C. *et al.* Comparative analysis of 3D culture methods on human HepG2 cells. *Arch. Toxicol.* **91**, 393–406 (2017).

57. Sheikhi, A. *et al.* Microfluidic-enabled bottom-up hydrogels from annealable naturally-derived protein microbeads. *Biomaterials* **192**, 560–568 (2019).

58. Shin, S. R. *et al.* Carbon nanotube reinforced hybrid microgels as scaffold materials for cell

encapuslation. *ACS Nano* **6**, 362–372 (2012).

59. Gudapati, H., Yan, J., Huang, Y. & Chrisey, D. B. Alginate gelation-induced cell death during laser-assisted cell printing. *Biofabrication* **6**, 035022 (2014).

60. Augst, A. D., Kong, H. J. & Mooney, D. J. Alginate hydrogels as biomaterials. *Macromol. Biosci.* **6**, 623–633 (2006).

61. Gombotz, W. R. & Wee, S. F. Protein release from alginate matrices. *Adv. Drug Deliv. Rev.* **64**, 194–205 (2012).

62. Lee, C. *et al.* Bioinspired, calcium-free alginate hydrogels with tunable physical and mechanical properties and improved biocompatibility. *Biomacromolecules* **14**, 2004–2013 (2013).

63. Rastogi, P. & Kandasubramanian, B. Review of alginate-based hydrogel bioprinting for application in tissue engineering. *Biofabrication* **11**, 042001 (2019).

64. Wu, Y., Lin, Z. Y. (William), Wenger, A. C., Tam, K. C. & Tang, X. (Shirley). 3D bioprinting of liver-mimetic construct with alginate/cellulose nanocrystal hybrid bioink. *Bioprinting* **9**, 1–6 (2018).

65. Jeon, O., Bouhadir, K. H., Mansour, J. M. & Alsberg, E. Photocrosslinked alginate hydrogels with tunable biodegradation rates and mechanical properties. *Biomaterials* **30**, 2724–2734 (2009).

66. Rouillard, A. D. *et al.* Methods for photocrosslinking alginate hydrogel scaffolds with high cell viability. *Tissue Eng. Part C* **17**, 173–179 (2011).

67. Grigore, A., Sarker, B., Fabry, B., Boccaccini, A. R. & Detsch, R. Behavior of encapsulated MG-63 cells in RGD and gelatine-modified alginate hydrogels. *Tissue Eng. Part A* **20**, 2140–50 (2014).

68. Yu, C. *et al.* Scanningless and continuous 3D bioprinting of human tissues with decellularized extracellular matrix. *Biomaterials* **194**, 1–13 (2019).

69. Jia, W. *et al.* Direct 3D bioprinting of perfusable vascular constructs using a blend bioink. *Biomaterials* **106**, 58–68 (2016).

70. Chen, K. L., Mylon, S. E., Elimelech, M. & Pennsyl, V. Enhanced aggregation of alginate-coated iron oxide (Hematite) nanoparticles in the presence of calcium, strontium, and barium cations. *Langmuir* **23**, 5920–5928 (2007).

71. Yang, J., Xie, Y. & He, W. Research progress on chemical modification of alginate: A review. *Carbohydr. Polym.* **84**, 33–39 (2011).

72. Lee, K. Y. *et al.* Controlling mechanical and swelling properties of alginate hydrogels independently by cross-linker type and cross-linking density. *Macromolecules* **33**, 4291–4294 (2000).

73. Zhu, K. *et al.* A General Strategy for Extrusion Bioprinting of Bio-Macromolecular Bioinks through Alginate-Templated Dual-Stage Crosslinking. *Macromol. Biosci.* **18**, 1800127 (2018).

74. Kojima, C. *et al.* Doxorubicin-conjugated dendrimer/collagen hybrid gels for metastasis-associated drug delivery systems. *Acta Biomater.* **9**, 5673–5680 (2013).

75. Hadi, M. F., Sander, E. A., Ruberti, J. W. & Barocas, V. H. Simulated remodeling of loaded collagen networks via strain-dependent enzymatic degradation and constant-rate fiber growth. *Mech. Mater.* **44**, 72–82 (2012).

76. Yeo, M. G., Lee, J. S., Chun, W. & Kim, G. H. An innovative collagen-based cell-printing method for obtaining human adipose stem cell-laden structures consisting of core-sheath structures for tissue engineering. *Biomacromolecules* **17**, 1365–1375 (2016).

77. Drury, J. L. & Mooney, D. J. Hydrogels for tissue engineering: scaffold design variables and applications. *Biomaterials* **24**, 4337–4351 (2003).

78. Zhu, J. & Kaufman, L. J. Collagen i self-assembly: Revealing the developing structures that generate turbidity. *Biophys. J.* **106**, 1822–1831 (2014).

79. Yin, J., Yan, M., Wang, Y., Fu, J. & Suo, H. 3D Bioprinting of Low-Concentration Cell-Laden Gelatin Methacrylate (GelMA) Bioinks with a Two-Step Cross-linking Strategy. *ACS Appl. Bio Mater.* **10**, 6849–6857 (2018).

80. Zhao, X. *et al.* Photocrosslinkable Gelatin Hydrogel for Epidermal Tissue Engineering. *Adv. Healthc. Mater.* **5**, 108–118 (2016).

81. Kolesky, D. B., Homan, K. A., Skylar-Scott, M. A. & Lewis, J. A. Three-dimensional bioprinting of thick vascularized tissues. *Proc. Natl. Acad. Sci. U. S. A.* **113**, 3179–84 (2016).

82. Gomez-Guillen, M. C., Gimenez, B., Lopez-Caballero, M. E. & Montero, M. P. Functional and bioactive properties of collagen and gelatin from alternative sources: A review. *Food Hydrocoll.* **25**, 1813–1827 (2011).

83. Zhao, Y. *et al.* Three-dimensional printing of Hela cells for cervical tumor model in vitro. *Biofabrication* **6**, 035001 (2014).

84. Byambaa, B. *et al.* Bioprinted Osteogenic and Vasculogenic Patterns for Engineering 3D Bone Tissue. *Adv. Healthc. Mater.* **6**, 1700015 (2017).

85. Shao, L. *et al.* Fiber-Based Mini Tissue with Morphology-Controllable GelMA Microfibers. *Small* **14**, 1802187 (2018).

86. Colosi, C. *et al.* Microfluidic Bioprinting of Heterogeneous 3D Tissue Constructs Using Low-Viscosity Bioink. *Adv. Mater.* **28**, 677–684 (2016).

87. Ostrovidov, S. *et al.* 3D Bioprinting in Skeletal Muscle Tissue Engineering. *Small* **15**, 1805530 (2019).

88. Bertassoni, L. E. *et al.* Direct-write Bioprinting of Cell-laden Methacrylated Gelatin Hydrogels. *Biofabrication* **6**, 24105 (2014).

89. Wang, Y. *et al.* Coaxial Extrusion of Tubular Tissue Constructs Using a Gelatin/GelMA Blend Bioink. *ACS Biomater. Sci. Eng.* **5**, 5514–5524 (2019).

90. Antich, C. *et al.* Bio-inspired hydrogel composed of hyaluronic acid and alginate as a potential bioink for 3D bioprinting of articular cartilage engineering constructs. *Acta Biomater.* **106**, 114–123 (2020).

91. Rodell, C. B. *et al.* Shear-thinning supramolecular hydrogels with secondary autonomous covalent crosslinking to modulate viscoelastic properties in vivo. *Adv. Funct. Mater.* **25**, 636–644 (2015).

92. Chen, G., Ushida, T. & Tateishi, T. Scaffold design for tissue engineering. *Macromol. Biosci.* **2**, 67–77 (2002).

93. Malda, J. *et al.* Engineering hydrogels for biofabrication. *Adv. Mater.* **25**, 5011–5028 (2013).

94. Pi, Q. *et al.* Digitally Tunable Microfluidic Bioprinting of Multilayered Cannular Tissues. *Adv. Mater.* **30**, 1706913 (2018).

95. Hansen, C. J. *et al.* Self-healing materials with interpenetrating microvascular networks. *Adv. Mater.* **21**, 4143–4147 (2009).

96. Wu, W., Deconinck, A. & Lewis, J. A. Omnidirectional printing of 3D microvascular networks. *Adv. Mater.* **23**, 178–183 (2011).

97. Kolesky, D. B. *et al.* 3D bioprinting of vascularized, heterogeneous cell-laden tissue constructs. *Adv. Mater.* **26**, 3124–3130 (2014).

98. Lim, K. S. *et al.* Bio-resin for high resolution lithography-based biofabrication of complex cell-laden constructs. *Biofabrication* **10**, 034101 (2018).

99. Crispim, E. G. *et al.* Hydrogels based on chemically modified poly(vinyl alcohol) (PVA-GMA) and PVA-GMA/chondroitin sulfate: Preparation and characterization. *eXPRESS Polym. Lett.* **6**, 383–395 (2012).

100. Zhou, D. *et al.* Photocrosslinked methacrylated poly(vinyl alcohol)/hydroxyapatite nanocomposite hydrogels with enhanced mechanical strength and cell adhesion. *J. Polym.*

Sci. Part A Polym. Chem. **57**, 1882–1889 (2019).

101. Meree, C. E., Schueneman, G. T., Meredith, J. C. & Shofner, M. L. Rheological behavior of highly loaded cellulose nanocrystal/poly(vinyl alcohol) composite suspensions. *Cellulose* **23**, 3001–3012 (2016).

102. Morgacheva, A. A. *et al.* Synthesis of polyvinyl alcohol with metharylate groups and hydrogels based on it. *Macromol. Compd. Polym. Mater.* **88**, 617–621 (2015).

103. Abitbol, T., Johnstone, T., Quinn, T. M. & Gray, D. G. Reinforcement with cellulose nanocrystals of poly(vinyl alcohol) hydrogels prepared by cyclic freezing and thawing. *Soft Matter* **7**, 2373–2379 (2011).

104. Reis, A. V *et al.* Reaction of Glycidyl Methacrylate at the Hydroxyl and Carboxylic Groups of Poly(vinyl alcohol) and Poly(acrylic acid): Is This Reaction Mechanism Still Unclear? *J. Org. Chem.* **74**, 3750–3775 (2009).

105. Chen, S. *et al.* Photocrosslinked Poly(vinyl alcohol) Nanofibrous Scaffolds. *J. Photopolym. Sci. Technol.* **29**, 841–847 (2016).

106. Cavalieri, F., Miano, F., D'Antona, P. & Paradossi, G. Study of Gelling Behavior of Poly(vinyl alcohol)-Methacrylate for Potential Utilizations in Tissue Replacement and Drug Delivery. *Biomacromolecules* **5**, 2439–2446 (2004).

107. Zhang, C. *et al.* High-Performance Photopolymerized Poly(vinyl alcohol)/Silica Nanocomposite Hydrogels with Enhanced Cell Adhesion. *ACS Appl. Mater. Interfaces* **10**, 27692–27700 (2018).

108. Wang, K., Ho, C. C., Zhang, C. & Wang, B. A Review on the 3D Printing of Functional Structures for Medical Phantoms and Regenerated Tissue and Organ Applications. *Engineering* **3**, 653–662 (2017).

109. Shin, S. R. *et al.* Cell-laden microengineered and mechanically tunable hybrid hydrogels of gelatin and graphene oxide. *Adv. Mater.* **25**, 6385–6391 (2013).

110. Cha, C. *et al.* Controlling mechanical properties of cell-laden hydrogels by covalent incorporation of graphene oxide. *Small* **10**, 514–523 (2014).

111. Lee, J. *et al.* Nanoparticle-Based Hybrid Scaffolds for Deciphering the Role of Multimodal Cues in Cardiac Tissue Engineering. *ACS Nano* **13**, 12525–12539 (2019).

112. Dozois, M. D., Bahlmann, L. C., Zilberman, Y. & Tang, X. (Shirley). Carbon nanomaterial-enhanced scaffolds for the creation of cardiac tissue constructs: A new frontier in cardiac tissue engineering. *Carbon* **120**, 338–349 (2017).

113. Patel, K. D., Singh, R. K. & Kim, H. W. Carbon-based nanomaterials as an emerging platform

for theranostics. *Materials Horizons* **6**, 434–469 (2019).

114. Basiri, H. *et al.* Carbon Dots Conjugated with Vascular Endothelial Growth Factor for Protein Tracking in Angiogenic Therapy. *Langmuir* **36**, 2893–2900 (2020).

115. Tadyszak, K., Wychowaniec, J. K. & Litowczenko, J. Biomedical Applications of Graphene-Based Structures. *Nanomaterials* **8**, (2018).

116. Alshehri, R. *et al.* Carbon Nanotubes in Biomedical Applications: Factors, Mechanisms, and Remedies of Toxicity. *J. Med. Chem.* **59**, 8149–8167 (2016).

117. Yi, J., Choe, G., Park, J. & Lee, J. Y. Graphene oxide-incorporated hydrogels for biomedical applications. *Polym. J.* **52**, 823–837 (2020).

118. Shin, S. R. *et al.* Carbon-nanotube-embedded hydrogel sheets for engineering cardiac constructs and bioactuators. *ACS Nano* **7**, 2369–2380 (2013).

119. Domingues, R. M. A., Gomes, M. E. & Reis, R. L. The potential of cellulose nanocrystals in tissue engineering strategies. *Biomacromolecules* **15**, 2327–2346 (2014).

120. Lu, P. & Hsieh, Y. Preparation and properties of cellulose nanocrystals: rods, spheres, and network. *Carbohydr. Polym.* **82**, 329–336 (2010).

121. Habibi, Y., Lucia, L. A. & Rojas, O. J. Cellulose nanocrystals: chemistry, self-Assembly, and applications. *Chem. Rev.* **110**, 3479–3500 (2010).

122. Huq, T. *et al.* Nanocrystalline cellulose (NCC) reinforced alginate based biodegradable nanocomposite film. *Carbohydr. Polym.* **90**, 1757–1763 (2012).

123. Lam, E., Male, K. B., Chong, J. H., Leung, A. C. W. & Luong, J. H. T. Applications of functionalized and nanoparticle-modified nanocrystalline cellulose. *Trends Biotechnol.* **30**, 283–290 (2012).

124. Ahmed, M., Azizi, S., Alloin, F. & Dufresne, A. Review of recent research into cellulosic whiskers, their properties and their application in nanocomposite field. *Biomacromolecules* **6**, 612–626 (2005).

125. Hubbe, M. A., Rojas, O. J., Lucia, L. A. & Sain, M. Cellulosic nanocomposites: a review. *Bioresources* **3**, 929–980 (2008).

126. Lin, N., Huang, J. & Dufresne, A. Preparation, properties and applications of polysaccharide nanocrystals in advanced functional nanomaterials: a review. *Nanoscale* **4**, 3274–3294 (2012).

127. Lin, N. & Dufresne, A. Nanocellulose in biomedicine : current status and future prospect. *Eur. Polym. J.* **59**, 302–325 (2014).

128. Yang, X. & Cranston, E. D. Chemically cross-linked cellulose nanocrystal aerogels with shape recovery and superabsorbent properties. *Chem. Mater.* **26**, 6016–6025 (2014).

129. Moon, R. J. *et al.* Cellulose nanomaterials review: structure, properties and nanocomposites. *Chem. Soc. Rev.* **40**, 3941–3994 (2011).

130. Ureña-Benavides, E. E., Ao, G., Davis, V. A. & Kitchens, C. L. Rheology and phase behavior of lyotropic cellulose nanocrystal suspensions. *Macromolecules* **44**, 8990–8998 (2011).

131. Siqueira, G. *et al.* Cellulose Nanocrystal Inks for 3D Printing of Textured Cellular Architectures. *Adv. Funct. Mater.* **27**, 1604619 (2017).

132. Xu, W. *et al.* On Low-Concentration Inks Formulated by Nanocellulose Assisted with Gelatin Methacrylate (GelMA) for 3D Printing toward Wound Healing Application. *ACS Appl. Mater.* **11**, 8838–8848 (2019).

133. Gomes, M. E., Rodrigues, M. T., Domingues, R. M. A. & Reis, R. L. Tissue engineering and regenerative medicine: new trends and directions - A year in review. *Tissue Engineering - Part B: Reviews* **23**, 211–224 (2017).

134. Tomasina, C., Bodet, T., Mota, C., Moroni, L. & Camarero-Espinosa, S. Bioprinting vasculature: Materials, cells and emergent techniques. *Materials (Basel).* **12**, 2701 (2019).

135. Gaharwar, A. K., Singh, I. & Khademhosseini, A. Engineered biomaterials for in situ tissue regeneration. *Nat. Rev. Mater.* **5**, 686–705 (2020).

136. Banaeiyan, A. A. *et al.* Design and fabrication of a scalable liver-lobule-on-a-chip microphysiological platform. *Biofabrication* **9**, 015014 (2017).

137. Bhise, N. S. *et al.* A liver-on-a-chip platform with bioprinted hepatic spheroids. *Biofabrication* **8**, 014101 (2016).

138. Khetani, S. R. & Bhatia, S. N. Microscale culture of human liver cells for drug development. *Nat. Biotechnol.* **26**, 120–126 (2008).

139. Liu, Y., Li, H., Yan, S., Wei, J. & Li, X. Hepatocyte cocultures with endothelial cells and fibroblasts on micropatterned fibrous mats to promote liver-specific functions and capillary formation capabilities. *Biomacromolecules* **15**, 1044–1054 (2014).

140. Debbaut, C. *et al.* Computer Methods in Biomechanics and Biomedical Engineering A 3D porous media liver lobule model: the importance of vascular septa and anisotropic permeability for homogeneous perfusion A 3D porous media liver lobule model: the importance of vascular sept. *Comput. Methods Biomech. Biomed. Engin.* **17**, 1295–1310 (2013).

141. Ozougwu, J. C. *Physiology of the liver*. *International Journal of Research in Pharmacy and*

Biosciences **4**, (2017).

142. Poisson, J. *et al.* Liver sinusoidal endothelial cells: Physiology and role in liver diseases. *Journal of Hepatology* **66**, 212–227 (2017).

143. Nishikawa, T. *et al.* Optimization of Albumin Secretion and Metabolic Activity of Cytochrome P450 1A1 of Human Hepatoblastoma HepG2 Cells in Multicellular Spheroids by Controlling Spheroid Size. *Biol. Pharm. Bull* **40**, 334–338 (2017).

144. Damm, G. *et al.* Human parenchymal and non-parenchymal liver cell isolation, culture and characterization. *Hepatol. Int.* **7**, 951–958 (2013).

145. Glickman, N. S. & Yelon, D. Cardiac development in zebrafish: coordination of form and function. *Semin. Cell Dev. Biol.* **13**, 507–513 (2002).

146. Kalra, A. & Tuma, F. *Physiology, Liver*. *StatPearls* (StatPearls Publishing, 2018).

147. Kietzmann, T. Metabolic zonation of the liver: The oxygen gradient revisited. *Redox Biology* **11**, 622–630 (2017).

148. Palakkan, A. A., Hay, D. C., Pr, A. K., Tv, K. & Ross, J. A. Liver tissue engineering and cell sources : issues and challenges. *Liver Int.* **33**, 666–676 (2013).

149. Ma, X. *et al.* Deterministically patterned biomimetic human iPSC-derived hepatic model via rapid 3D bioprinting. *PNAS* **113**, 3–8 (2015).

150. Pless, G. Artificial and bioartificial liver support. *Organogenesis* **3**, 20–24 (2007).

151. Zeilinger, K., Freyer, N., Damm, G., Seehofer, D. & Knöspel, F. Cell sources for in vitro human liver cell culture models. *Exp. Biol. Med.* **241**, 1684–98 (2016).

152. Ma, X. *et al.* Rapid 3D bioprinting of decellularized extracellular matrix with regionally varied mechanical properties and biomimetic microarchitecture. *Biomaterials* **185**, 310–321 (2018).

153. Nguyen, D. G. *et al.* Bioprinted 3D primary liver tissues allow assessment of organ-level response to clinical drug induced toxicity in vitro. *PLoS One* **11**, 1–17 (2016).

154. Colosi, C. *et al.* Rapid prototyping of chitosan-coated alginate scaffolds through the use of a 3D fiber deposition technique. *J. Mater. Chem. B* **2**, 6779–6791 (2014).

155. Boesen, M. E., Singh, D., Menon, B. K. & Frayne, R. A systematic literature review of the effect of carotid atherosclerosis on local vessel stiffness and elasticity. *Atherosclerosis* **243**, 211–222 (2015).

156. Shirwany, N. A. & Zou, M. H. Arterial stiffness: A brief review. *Acta Pharmacologica Sinica* **31**, 1267–1276 (2010).

157. Darabian, S., Hormuz, M., Latif, M. A., Pahlevan, S. & Budoff, M. J. The role of carotid intimal thickness testing and risk prediction in the development of coronary atherosclerosis. *Curr. Atheroscler. Rep.* **15**, 1–4 (2013).

158. Chee, A. J. Y., Ho, C. K., Yiu, B. Y. S. & Yu, A. C. H. Walled Carotid Bifurcation Phantoms for Imaging Investigations of Vessel Wall Motion and Blood Flow Dynamics. *IEEE Trans. Ultrason. Ferroelectr. Freq. Control* **63**, 1852–1864 (2016).

159. Iino, H. *et al.* Usefulness of carotid arterial strain values for evaluating the arteriosclerosis. *J. Atheroscler. Thromb.* **26**, 476–487 (2019).

160. Ebrahimi, A. P. Mechanical properties of normal and diseased cerebrovascular system. *J. Vasc. Interv. Neurol.* **2**, 155–162 (2009).

161. Cui, H. *et al.* In vitro and in vivo evaluation of 3D bioprinted small-diameter vasculature with smooth muscle and endothelium. *Biofabrication* **12**, 015004 (2019).

162. Gao, G., Park, J. Y., Kim, B. S., Jang, J. & Cho, D. Coaxial Cell Printing of Freestanding, Perfusable, and Functional In Vitro Vascular Models for Recapitulation of Native Vascular Endothelium Pathophysiology. *Adv. Healthc. Mater.* **7**, 1801102 (2018).

163. Tijore, A., Behr, J.-M., Irvine, S. A., Baisane, V. & Venkatraman, S. Bioprinted gelatin hydrogel platform promotes smooth muscle cell contractile phenotype maintenance. *Biomed. Microdevices* **20**, 32 (2018).

164. Nguyen, K. T., Clark, C. D., Chancellor, T. J. & Papavassiliou, D. V. Carotid geometry effects on blood flow and on risk for vascular disease. *J. Biomech.* **41**, 11–19 (2008).

165. Ohira, T. *et al.* Carotid artery wall thickness and risk of stroke subtypes: the atherosclerosis risk in communities study. *Stroke* **42**, 397–403 (2011).

166. Paul, J., Shaw, K., Dasgupta, S. & Ghosh, M. K. Measurement of intima media thickness of carotid artery by B-mode ultrasound in healthy people of India and Bangladesh, and relation of age and sex with carotid artery intima media thickness: An observational study. *J. Cardiovasc. Dis. Res.* **3**, 128–131 (2012).

167. Maresca, D. *et al.* Biomolecular Ultrasound and Sonogenetics. *Annu. Rev. Chem. Biomol. Eng.* **9**, 229–252 (2018).

168. Yu, A. C. H. & Hossack, J. A. Methods and protocols: Engine for the next wave of biomedical ultrasound innovations. *IEEE Trans. Ultrason. Ferroelectr. Freq. Control* **64**, 6–10 (2017).

169. Chee, A. J. Y., Yiu, B. Y. S., Ho, C. K. & Yu, A. C. H. Arterial Phantoms with Regional Variations in Wall Stiffness and Thickness. *Ultrasound Med. Biol.* **44**, 872–883 (2018).

170. Culjat, M. O., Goldenberg, D., Tewari, P. & Singh, R. S. A review of tissue substitutes for

ultrasound imaging. *Ultrasound Med. Biol.* **36**, 861–873 (2010).

171. Hoskins, P. R. Simulation and Validation of Arterial Ultrasound Imaging and Blood Flow. *Ultrasound Med. Biol.* **34**, 693–717 (2008).

172. Gao, Q. *et al.* 3D Bioprinting of Vessel-like Structures with Multilevel Fluidic Channels. *ACS Biomater. Sci. Eng.* **3**, 399–408 (2017).

173. Gao, Q., He, Y., Fu, J.-Z., Liu, A. & Ma, L. Coaxial nozzle-assisted 3D bioprinting with built-in microchannels for nutrients delivery. *Biomaterials* **61**, 203–215 (2015).

174. Wu, J. *et al.* Tissue-engineered Vascular Grafts: Balance of the Four Major Requirements. *Colloid interface Sci. Commun.* **23**, 34–44 (2018).

175. Piterina, A. *et al.* ECM-Based Materials in Cardiovascular Applications: Inherent Healing Potential and Augmentation of Native Regenerative Processes. *Int. J. Mol. Sci.* **10**, 4375–4417 (2009).

176. Domingo-Roca, R., Saltin, B., Windmill, J., Jackson, J. & Mulvana, H. Rapid prototyped microvessel flow phantom for controlled investigation of ultrasound-mediated targeted drug delivery. in *2019 IEEE International Ultrasonics Symposium (IUS)* 2390–2393 (IEEE Computer Society, 2019). doi:10.1109/ULTSYM.2019.8925741

177. Filippou, V. & Tsoumpas, C. Recent advances on the development of phantoms using 3D printing for imaging with CT, MRI, PET, SPECT, and ultrasound. *Med. Phys.* **45**, e740–e760 (2018).

178. Ommen, M. L. *et al.* 3D Printed Flow Phantoms with Fiducial Markers for Super-Resolution Ultrasound Imaging. in *2018 IEEE International Ultrasonics Symposium (IUS)* 1–9 (IEEE Computer Society, 2018). doi:10.1109/ULTSYM.2018.8580217

179. Demitri, C., Mercurio, L., Montagna, F., Sannino, A. & Maffezzoli, A. Acrylic-based hydrogel phantom for *in vitro* ultrasound contrast agent characterization. *Virtual Phys. Prototyp.* **2**, 191–196 (2007).

180. Aliabouzar, M., Zhang, G. L. & Sarkar, K. Acoustic and mechanical characterization of 3D-printed scaffolds for tissue engineering applications. *Biomed. Mater.* **13**, 055013 (2018).

181. Maxwell, A. D. *et al.* A tissue phantom for visualization and measurement of ultrasound-induced cavitation damage. *Ultrasound Med. Biol.* **36**, 2132–2143 (2010).

182. Li, X., Zhang, J., Kawazoe, N. & Chen, G. Fabrication of Highly Crosslinked Gelatin Hydrogel and Its Influence on Chondrocyte Proliferation and Phenotype. *Polymers (Basel).* **9**, 309 (2017).

183. Spoljaric, S., Salminen, A., Dang Luong, N. & Seppälä, J. Stable, self-healing hydrogels from

nanofibrillated cellulose, poly(vinyl alcohol) and borax via reversible crosslinking. *Eur. Polym. J.* **56**, 105–117 (2014).

184. Shirahama, H., Lee, B. H., Tan, L. P. & Cho, N.-J. Precise Tuning of Facile One-Pot Gelatin Methacryloyl (GelMA) Synthesis. *Sci. Rep.* **6**, 31036 (2016).

185. Su, W.-F. Radical Chain Polymerization. in *Principles of Polymer Design and Synthesis* 137–183 (Springer, 2013). doi:10.1007/978-3-642-38730-2_7

186. Fairbanks, B. D., Schwartz, M. P., Bowman, C. N. & Anseth, K. S. Photoinitiated polymerization of PEG-diacrylate with lithium phenyl-2,4,6-trimethylbenzoylphosphinate: polymerization rate and cytocompatibility. *Biomaterials* **30**, 6702–6707 (2009).

187. Lambert, J. B., Mazzola, E. P. & Ridge, C. D. *Nuclear Magnetic Resonance Spectroscopy: an Introduction to Principles, Applications, and Experimental Methods.* (John Wiley & Sons, 2019).

188. Ebagninin, K. W., Benchabane, A. & Bekkour, K. Rheological characterization of poly(ethylene oxide) solutions of different molecular weights. *J. Colloid Interface Sci.* **336**, 360–367 (2009).

189. Jaishankar, A., Wee, M., Matia-Merino, L., Goh, K. K. T. & McKinley, G. H. Probing hydrogen bond interactions in a shear thickening polysaccharide using nonlinear shear and extensional rheology. *Carbohydr. Polym.* **123**, 136–145 (2015).

190. Ding, J. *et al.* Review on shear thickening fluids and applications Publication Details. *Text. Light Ind. Sci. Technol.* **2**, 161–173 (2013).

191. Wagner, C. E., Barbati, A. C., Engmann, J., Burbidge, A. S. & Mckinley, G. H. Apparent shear thickening at low shear rates in polymer solutions can be an artifact of non-equilibration. *Appl. Rheol.* **26**, 36–40 (2016).

192. Patrício, S. G. *et al.* Freeform 3D printing using a continuous viscoelastic supporting matrix. *Biofabrication* **12**, 035017 (2020).

193. Feng, L. *et al.* Three-Dimensional Printing of Hydrogel Scaffolds with Hierarchical Structure for Scalable Stem Cell Culture. *ACS Biomater. Sci. Eng* **6**, 2995–3004 (2020).

194. Singh, N. K. *et al.* Three-dimensional cell-printing of advanced renal tubular tissue analogue. *Biomaterials* **232**, 119734 (2020).

195. Luo, Q., Kuang, D., Zhang, B. & Song, G. Cell stiffness determined by atomic force microscopy and its correlation with cell motility. *Biochimica et Biophysica Acta - General Subjects* **1860**, 1953–1960 (2016).

196. Zhu, M. *et al.* Gelatin methacryloyl and its hydrogels with an exceptional degree of controllability and batch-to-batch consistency. *Sci. Rep.* **9**, 1–13 (2019).

197. Solon, J., Levental, I., Sengupta, K., Georges, P. C. & Janmey, P. A. Fibroblast adaptation and stiffness matching to soft elastic substrates. *Biophys. J.* **93**, 4453–4461 (2007).

198. Duan, B., Yin, Z., Hockaday, L. A., Magin, R. L. & Butcher, J. T. Active Tissue Stiffness Modulation Controls Valve Interstitial Cell Phenotype and Osteogenic Potential in 3D Culture. *Acta Biomater.* **36**, 42–54 (2016).

199. Duin, S. *et al.* 3D Bioprinting of Functional Islets of Langerhans in an Alginate/Methylcellulose Hydrogel Blend. *Adv. Healthc. Mater.* **8**, 1801631 (2019).

200. Song, Y. *et al.* Engineering of brain-like tissue constructs via 3D Cell-printing technology. *Biofabrication* **12**, 035016 (2020).

201. Rao, S. S. *et al.* Inherent Interfacial Mechanical Gradients in 3D Hydrogels Influence Tumor Cell Behaviors. *PLoS One* **7**, e35852 (2012).

202. Lo, C.-M., Wang, H.-B., Dembo, M. & Wang, Y.-L. Cell Movement Is Guided by the Rigidity of the Substrate. *Biophys. J.* **79**, 144–152 (2000).

203. DuChez, B. J., Doyle, A. D., Dimitriadis, E. K. & Yamada, K. M. Durotaxis by Human Cancer Cells. *Biophys. J.* **116**, 670–683 (2019).

204. Jung, H.-R. *et al.* Cell Spheroids with Enhanced Aggressiveness to Mimic Human Liver Cancer In Vitro and In Vivo. *Sci. Rep.* **7**, 10499 (2017).

205. Lee, H. W., Kook, Y.-M., Lee, H. J., Park, H. & Koh, W.-G. A three-dimensional co-culture of HepG2 spheroids and fibroblasts using double-layered fibrous scaffolds incorporated with hydrogel micropatterns. *RSC Adv.* **4**, 61005–61011 (2014).

206. Jeong, D. *et al.* Effect of Concentrated Fibroblast-Conditioned Media on In Vitro Maintenance of Rat Primary Hepatocyte. *PLoS One* **11**, 0148846 (2016).

207. Silvério, H. A., Flauzino Neto, W. P. & Pasquini, D. Effect of incorporating cellulose nanocrystals from corncob on the tensile, thermal and barrier properties of poly(vinyl alcohol) nanocomposites. *J. Nanomater.* **2013**, (2013).

208. Bai, H., Li, Z., Zhang, S., Wang, W. & Dong, W. Interpenetrating polymer networks in polyvinyl alcohol/cellulose nanocrystals hydrogels to develop absorbent materials. *Carbohydr. Polym.* **200**, 468–476 (2018).

209. Ino, J. M. *et al.* Evaluation of hemocompatibility and endothelialization of hybrid poly(vinyl alcohol) (PVA)/gelatin polymer films. *J. Biomed. Mater. Res. Part B Appl. Biomater.* **101**, 1549–1559 (2013).

210. Vrana, N. E., Cahill, P. A. & McGuinness, G. B. Endothelialization of PVA/gelatin cryogels for vascular tissue engineering: Effect of disturbed shear stress conditions. *J. Biomed. Mater.*

Res. Part A **94**, 1080–1090 (2010).

211. Crispim, E. G., Piai, J. F., Rubira, A. F. & Muniz, E. C. Addition of methacryloil groups to poly(vinyl alcohol) in DMSO catalyzed by TEMED: Optimization through response surface methodology. *Polym. Test.* **25**, 377–383 (2006).

212. Li, J. *et al.* Tough adhesives for diverse wet surfaces. *Science* **357**, 378–381 (2017).

213. Lu, B. *et al.* One-Pot Assembly of Microfibrillated Cellulose Reinforced PVA− Borax Hydrogels with Self-Healing and pH-Responsive Properties. *ACS Sustain. Chem. Eng.* **5**, 948–956 (2017).

214. Han, J., Lei, T. & Wu, Q. High-water-content mouldable polyvinyl alcohol-borax hydrogels reinforced by well-dispersed cellulose nanoparticles: Dynamic rheological properties and hydrogel formation mechanism. *Carbohydr. Polym.* **102**, 306–316 (2014).

215. Yang, J., Han, C. R., Zhang, X. M., Xu, F. & Sun, R. C. Cellulose nanocrystals mechanical reinforcement in composite hydrogels with multiple cross-links: Correlations between dissipation properties and deformation mechanisms. *Macromolecules* **47**, 4077–4086 (2014).

216. Huang, S., Zhao, Z., Feng, C., Mayes, E. & Yang, J. Nanocellulose reinforced P(AAm-co-AAc) hydrogels with improved mechanical properties and biocompatibility. *Compos. Part A Appl. Sci. Manuf.* **112**, 395–404 (2018).

217. Kaazempur-Mofrad, M. R. *et al.* Cyclic strain in human carotid bifurcation and its potential correlation to atherogenesis: Idealized and anatomically-realistic models. *J. Eng. Math.* **47**, 299–314 (2003).

218. Wyss, C. S., Karami, P., Bourban, P. E. & Pioletti, D. P. Cyclic loading of a cellulose/hydrogel composite increases its fracture strength. *Extrem. Mech. Lett.* **24**, 66–74 (2018).

219. Chen, K. *et al.* Preparation and property of high strength and low friction PVA-HA/PAA composite hydrogel using annealing treatment. *Mater. Sci. Eng. C* **91**, 579–588 (2018).

220. Yang, J., Han, C.-R., Xu, F. & Sun, R.-C. Simple approach to reinforce hydrogels with cellulose nanocrystals. *Nanoscale* **6**, 5934 (2014).

221. Khoushabi, A., Wyss, C. S., Caglar, B., Pioletti, D. & Bourban, P. E. Tailoring swelling to control softening mechanisms during cyclic loading of PEG/cellulose hydrogel composites. *Compos. Sci. Technol.* **168**, 88–95 (2018).

222. Yang, J., Bai, R., Chen, B. & Suo, Z. Hydrogel Adhesion: A Supramolecular Synergy of Chemistry, Topology, and Mechanics. *Adv. Funct. Mater.* **31**, 1901693 (2019).

223. Yang, J. *et al.* Design Molecular Topology for Wet-Dry Adhesion. *ACS Appl. Mater. Interfaces* **11**, 24802–24811 (2019).

224. Metwally, S. & Stachewicz, U. Surface potential and charges impact on cell responses on biomaterials interfaces for medical applications. *Mater. Sci. Eng. C* **104**, 109883 (2019).

225. Khuu, N. *et al.* Temperature-Mediated Microfluidic Extrusion of Structurally Anisotropic Hydrogels. *Adv. Mater. Technol.* **4**, 1800627 (2019).

226. Akhlaghi, S. P. *et al.* Synthesis of amine functionalized cellulose nanocrystals: optimization and characterization. *Carbohydr. Res.* **409**, 48–55 (2015).

227. Martin, P. *et al.* pH-Controlled network formation in a mixture of oppositely charged cellulose nanocrystals and poly(allylamine). *J. Polym. Sci. Part B Polym. Phys.* **57**, 1527–1536 (2019).

228. Qi, W., Yu, J., Zhang, Z. & Xu, H. N. Effect of pH on the aggregation behavior of cellulose nanocrystals in aqueous medium. *Mater. Res. Express* **6**, 125078 (2019).

229. Webb, K., Hlady, V. & Tresco, P. A. Relative importance of surface wettability and charged functional groups on NIH 3T3 fibroblast attachment, spreading, and cytoskeletal organization. *J. Biomed. Mater. Res.* **41**, 422–430 (1998).

230. Kim, J. *et al.* Charged nanomatrices as efficient platforms for modulating cell adhesion and shape. *Tissue Eng. - Part C Methods* **18**, 913–923 (2012).

Appendix A

3D Printer Design and Dual-syringe System

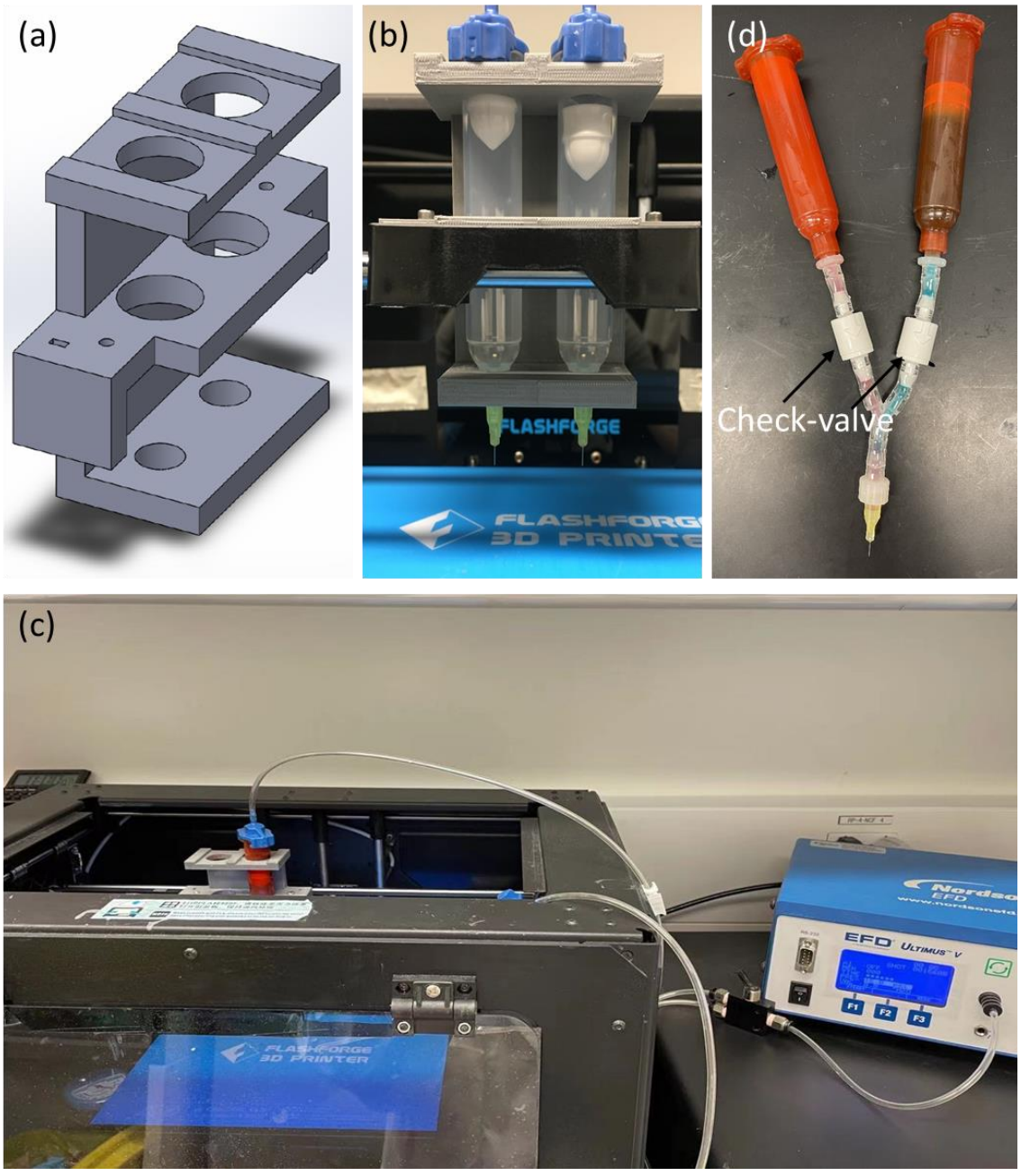

Figure A.1 (a) Schematic of the customized dual-syringe holder. (b) Image of the printed dual-syringe holder. (c) The bioink-laden syringe is connected to a pneumatic system. (d) Images of the dual-syringe printing design with a check-valve connecting to both syringes to avoid backflow of the bioinks.

Appendix B

Embedded printed Hollow Tubes Without in-situ Crosslinking and Rupture Images

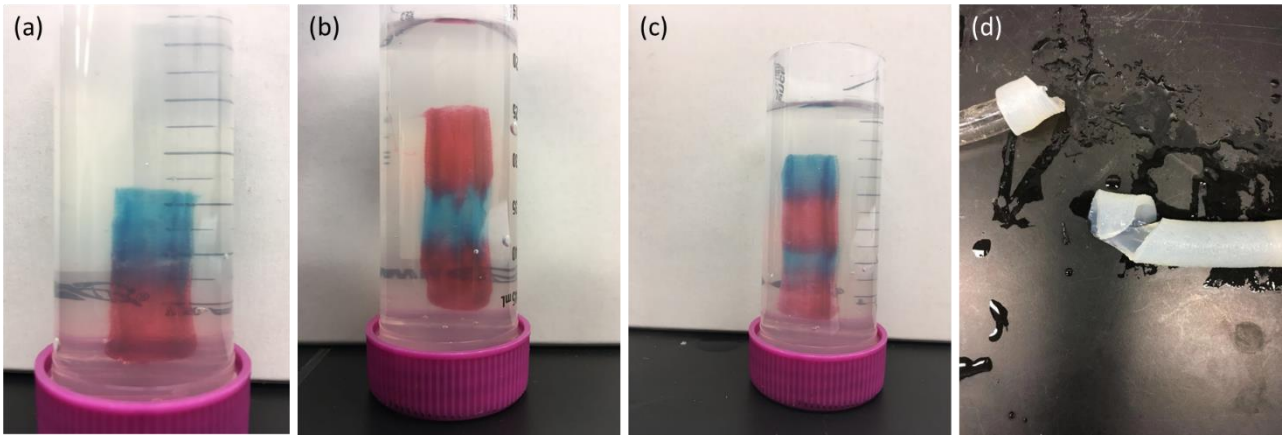

Figure B.1 (a) Two-segment, (b) three-segment, and (c) four-segment hollow tubes were printed without *in-situ* UV crosslinking. Sedimentation and deformation were observed, suggesting that the *in-situ* crosslinking helped maintain shape fidelity. (d) The printed vessel tube broke at high pressure with the rupture region not along the printing direction, illustrating optimal layer integrity.

Appendix C

Surface Modification of CNC and the Characterizations

Less negatively-charged CNCs (DS-CNCs) and positively-charged CNCs (GTMAC-CNCs) were synthesized as per the method provided by Dr. Michael Tam's group as illustrated in **Figure C.1**. Briefly, 2 wt% CNC (10 g) suspension was prepared in water and dispersed for 30 min using a homogenizer followed by sonication for 10 min. NaOH solution (5 M, 350 mL) was added to the CNC suspension. The reaction mixture was stirred at 500 rpm at 65 ℃ for 5 hours. The mixture turned slightly yellowish/greenish and settled during the reaction due to the removal of sulfate groups. After the reaction, the mixture was cooled to room temperature in an ice bath followed by centrifugation at 8000 g for 10 min. The precipitate was collected and re-dispersed in Milli-Q water before dialysis for 7 days. Once the dialysis was done, rotary evaporation was conducted to concentrate the DS-CNC suspension. The final concentration of DS-CNCs determined by gravimetric analysis was found to be approximately 3 wt%.

Solvent exchange with DMSO was performed on DS-CNC suspension to obtain DS-CNCs in DMSO at a concentration of 1 wt%. Same amount of tetrabutylammonium hydroxide (TBAH) was added to the DS-CNC suspension and it was purged with nitrogen to degas the mixture for 30 min at room temperature. Glycidyl trimethyl ammonium chloride (GTMAC) at a 3:1 molar ratio of GTMAC:anhydroglucose unit was added to the reaction mixture. The reaction took place at 65℃ for 5 hours and slightly brownish suspension was obtained, followed by dialysis directly against water for 5 days using a 12 kDa molecular weight cut-off (MWCO) membrane. Similarly, rotary evaporation was conducted to concentrate the GTMAC-CNC suspension and the final concentration of GTMAC-CNCs

was found to be 6 wt%.

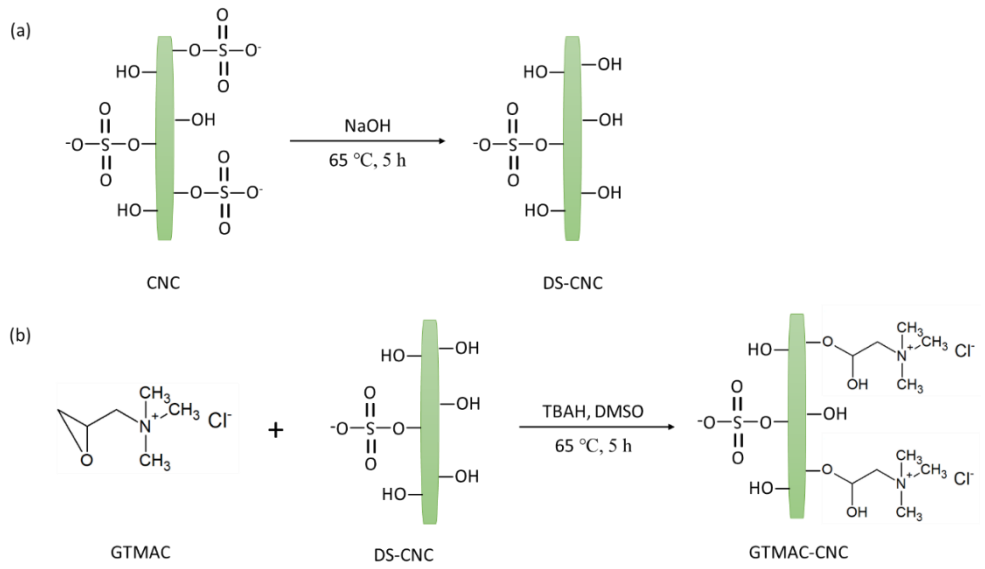

Figure C.1 Chemical modification of CNCs. (a) Less negatively charged CNC (DS-CNC) was synthesized by the surface desulfation of CNC in strong basic conditions for 5 hours. (b) Positively charged CNC (GTMAC-CNC) was synthesized by grafting glycidyl trimethyl ammonium chloride (GTMAC) onto DS-CNC in the presence of tetrabutylammonium hydroxide (TBAH) in DMSO for 5 hours.

Physical characterizations, such as zeta potential, size distribution, and rheological properties, and cytotoxicity tests were performed on the synthesized DS-CNC and GTMAC-CNC suspensions.

DS-CNCs, GTMAC-CNCs, and CNCs were dispersed in water and the pH was adjusted from 4 to 10. Zeta potential of all the suspensions was measured and illustrated in **Figure C.2a**. It is observed that the unmodified CNCs possessed negative zeta potentials at all the pH values due to the presence of the sulfate ester groups on CNCs. With the pH decreasing from 7 to 4, the zeta potential increased from -39.2 mV to -26.8 mV ascribed to screening effects and protonation of the negative charged sulfate ester groups.[226,227] In basic conditions, the zeta potential increased with the increasing pH as the sulfate ester groups were hydrolyzed and Na^+ may also shield electrons.[226,228] The surface

desulfation of CNCs lead to less negative zeta potentials compared to unmodified CNCs because part of the sulfate ester groups were replaced with hydroxyl groups. Moreover, zeta potential measurements confirmed the successful functionalization of CNCs with GTMAC, making GTMAC-CNCs highly positively charged in all pH values.

Dynamic light scattering was performed on DS-CNC, GTMAC-CNC, and CNC suspensions (pH 7.0) immediately after sonication to measure their size distributions. The results show that the radius of the CNC particles ranged from 3 to 110 nm with a distribution peak at 30 nm (**Figure C.2b**). The distribution peak of DS-CNCs and GTMAC-CNCs was at 71 and 82 nm, respectively, indicating that the modified particles are slightly larger than pristine CNCs. However, a small peak at 2780 nm was observed in GTMAC which could be explained by particle aggregation.

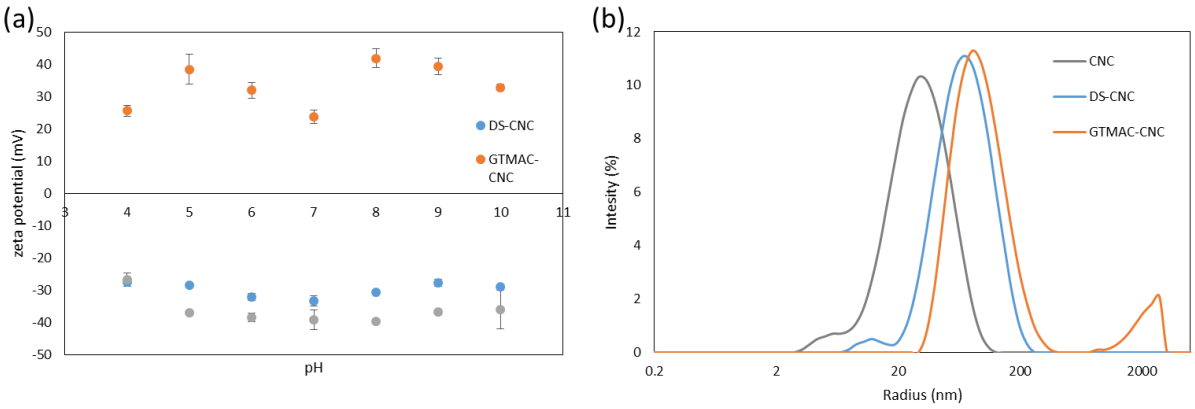

Figure C.2 (a) Zeta potential and (b) size distribution of CNCs, DS-CNCs, and GTMAC-CNCs.

The rheological properties of the unmodified and modified CNC suspensions were measured and illustrated in **Figure C.3**. All samples exhibited shear-thinning regions because of the alignment of CNCs and the chiral nematic domains. Compared to pristine CNC suspensions, the viscosity profile of both modified CNC suspensions exhibited a strong shear-thinning property over the entire shear rate

range, and DS-CNC suspensions possessed the highest viscosity at the same shear rate (**Figure C.3a**). Additionally, 6 wt% GTMAC-CNC suspensions possessed a similar viscosity to that of 3 wt% DS-CNC suspensions. The improved shear-thinning property and viscosity of DS-CNC suspensions can be explained by the enhanced hydrogen bonding. The shear-thinning behavior in GTMAC-CNC suspensions may be caused by the strong electrostatic interaction between the positively-charged ammonium groups and negatively-charged sulfate ester groups. Another hypothesis for this phenomena is the larger size of the CNC derivatives when compared to pure CNCs. Moreover, 6 wt% GTMAC-CNC and 3 wt% DS-CNC suspensions were more solid-like, while 3 wt% CNC and GTMAC-CNC suspensions were more liquid-like, suggesting they are suitable for 3D printing (**Figure C.3b**).

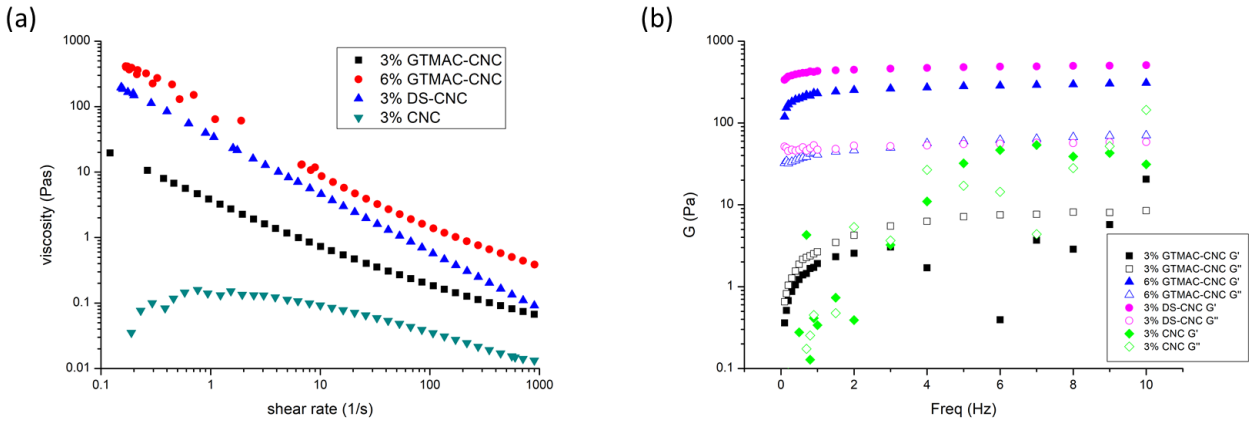

Figure C.3 Rheological properties of the suspension of CNC and its derivatives. (a) Flow curves and (b) elastic modulus (G') and viscous modulus (G'') as a function of frequency of pure GTMAC-CNC, DS-CNC, and CNC suspensions.

Besides the rheological properties of the pure CNC and its derivatives suspensions, rheological measurements of hybrid inks composed of alginate and CNC or its derivatives were performed as well (**Figure C.4**). Due to the limit of initial concentration of DS-CNC, the highest concentration of DS-CNC

was 2 wt% in the hybrid inks while that of CNC and GTMAC-CNC was 3 wt%. A homogeneous suspension was prepared when alginate was mixed with CNC and DS-CNC, however, phase separation occurred with the addition of increasing amount of GTMAC-CNC owing to the electrostatic interactions between negatively charged alginate and positively charged GTMAC-CNC as shown in the inserted images in **Figure C.4a**, therefore, ink comprising 1 wt% alginate and 3 wt% GTMAC-CNC (13Alg-GTMAC) possessed the lowest viscosity and the least shear-thinning behavior. In contrast, 1 wt% alginate and 2 wt% DC-CNC (12Alg-DSCNC) showed the strongest shear-thinning and the highest viscosity which could be explained by the improved hydrogen bonding between alginate and the less negatively-charged DS-CNCs. Additionally, as shown in **Figure C.4b**, the elastic moduli G' were higher than the viscous moduli G" over the entire frequency range in all three different compositions, indicating that all the hybrid inks were more solid-like and could produce scaffolds with good structural fidelity. Moduli of suspensions with different amount of DS-CNCs and GTMAC-CNCs were also measured and illustrated in **Figure C.4c-d**. The elastic moduli G' were larger than the viscous moduli G" in 11Alg-DSCNC and 12Alg-GTMAC inks at low frequencies, and G" overtook G' at around 6 Hz, indicating the two compositions were more solid-like at low frequencies and can be utilized for ME bioprinting. However, when the concentration of GTMAC-CNC lowered to 1 wt%, it was more liquid-like at low frequencies, meaning it was not suitable for freeform printing, thus 11Alg-DSCNC and 12Alg-GTMAC were selected as the compositions for cell studies.

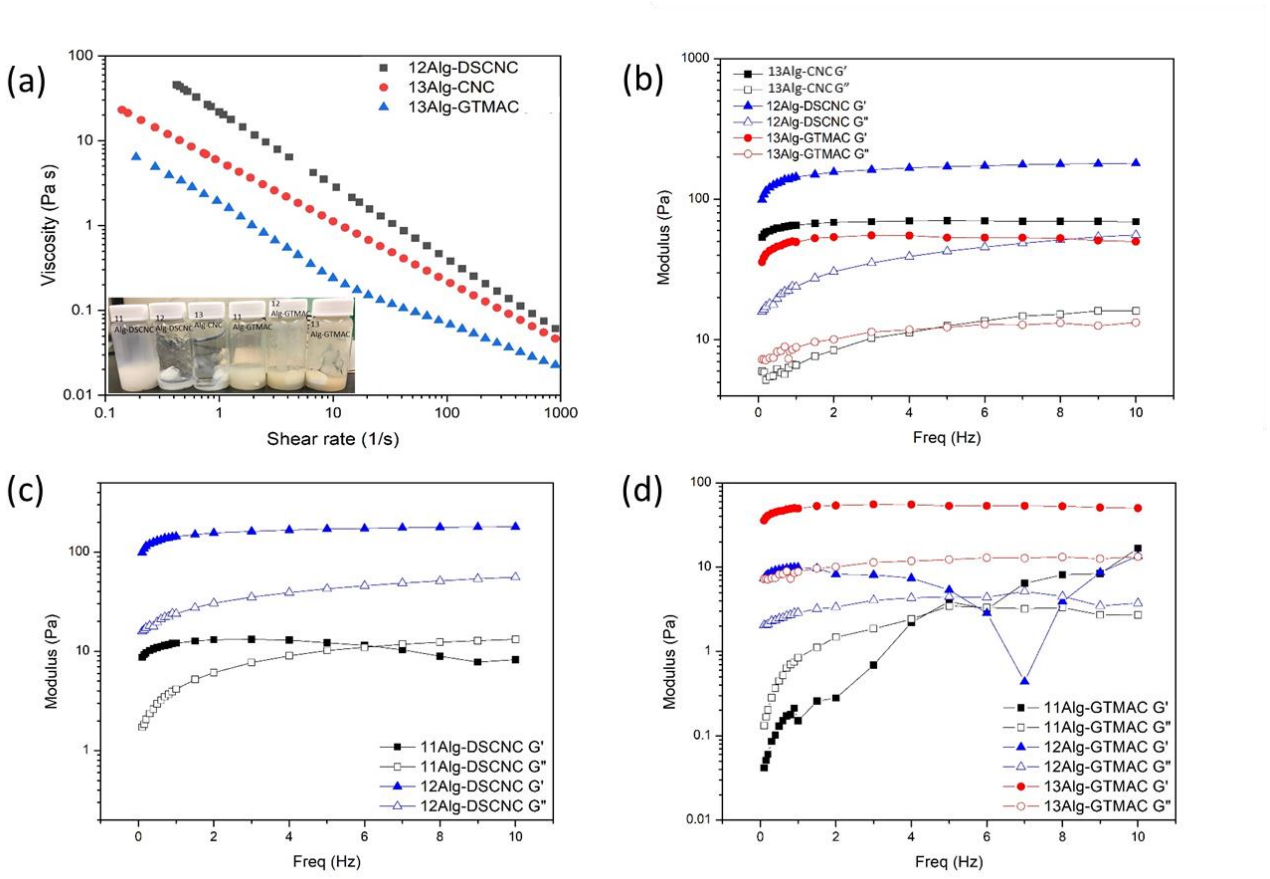

Figure C.4 Rheological properties of hybrid inks composed of alginate and CNC or its derivatives. (a) Flow curves and (b) elastic modulus (G') and viscous modulus (G'') as a function of frequency of pre-gel solutions composed of alginate with CNC derivatives. (c) Elastic modulus (G') and viscous modulus (G'') as a function of frequency of alginate and DS-CNC hybrid solutions with different concentrations of DS-CNC. (d) Elastic modulus (G') and viscous modulus (G'') as a function of frequency of alginate and GTMAC-CNC hybrid solutions with different concentrations of GTMCA-CNC.

To test the cytotoxicity of the inks and the effect of surface charge on cell growth, a live/dead assay kit was utilized to visualize NIH/3T3 fibroblast encapsulated in the printed constructs. GelMA was incorporated to introduce the cell attachment sites. As shown in **Figure C.5**, the cells elongated and proliferated in the negatively charged CNC-, CNF-, and DS-CNC-containing hybrid bioinks, namely

115Alg-CNC-Gel, 115Alg-CNF-Gel, 115Alg-DSCNC-Gel. Compared to 115Alg-CNC-Gel, the cell proliferation rate and cell size were larger in both 115Alg-CNF-Gel and 115Alg-DSCNC-Gel, which is attributed to the fibrillar structure of CNF and less negative charge of the DS-CNC. Interestingly, cells cultured in 125Alg-GTMAC-Gel exhibited round morphology but with a lower cell viability. One possibility of the low cell viability is that the prepared GTMAC-CNC was not pure enough and further dialysis is still needed. The different cell morphology between 125Alg-GTMAC-Gel and the other three bioinks is ascribed to the opposite surface charges. Chondroitin sulfate proteoglycans on cell membranes are negative charged and the electrostatic interactions between chondroitin sulfate proteoglycans and the charged matrix plays a vital role in cell adhesion and growth. The positively charged surfaces electrostatically promote cell adhesion as compared to the negatively charged surfaces, thus cells of bipolar shape with reduced focal adhesion are predominant on the negative surfaces, while cells adopt to rounded, well-spread morphology on the positively charged matrix.[229,230]

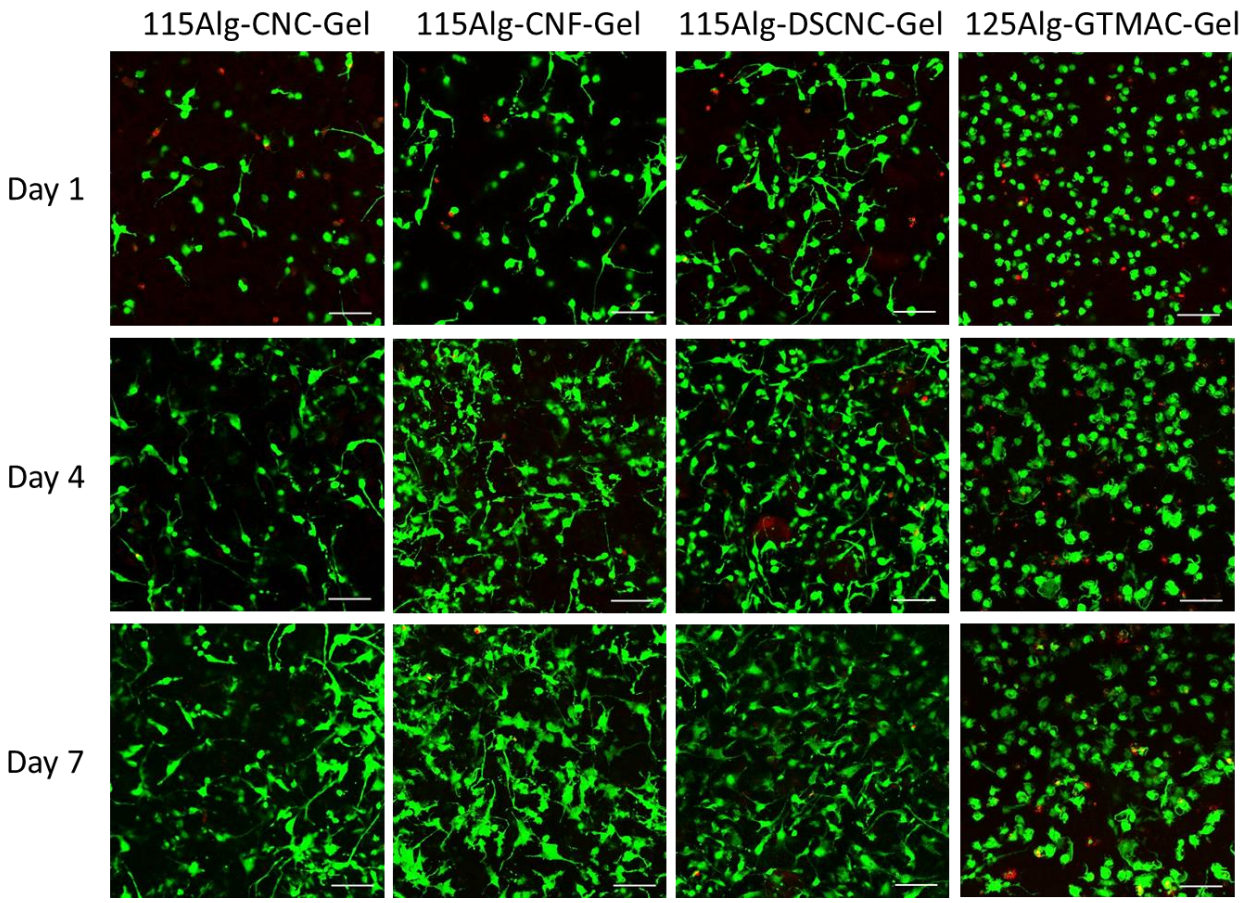

Figure C.5 Representative live/dead fluorescent images of fibroblast encapsulated in 115Alg-CNC-Gel, 115Alg-CNF-Gel, 115Alg-DSCNC-Gel, and 125Alg-GTMAC-Gel at day 1, 4, and 7.